Spring 2009

# Computational study of pristine and titanium-doped sodium alanates for hydrogen storage applications

Gopi Krishna Phani Dathar
*Louisiana Tech University*

Follow this and additional works at: https://digitalcommons.latech.edu/dissertations

 Part of the Materials Science and Engineering Commons, and the Physical Chemistry Commons

# COMPUTATIONAL STUDY OF PRISTINE

# AND Ti-DOPED SODIUM ALANATES

# FOR HYDROGEN STORAGE

# APPLICATIONS

by

Gopi Krishna Phani Dathar, M.S

A Dissertation Presented in Partial Fulfillment of the
Requirements for the Degree of Doctor
of Philosophy in Engineering

COLLEGE OF ENGINEERING AND SCIENCE
LOUISIANA TECH UNIVERSITY

May 2009

UMI Number: 3358248

INFORMATION TO USERS

The quality of this reproduction is dependent upon the quality of the copy submitted. Broken or indistinct print, colored or poor quality illustrations and photographs, print bleed-through, substandard margins, and improper alignment can adversely affect reproduction.
In the unlikely event that the author did not send a complete manuscript and there are missing pages, these will be noted. Also, if unauthorized copyright material had to be removed, a note will indicate the deletion.

# UMI®

# LOUISIANA TECH UNIVERSITY

## THE GRADUATE SCHOOL

04/01/2009
_____
Date

We hereby recommend that the dissertation prepared under our supervision

by ___GOPI KRISHNA PHANI DATHAR_____

entitled_____

### COMPUTATIONAL STUDY OF PRISTINE AND Ti-DOPED

### SODIUM ALANATES FOR HYDROGEN STORAGE

### APPLICATIONS

be accepted in partial fulfillment of the requirements for the Degree of

### DOCTOR OF PHILOSOPHY

_____
Supervisor of Dissertation Research

_____
Head of Department

ENGINEERING
_____
Department

Recommendation concurred in:
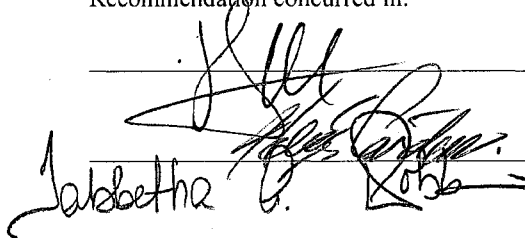
_____
_____  Advisory Committee

_____
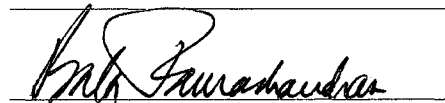
**Approved:**

_____
Director of Graduate Studies

_____
Dean of the College

**Approved:**

_____
Dean of the Graduate School

# ABSTRACT

The emphasis of this research is to study and elucidate the underlying mechanisms of reversible hydrogen storage in pristine and Ti-doped sodium aluminum hydrides using molecular modeling techniques. An early breakthrough in using complex metal hydrides as hydrogen storage materials is from the research on sodium alanates by Bogdanovic et al., in 1997 reporting reversible hydrogen storage is possible at moderate temperatures and pressures in transition metal doped sodium alanates. Anton reported titanium salts as the best catalysts compared to all other transition metal salts from his further research on transition metal doped sodium alanates. However, a few questions remained unanswered regarding the role of Ti in reversible hydrogen storage of sodium alanates with improved thermodynamics and kinetics of hydrogen desorption.

The first question is about the position of transition metal dopants in the sodium aluminum hydride lattice. The position is investigated by identifying the possible sites for titanium dopants in $NaAlH_4$ lattice and studying the structure and dynamics of possible compounds resulting from titanium doping in sodium alanates. The second question is the role of titanium dopants in improved thermodynamics of hydrogen desorption in Ti-doped $NaAlH_4$. Though it is accepted in the literature that formation of TiAl alloys (Ti-Al and $TiAl_3$) is favorable, reaction pathways are not clearly established. Furthermore, the source of aluminum for Ti-Al alloy formation is not clearly understood. The third question in this area is the role of titanium dopants in improved kinetics of

hydrogen absorption and desorption in Ti-doped sodium alanates. This study is directed towards addressing the three longstanding questions in this area. Thermodynamic and kinetic pathways for hydrogen desorption in pristine $NaAlH_4$ and formation of Ti-Al alloys in Ti-doped $NaAlH_4$, are elucidated to understand the underlying mechanisms of hydrogen desorption.

Density functional theory formalism as implemented in CASTEP (Cambridge Serial Total Energy Package) is used to study the structure and energetics of pristine and Ti-doped sodium alanates. From investigations of various models of sodium alanates with Ti dopants, it is shown that the difference between the energy required for Ti$\rightarrow S_{Na}$ (Ti-substituted Na at the lattice site on the surface) and Ti$\rightarrow T_I$ (Ti placed on top of the surface interstitial $S_I$ site) is 0.003 eV atom$^{-1}$, and is minimal compared to other models. Since less energy is required for Ti$\rightarrow S_{Na}$ and Ti$\rightarrow T_I$, these two sites ($S_{Na}$ and $T_I$) would be preferred by the Ti dopants. In Ti$\rightarrow S_{Na}$ model, Ti is coordinated to two aluminum and seven hydrogen atoms resulting in the possible formation of a $TiAl_2H_7$ complex. At elevated temperatures (423 and 448 K), the number of aluminum atoms coordinating with titanium in the complex increase from two (at distances in the 2.6-2.7 Å range) to five (at distances in the 2.6-2.7 Å range). Besides the formation of a Ti-Al-H complex, Al-Al association (with a 2.97 Å bond length) is also seen from the DFT-MD results. In the case of Ti$\rightarrow T_I$, Ti is coordinated to two aluminum and two hydrogen atoms resulting in the possible formation of a $TiAl_2H_2$ complex. $TiAl_2H_2$ complex becomes $TiAl_3H_6$ and $TiAl_3H_7$ at elevated temperatures of 423 and 448 K, respectively.

The investigation of thermodynamics pathways in Ti-doped sodium alanates illustrates a three step reaction pathway to the formation of $TiAl_3$ (Ti and $AlH_3$ after the

first reaction, TiAl after the second and finally TiAl$_3$). This investigation also suggests aluminum in its +3 oxidation state present in aluminum hydride species is responsible in the formation of Ti-Al alloys. From kinetics studies, the proposed mechanism is related to transition from AlH$_4^-$ to AlH$_6^{3-}$. The rate limiting step is determined to be associated with hydrogen evolution from association of AlH$_3$ species nucleating aluminum phase. This step is 15 kJ/mol higher than the nearest highest barrier in the reaction path related to transition from AlH$_5^{2-}$ to AlH$_6^{3-}$. From the DFT-MD simulations, it is observed that the titanium dopants are present on the surface during the entire simulation time and exhibit the role in catalytic splitting of hydrogen from surrounding AlH$_4$ groups. Besides the catalytic role, Ti dopants also form bonds with Al, and we also see that the AlH$_4$ groups on the surface and that are present in the sub-surface layers are drawn towards the Ti dopants. This association of Al around titanium indicates the initiation of Al nucleation site facilitated by Ti dopants residing on the surface.

## APPROVAL FOR SCHOLARLY DISSEMINATION

The author grants to the Prescott Memorial Library of Louisiana Tech University the right to reproduce, by appropriate methods, upon request, any or all portions of this Dissertation. It is understood that "proper request" consists of the agreement, on the part of the requesting party, that said reproduction is for his personal use and that subsequent reproduction will not occur without written approval of the author of this Dissertation. Further, any portions of the Dissertation used in books, papers, and other works must be appropriately referenced to this Dissertation.

Finally, the author of this Dissertation reserves the right to publish freely, in the literature, at any time, any or all portions of this Dissertation.

Author _GOPI KRISHNA PHANI DATIHAR_

Date _04|22|09_

# <u>DEDICATION</u>

To

My dear parents Vijaya Lakshmi and Laxman Rao and my loving wife Poornima without whom, this is not possible.

# TABLE OF CONTENTS

# LIST OF TABLES

# LIST OF FIGURES

# ACKNOWLEDGEMENTS

# CHAPTER 1

## INTRODUCTION AND BACKGROUND

Fast depletion of fossil fuels coupled with increase in environmental pollution and global warming demands replacement of existing non-renewable energy sources with renewable and cleaner fuels. Potential alternative energy sources such as energy from wind, solar, nuclear, and hydrogen have not yet been accepted to replace the fossil fuels, due to the difficulties that include production, storage, distribution, and application to suit the current day needs [1]. Among the alternative sources, hydrogen energy has received much attention lately. Hydrogen is most abundant in the universe, but its existence in elemental form is very rare. Present extraction of hydrogen in industrial settings from compounds such as hydrocarbons cater to the industry specific applications [2]. Research in hydrogen production from primary energy sources, such as biomass rather than from coal and natural gas, is more appropriate to reduce the costs involved and greenhouse gas emissions. Other challenges to widespread hydrogen use include storage, distribution, and application of hydrogen. These areas provide challenges that are to be researched in the area of solid state hydrogen storage.

The U.S. Department of Energy's hydrogen initiative to transition from existing fuels to hydrogen and to introduce hydrogen fuel powered vehicles into the market, requires overcoming obstacles such as lack of infrastructure to produce, store, and apply

hydrogen at affordable costs coupled with safety issues in handling hydrogen. The targets set by the Department of Energy (DoE) in its Energy Hydrogen Program as outlined in the Hydrogen Posture Plan (2004) need to be met by 2015 to make a transition from research labs to market. The targets set by DoE for production and application are hydrogen production from alternative energy sources at a price equivalent to $1.50/gallon at 5000 psi and fuel cells that can deliver 5000 hours of service at $30-$45/KW. The targets also include the development of onboard storage materials that have a gravimetric density of more than 9wt% of hydrogen and enable a 300 mile drive range [1, 3].

Research in hydrogen storage has shown different forms of storage methods that include storing hydrogen in gas, liquid or solid state. Storage of hydrogen in the form of gas requires a large amount of space with a very low gravimetric density. Storage in liquid form can achieve greater gravimetric densities than specified targets, but the storage temperatures are unrealistic (-253°C) [4]. On the other hand, solid state hydrogen storage materials are very promising due to achievable gravimetric and volumetric density targets set by the DoE including reversibility of hydrogen storage [5]. However, its share of problems includes unfavorable thermodynamics and kinetics of hydrogen release as well as the absorption and desorption of hydrogen.

## 1.1 Background

### 1.1.1 Solid State Hydrogen Storage

Metal hydrides, chemical hydrides, boranes, amides, metal organic frameworks (MOFs) and carbon-based storage materials are researched by various groups worldwide to realize materials-based onboard hydrogen storage. Hydrogen storage in materials is governed by three mechanisms: absorption, adsorption (chemisorption and

physisorption), and chemical reaction. In MOFs and carbon-based materials, hydrogen storage is mainly due to physisorption of hydrogen that results from weak non-covalent interactions between the atoms in the complexes and hydrogen [3]. In chemical hydrides, such as sodium borohydrides ($NaBH_4$), and boranes, such as ammonia borane ($NH_3BH_3$), hydrogen stored in the materials can be obtained by a chemical reaction, and the refueling with hydrogen should be done off-board by reversing the chemical reaction [3]. Metal hydrides are formed by hydriding reactions of metals through dissociative chemisorption of hydrogen [6]. Metal hydrides are three dimensional lattices with metallic cations and hydrides present as anions occupying interstitial sites in the metal complex. The metal-hydrogen complexes are formed through ionic bonding in some hydrides that are categorized as high temperature hydrides, such as magnesium hydride ($MgH_2$), and are formed due to covalent bonding in low-temperature hydrides [4]. Complex metal hydrides are a class of metal hydrides with hydrogens bonded covalently to one metallic species and the stability of the lattice is governed by another metallic species, such as sodium aluminum hydride or sodium alanate ($NaAlH_4$). Complex metal hydrides of type $M_x(AH_y)$, is formed by metallic cations ($M_x^{x+}$) with anions as molecular species containing hydrides bonded to a different metallic species (A). The interactions among the anionic molecular species are reported to be covalent and interactions that exist between the metal cations and the anionic complexes are reported to be ionic. Hydrogen is obtained from metal hydrides and amides by elevating the temperature to produce thermal effects to desorb hydrogen. Refueling of hydrogen in metal hydrides is done by applying pressure and temperature. Besides the above three materials for solid state hydrogen storage, new materials and concepts of hydrogen storage that are under

research include nanostructured materials, amine borane complexes, metal perhydrides, clathrates, lithium nitride, and irradiation activation of materials [7].

### 1.1.2 Metal Hydrides

Though metal hydrides are potential sources of solid state hydrogen storage, practical usage in transportation applications is limited by the slow hydrogen absorption/desorption kinetics, high temperatures for desorption, and high pressures for absorption. An early breakthrough in using complex metal hydrides as hydrogen storage materials is from the research on sodium alanates by Bogdanovic et al., in 1997 [8], who demonstrated reversible hydrogen storage upon transition metal catalysis. Since then numerous research efforts have been directed towards using sodium alanates as well as other complex light metal hydrides such as lithium borohydrides ($LiBH_4$) and lithium alanates ($LiAlH_4$). Figure 1.1 shows the progress of research on metal hydrides as published by Thomas et al. in the report by US DoE in 2007 [3]. In Figure 1.1, materials that are inside the dashed line box satisfy DoE targets of temperature for hydrogen release and gravimetric density of hydrogen to be used for onboard hydrogen storage. All the metal hydrides that are plotted require either require high temperatures for hydrogen release or have a lower gravimetric density compared to targets set by DoE. Besides the requirement of high temperatures for hydrogen release, hydrogen uptake by pristine metal hydrides requires very high pressures. Along with these limitations, highly ordered metal complexes result in very slow kinetics of hydrogen ab/desorption.
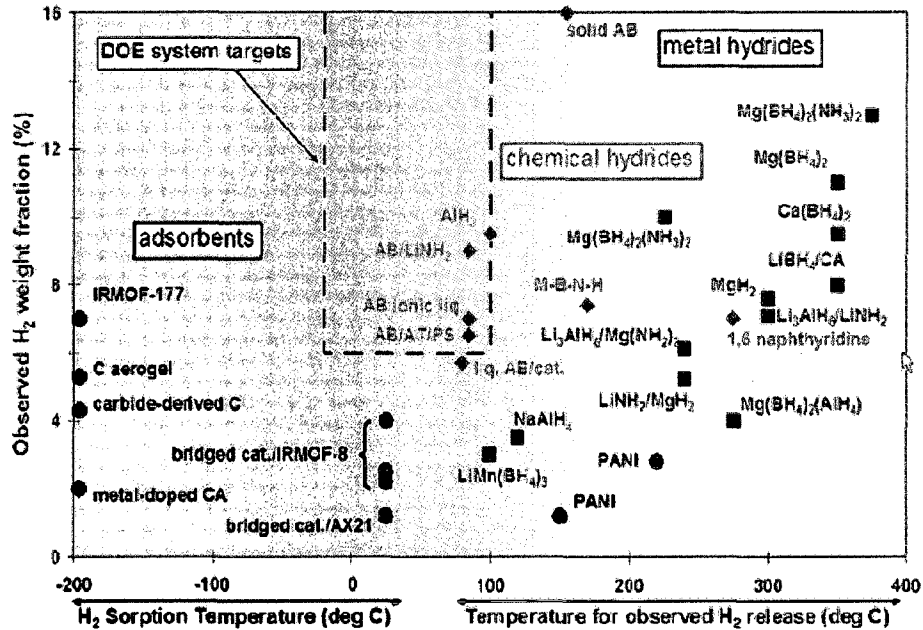
Figure 1.1 Research progress in solid state hydrogen storage with observed weight fraction plotted as a function of temperature for hydrogen release [3].

Transition metal doped metal hydrides as proposed by Bogdanovic et al., [8] offer a solution to improve unfavorable thermodynamics of hydrogen desorption in metal hydrides. Metal hydrides can be doped by transition metals either in liquid state or solid state. Bogdanovic and Schwickardi [8] demonstrated reversibility of hydrogen desorption in sodium alanates at near room temperatures in the order of 33°C upon liquid state doping of sodium alanates with transition metal salts such as $TiCl_3$. Further studies by Gross et al., [9] have shown similar results by solid state doping of $NaAlH_4$ with $TiCl_3$. Doping sodium alanates with $TiCl_3$ have also shown improvement in kinetics of hydrogen ab/desorption, but the total recoverable hydrogen from sodium alanates dropped to 4wt% compared to the theoretical 5.6wt%. However, transition metal doped metal hydrides are still under investigation and are believed to be a good alternative for onboard hydrogen storage. Another possibility for improved thermodynamics of metal hydrides stems from the pioneering work on destabilizing metal hydrides proposed by

Reilly and Wiswall [10, 11] and further demonstrated by Vajo et al., [12] on destabilized MgH$_2$ and LiH using Si. In destabilized metal hydrides such as MgH$_2$/Si or LiH/Si, destabilizer compounds form alloys with metallic species in their hydrogenated or dehydrogenated states. Enthalpy of alloy formation thereby leading to hydrogen desorption is lower compared to the decomposition of pristine metal hydrides to produce hydrogen. Hence destabilized metal hydrides are also considered as possible materials for onboard hydrogen storage. However, improvement in kinetics is not demonstrated in the pioneering work.

Research on various metal hydrides listed in the recent progress report published by DoE in 2008 [7] include investigating doped and destabilized calcium borohydrides, magnesium borohydrides, Li-Mg-B-N systems, Li-Mg-N systems, lithium amides and imides, tuned nano phase materials, Li-AB (Lithium doped ammonia boranes) and catalyzed nano frameworks of complex metal hydrides [7]. The emphasis of this dissertation research is to study the thermodynamic and kinetic behavior of sodium alanates. Though sodium alanates does not meet the specified DoE requirements, this research program still supports the studies on sodium alanates to provide a solid fundamental understanding of pristine and transition metal doped NaAlH$_4$ that can later be applied to improved types of metal hydrides.

### 1.1.3 Sodium Aluminum Hydride (NaAlH$_4$)

Sodium aluminum hydride (sodium alanate) is one of the most researched light metal hydrides after the reported observations on pristine and transition metal doped sodium alanates by Bogdanovic and Schwickardi [8]. The reversible hydrogenation capacity of the sodium aluminum hydride is enhanced after doping, and the reversible hydrogenation reactions reported [8, 13, 14] are

$$NaAlH_4 \overset{3.7wt\%}{\leftrightarrow} \frac{1}{3}Na_3AlH_6 + \frac{2}{3}Al + H_2 \uparrow \qquad \text{(Eq. 1.1)}$$

$$\frac{1}{3}Na_3AlH_6 \overset{1.9wt\%}{\leftrightarrow} NaH + \frac{1}{3}Al + \frac{1}{2}H_2 \uparrow \qquad \text{(Eq. 1.2)}$$
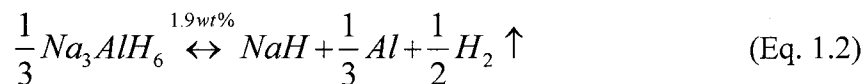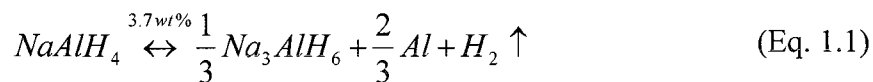
Following the pioneering work by Bogdanović and schwickardi in 1997 [8], further research on development of Ti-doped $NaAlH_4$ is carried out by Bogdanovic et al., [13, 14] Jensen and Gross, [15] Gross et al., [9] and Sandrock et al., [16] from 1997-2002. In 2003, Anton [17] showed that titanium salts are preferred over all the transition metal dopants. Great progress is seen in this area; however, a few questions remain unanswered. First is the position of transition metal dopants in the sodium aluminum hydride lattice. This position is still debated in literature, and various studies have been published from 2003-2008 addressing the position of Ti dopants in $NaAlH_4$ lattice. The second question is the role of titanium dopants in improved thermodynamics of hydrogen desorption in Ti-doped $NaAlH_4$. Though it is accepted in the literature that the formation of TiAl alloys (Ti-Al and $TiAl_3$) is favorable, reaction pathways are not clearly established. Furthermore, the source of aluminum for Ti-Al alloy formation is not clearly understood. The third question in this area is the role of titanium dopants in improved kinetics of hydrogen ab/desorption in Ti-doped sodium alanates. This dissertation study addresses the three longstanding questions by applying theoretical methods to understand the mechanisms of hydrogen desorption in pristine and Ti-doped sodium alanates. The next sections provide a review of published literature addressing the three questions.

### 1.1.3.1 Position of Ti Dopants

NMR studies by Sun et al., [18] and dry doping followed by X-ray diffraction studies by Gross et al., [19] suggested Ti substitution at native Na lattice sites where the presence of Ti at interstitial sites and on surface is reported by Baldé et al., [20] from their XANES and EXAFS study. Combined neutron inelastic scattering studies and first principle calculations by Iniguez et al., [21] reported the substitution of Ti at the native Na sites in the lattice to be energetically favorable followed by the metal-hydrogen interactions resulting in weakening of Al-H bonds in $AlH_4^-$ complexes. Ozolins et al., [22] reported a little or no change in the lattice after doping with titanium from their experimental observations. Contradicting the previous observations, Lee et al., [23] from their theoretical studies, reported a decrease in lattice parameters due to the substitution of Ti at the lattice sites of either Na or Al. They also reported substitution of Ti in Na or Al sites is found thermodynamically unfavorable whereas formation of $TiAl_3$ is found thermodynamically favorable. Studies by Kiyobayashi et al., [24] reported the distribution and diffusion of dopants are the rate limiting factors in dehydrogenation reactions. Arroyo et al., [25] reported improved kinetics by partial substitution of Ti at Na and Al sites in the lattice followed by theoretical studies by Løvvik and Opalka, [26] suggesting native Al sites in the lattice are also favorable for Ti substitution. When the formation of NaCl due to the titanium salt used is possible, experiments show that Na sites are preferred by Ti dopant over Al sites since the overall energy required to replace Na by Ti is lower compared to the energy required to replace Al by Ti [27]. This observation is consistent with the experimental work by Fitchner et al., [28] that reported preference of Ti dopants for Na over Al sites. Vacancy mediated desorption [29] is also suggested after the formation of NaCl is reported due to titanium salt used for introducing

titanium dopants into NaAlH$_4$ reaction [22]. Inspite of these observations, the preferred sites for Ti dopant in the NaAlH$_4$ lattice are still debated in the literature.

### 1.1.3.2 Thermodynamics in Ti-doped NaAlH$_4$

To understand the improved thermodynamics after doping sodium alanates with Ti salts, compounds resulting from ball milling with titanium salts and cycling at various temperatures are extensively investigated using experiments and first principles. The formed compounds are believed to be responsible for the improved thermodynamic profiles of hydrogen desorption in Ti-doped NaAlH$_4$. This investigation shed light on various phenomena including formation of solid Ti-Al, TiAl$_3$ as well as Ti-Al-H compounds along with Al clustering.

Gross et al., [9, 30] reported the presence of metallic Al and Ti phases accompanied by partial dehydrogenation after high energy ball milling of Ti salts with NaAlH$_4$, that is not observed during ball milling of NaAlH$_4$ alone. Experimental EXAFS studies by Chaudhuri et al., [31] also showed the formation of stable intermetallic species resembling TiAl$_3$. Further investigation into hydrogenation reactions by Chaudhuri and Mukerman, [32] and Graetz et al., [33] has shown that the formation of alane clusters activated by Ti is a critical step in the formation of sodium alanates. Brinks et al., [34, 35] have shown the formation of a solid Al$_{1-x}$Ti$_x$ solution with $x{\sim}0.07$ after cycling at 160°C. Haiduć et al., [36] found an hcp-Ti(Al) solid solution after doping with TiCl$_3$, and an XRD-amorphous phase when NaAlH$_4$ was doped with Ti(OBu)$_4$. These authors have also observed that the composition of those Ti compounds is temperature dependent. At temperatures up to 175°C an amorphous Al–Ti alloy is formed, while at temperatures higher than 200°C intermetallic phases of the Al$_x$Ti form are present. Baldé et al., [20] observed 70% of titanium occupied interstitial sites on the surface, and after desorption at

different temperatures, the researchers observed different phases of TiAl intermetallics depending on the availability of Al. They also observed the formation of crystalline $TiAl_3$ after heat treatment at 475°C and amorphous $TiAl_3$ at 225°C. Studies by Léon et al., [37] observed the change in the oxidation state of Ti to zero after ball milling, and Gross et al., [19] suggested the formation of catalytically active $TiH_2$. Experimental studies by Dobbins et al., [38] using X-ray absorption spectroscopy, revealed $TiAl_3$ phase after total dehydrogenation, and $Ti^0$ and amorphous TiAl after ball milling and pre-heating of $NaAlH_4$ doped with $TiCl_3$. Besides experimental observations, theoretical studies are also employed to understand the role of Ti dopants [21, 22, 25, 26, 29, 31, 32, 39-44]. Density Functional Theory studies by Lee et al., [23] suggested that Na and Al substitution by Ti in sodium alanates is unfavorable; however, the formation of $TiAl_3$ is thermodynamically favorable. Regarding the concentration of dopant salts, Sandrock et al., [16] reported detrimental effects on hydrogen desorption in sodium alanates with increase in concentration of Ti dopants. From all these studies, the presence of one or more phases of Ti-Al compounds is expected to take part in hydrogen desorption from Ti-doped sodium alanates. In spite of all experimental and theoretical investigations on this topic, the basic role of titanium dopant in the formation of key intermetallics and thermodynamic profiles of hydrogen desorption in Ti-doped sodium alanates is still unknown.

### 1.1.3.3 Kinetics of Ti-doped NaAlH₄

Kinetics of hydrogen desorption in pristine and Ti-doped sodium alanates includes two steps. The first step is to study the diffusion mechanisms that are responsible for hydrogenation and dehydrogenation reactions in pristine $NaAlH_4$, and the second step is to study Ti-doped $NaAlH_4$ that exhibits reversibility of hydrogen storage and improved kinetics compared to pristine $NaAlH_4$.

To understand the kinetics of hydrogen desorption in pristine sodium alanates, decomposition reactions of sodium alanate to yield hydrogen are studied. Suggested progress of the first decomposition reaction is by transition from $AlH_4^-$ anion to $AlH_6^{3-}$ anion combined with nucleation and growth of Al phase [8]. Early studies by Gross et al., in 2001, on pristine and Ti-doped $NaAlH_4$ using in-situ X-ray diffraction [9] suggested the possibility of transition through long range diffusion of heavier mass species than hydrogen. This observation is further supported by recent isotope scrambling experimental studies by Bellosta et al., [45] and Lohstroh and Fitchner, [46] that indicate diffusion of hydrogen as the atomic or molecular species is unlikely to precede the diffusion of heavier mass species than hydrogen. Recent computational studies by Gunaydin et al., [47] have shown the possibility of $AlH_3$ vacancy assisted hydrogen desorption and that the formation of $AlH_3$ vacancy is favorable over the NaH vacancy formation proposed by Walters and Scogin [48].

Improved kinetics of hydrogen ab/desorption in Ti-doped $NaAlH_4$ was observed by Bogdanovic et al., [8, 14] Gross et al., [9, 30] Jensen et al., [15] and Sandrock et al., [16]. In 2003, Gross et al., [19] reported increase in kinetics of hydrogen desorption with increase in Ti halides but at the expense of reversible hydrogen capacity of the material. It is also observed that the improvement in kinetics is independent of the type of halide with the exception of $TiCl_2$, and similar improvements were also observed after doping with large amounts of $TiH_2$ [19]. Mazjoub et al., [49] reported improved kinetics is independent of the valence state of Ti precursor. They also reported atomically dispersed Ti as well as formed $TiAl_3$ alloys are responsible for reversible hydrogen storage as well as improved kinetics of hydrogen desorption. The study by Luo and Gross, [50]

suggested kinetic models of decomposition and formation of pristine and Ti-doped sodium alanates show that at a fixed pressure, an increase in temperature is advantageous in formation and improved kinetics. Observations by Brinks et al., [34, 35] showed solid Al-Ti solution followed by Haiduć et al., [36] reporting the formed phases of TiAl depend on cycling at various temperatures. Other researchers have suggested the surface morphology of the doped particles also affect the kinetics of hydrogen desorption [51, 52]. Wang et al., [53] reported improvements in dehydrogenation kinetics by introduction of co-dopants like zirconium in addition to Ti. In spite of all of these observations nothing conclusive has been reported yet.

## 1.2 <u>Objectives</u>

The main goal of this dissertation study is to address all the three questions laid out in the previous section about the position of transition metal dopants in the sodium aluminum hydride lattice, various resulting compounds from titanium doping in sodium alanates, and improved thermodynamics and kinetics of hydrogen ab/desorption in Ti-doped sodium alanates. Hence the objectives of this dissertation study are

1. Study the structural, electronic, and vibrational properties of pristine $NaAlH_4$ using DFT techniques.

2. Identify the possible sites for Titanium dopants in $NaAlH_4$ lattice to investigate the possible conformations of Ti-doped $NaAlH_4$ that can further be analyzed to determine the role of Ti dopants.

3. Identify the possible compounds resulting from titanium doping in sodium alanates to elucidate the role of Ti in formation of various Ti-Al alloys and Ti-Al-H compounds.

4. Study the dynamics of Ti-Al and Ti-Al-H compounds at elevated temperatures to explain the underlying phenomenon of existence of those compounds during thermally induced hydrogen desorption.

5. Identify the thermodynamic pathways for hydrogen desorption in pristine $NaAlH_4$ and formation of Ti-Al alloys in Ti-doped $NaAlH_4$ to investigate the most favorable reaction pathways and understand the thermodynamic profiles of hydrogen desorption in Ti-doped sodium alanates.

6. Understand the kinetics of hydrogen desorption in pristine $NaAlH_4$ to identify the rate limiting steps and elucidate the role of Ti dopants in improved kinetics of Ti-doped $NaAlH_4$.

The following Chapters of this dissertation discuss the approach and results obtained from our calculations fulfilling the above listed objectives. In Chapter 2, methods used in this study are discussed in general as well as specifically regarding implementation in the software used. Chapter 3 presents results from first principles calculations determining the ground state structure; electronic properties such as electronic density of states, band structure, and charge population analysis on the atomic/ionic species; vibrational properties; and thermodynamic properties of $NaAlH_4$. Extended lattice and surface models used in subsequent Chapters to study the effects of Ti dopants, thermodynamics, and kinetics are also presented. In Chapter 4, results obtained from our calculations to understand the thermodynamics and kinetics of hydrogen desorption from pristine sodium alanates, thereby identifying the underlying mechanisms that need to be addressed, are discussed. Chapter 5 focuses on the study of the preferred sites for titanium dopants after solid state doping or mechanical milling and

after elevating the temperature of the doped material. In Chapter 5, changes in the electronic structure of $NaAlH_4$ due to Ti dopants and identification of various intermediate and minimum energy configurations of formed intermetallics are presented. In addition, the charge distribution analysis presented in Chapter 5 provides the atomistic details of the formed intermetallics and local environment around dopant ions. Time dependent dynamics of Ti doped $NaAlH_4$ at elevated temperatures is also explained. Overall, Chapter 5 is aimed at providing detailed atomistic information about the formed intermetallics and local environment around Ti dopant. Results discussed in Chapter 6 include the favorable thermodynamic pathways for Ti-Al alloy formation in Ti-doped sodium alanates as well as calculations elucidating the role of Ti dopant in improved kinetics of hydrogen desorption in Ti-doped sodium alanates.

# CHAPTER 2

# SIMULATION TECHNIQUES AND CONCEPTS

# IN MODELING PERIODIC SYSTEMS

## 2.1 Simulation Techniques

Computational chemistry methods provide a prior insight into the molecules of interest in good agreement with experimental information. Though computational chemistry was limited by the computational power in past decades, it is now overcome by the development of faster, more accurate and more reliable computing resources. Parallel and distributed computing combined with low cost work stations and high end networks enable computational chemistry to be applied to the molecular/nanosystems development. Computational methods that are typically applied in this field of study are based on classical physics and quantum mechanics. The evaluating tools for the interactions of the materials at the molecular level, such as density functional theory (DFT)/molecular mechanics (MM)/molecular dynamics (MD), have grown to a greater extent increasing the accuracy and precision of the simulations. Quantum mechanical computational techniques, such as density functional theory (DFT), have been successfully used for evaluating molecular properties such as energy, optimum conformation, reaction paths and thermal behavior [54-61].

Most of the calculations in this dissertation related to total energy, electronic properties, and thermodynamics are performed using DFT formalism extended to infinite periodic models as implemented in CASTEP, and the remaining calculations related to kinetics are performed using DFT formalism as implemented in $DMoL^3$ modules in Materials Studio by Accelrys Inc. Hence, further discussion is related to the background theory, concepts in modeling periodic systems, and implementation of various schemes in CASTEP and $DMoL^3$ modules.

### 2.1.1 Quantum Mechanics

The word Quantum was first used by Max Planck in 1900s and the term quantum mechanics was first coined by Born in 1924. In mid 1920s, two formulations of quantum mechanics were postulated by Werner Heisenberg and Erwin Schrödinger. Erwin Schrödinger's formulation of quantum mechanics or wave mechanics is based on the wave-particle duality proposed by Louis de Broglie [62]. Heisenberg's formalism is based on the theory of matrices and is called matrix mechanics. Schrödinger has shown that the concurrently developed theories by Heisenberg and himself are mathematically equivalent. Later P. A. M Dirac and Jordan's transformation theory clarified the connection between two methods. In modern quantum theory Schrödinger's formulation of quantum mechanics is used [62, 63].

The basic postulate of quantum mechanics by Schrödinger is for any N-particle system there exists a state function or a wavefunction, $\Psi(r)$, and applying appropriate operators on that function would result in the observable properties of the system. Wavefunctions must be continuous and single valued. The square of the wavefunction is the probability density, and its integral over the state space must be equal to one which

requires the wavefunction to be quadratically integrable. The operator that acts on a wavefunction and returns the energy of the system is a Hamiltonian operator [54].

### 2.1.1.1 Schrödinger Equation

The energy of a molecular system can be obtained by solving the time independent non-relativistic Schrödinger equation represented as:

$$H(r)\Psi(r) = E\Psi(r),$$
(Eq. 2.1)

where $H(r)$ is the Hamiltonian operator, $\Psi(r)$ is the wavefunction, $E$ is the energy of the molecular system, and $r$ is the position vector given by $x\boldsymbol{i}+y\boldsymbol{j}+z\boldsymbol{k}$.

The total Hamiltonian operator includes the kinetic as well as potential energies of all particles (electrons and nuclei) and is expressed as:

$$\hat{H}_{TOT} = \overbrace{\frac{-\hbar^2}{8\pi^2}\sum_A \frac{1}{m_A}\nabla_A^2 + \frac{-\hbar^2}{8\pi^2}\sum_i \frac{1}{m_i}\nabla_i^2}^{\underbrace{\phantom{xxxxxxxxxxxxxxxxxxxxxxxxx}}_{\text{Kinetic Energy}}} \overbrace{- \sum_i\sum_A \frac{Z_A e^2}{r_{iA}} + \sum_i\sum_{<j}\left(\frac{e^2}{r_{ij}}\right) + \sum_A\sum_{<B}\left(\frac{Z_A Z_B e^2}{R_{AB}}\right)}^{\underbrace{\phantom{xxxxxxxxxxxxxxxxxxxxxxxxx}}_{\text{Potential Energy}}},$$

(Eq. 2.2)

where $\hbar$ is Planck's constant divided by $2\pi$, $m$ is the mass of the particle, $Z$ is the atomic number, $R_{AB}$ is the distance between particles A and B, $e$ is the charge on the electron, and $r_{iA}$ and $r_{iB}$ are distances between electrons and nuclei [64, 65]. The potential energy of all particles includes the nuclei-nuclei interaction, electron-electron interaction, and electron-nuclei interaction energies. Kinetic energy comprises the kinetic energy of nuclei and kinetic energy of electrons.

In Eq. (2.2), the first and second terms represent the kinetic energies of nuclei and electrons, respectively. The third term represents the electron-nuclei interaction energy, fourth term represents the electron-electron interactions, and the fifth term represents the

nuclei-nuclei interactions. Born-Oppenheimer approximation decouples the nuclear motion from electronic motion based on the fact that the kinetic energy of the nuclei is negligible when compared to the kinetic energy of electrons since the nuclei are much heavier than the electrons making the first term in the Eq. (2.2) equal to zero. Applying Born-Oppenheimer approximation, the Schrödinger equation is reduced to

$$\hat{H}_{elec}\,\Psi(r) = E\Psi(r),$$
(Eq.2.3)

where $\hat{H}_{elec}$ is the electronic Hamiltonian that consists of potential energy and the kinetic energy of electrons, and $\Psi(r)$ is the wavefunction. To differentiate between one electron and many electron wavefunctions, one electron wavefunction is denoted as $\psi(r)$, and the many electron wavefunction is denoted as $\Psi(r)$ and, the many electron wavefunction is expressed as a Hartree product of one electron wavefunctions ($\Psi(r) = \psi_1(r)\psi_2(r)..\psi_N(r)$).

Potential energy surface (PES) represents the plot of potential energies of different nuclear configurations. Each point on the PES represents the energy with respect to the nuclear geometries. Once the PES is defined, the nuclear part of the Schrödinger equation is solved. For a polyatomic system with N nuclei, 3N coordinates describe the geometry. Three coordinates describe the translation of the molecule, and three coordinates describe the rotation of the molecule, and 3N-6 coordinates describe the relative movement of nuclei resulting in the geometrical changes [66]. The stationary points found on a PES may be a maximum point or a saddle point (minimum along some reaction coordinates and maximum along others) or a minimum point. The saddle point with maximum along one reaction coordinate and minimum along all others is called a

transition point. Determination of a stationary point and calculating its energy and geometry on the PES is called geometry optimization. In case of the transition point, it is called transition state optimization and in the case of the minimum it is called energy minimization. The methods used to solve the electronic Schrödinger equation are often referred to as electronic structure methods.

## 2.1.1.2 Density Functional Theory

The three main divisions of electronic structure methods are *ab initio,* semi-empirical, and density functional theory. *Ab initio*, as the name implies, uses the first principles and employs only physical constants in the calculations on molecular systems. Semi-empirical calculations use numerical parameters for some integrals and ignore some integrals in the Hamiltonian. Both *ab initio* and semi-empirical methods are based on predicting the observables using molecular wavefunctions. Density functional theory (DFT) is based on electron probability density function or electronic density function rather than a wavefunction [54, 56, 57]. DFT formalism is used in all the calculations in this study. Hence, the theory behind DFT is further discussed in this Chapter.

Electronic energy and ground state properties of molecules in DFT calculations are based on the Kohn-Sham approach that defines the ground state properties as a function of the electron density or charge density. The energy functional in DFT is of the form:

$$E[\rho(r)] = E_{KE}[\rho(r)] + E_{NE}[\rho(r)] + E_H[\rho(r)] + E_{XC}[\rho(r)] \qquad \text{(Eq. 2.4)}$$

It is written as a sum of contributions from non-interacting electrons $E_{KE}[\rho(r)]$, electron-nuclei interaction $E_{NE}[\rho(r)]$, classical electron-electron interactions $E_H[\rho(r)]$, and corrections to the kinetic and electron-electron repulsions in the real interacting

system $E_{XC}[\rho(r)]$. $E_H[\rho(r)]$ is also called Hartree electrostatic energy, which arises from the columbic interaction between two charge densities. The wavefunction $\Phi(r)$ is constructed as a Slater determinant of one electron functions or molecular orbitals $\phi(r)$ as in molecular orbital theory, and the charge density is constructed as a sum of squared densities of molecular orbitals, $\rho(r) = \sum_i^N |\phi_i(r)|^2$, under the constraint that the molecular orbitals are orthonormal. In terms of electronic density, the total energy is expressed as:

$$E[\rho(r)] = \sum_i^N \left\langle \phi_i \left| -\frac{\nabla^2}{2} \right| \phi_i \right\rangle + \sum_i^N \sum_k^N \left\langle \rho(r_i) \left| \frac{Z}{r_k - r_i} \right| \right\rangle + \frac{1}{2} \sum_i^N \left\langle \rho(r_i) \int \frac{\rho(r')}{|r_i - r'|} dr' \right\rangle + E_{XC}[\rho(r)],$$

(Eq. 2.5)

where the first term is the kinetic energy, the second term is electron-nuclei interactions, the third term represents electron-electron repulsion, and the fourth term is the exchange-correlation energy. To find the ground state energy, variations in total energy must be optimized against the variations in electronic density. Since molecular orbitals or KS orbitals that correspond to the ground state energy satisfy the Schrodinger equation, the total Hamiltonian can be written as:

$$H = \sum_{i=1i}^N h_i^{KS} |\phi_i\rangle,$$

(Eq. 2.6)

where $h_i^{KS}$ is the Kohn-Sham one-particle operator and is expressed as:

$$h_i^{KS} = -\frac{1}{2}\nabla_i^2 + \sum_k^N \frac{Z_k}{|r_k - r_i|} + \int \frac{\rho(r')}{|r_i - r'|} dr' + V_{XC},$$

(Eq. 2.7)

where, $V_{XC}$ is the exchange correlation functional. Expressing the molecular orbitals as a linear combination of atomic basis functions, $\phi_i = \sum_\mu C_{i\mu}\varphi_\mu$, energy

eigenvalues are obtained by solving the secular equation of the form $HC = ESC$ where

the elements of resonance and overlap integrals are equal to $H_{\mu\nu} = \left\langle \varphi_\mu(r_i) \middle| h_i^{KS} \middle| \varphi_\nu(r_i) \right\rangle$

and $S_{\mu\nu} = \left\langle \varphi_\mu(r_i) \middle| \varphi_\nu(r_i) \right\rangle$ respectively.

Two approximations are proposed for determining exchange - correlation

potential in molecular systems: local density approximation (LDA) and non-local density

or generalized gradient approximation (GGA). Local spin density approximation (LSDA

or LDA) is based on the electron density in uniform electron gas [67-69]. This approach

was proven useful in many cases, but in the polyatomic systems with non-uniform

electron density distribution, non-local functionals also need to be used besides local

functionals. This approach is called gradient-corrected approximation functional (GGA).

Non-local functionals depend on the gradient of density in space [70, 71].

Implementation of general concepts of DFT related to charge density, DFT

functionals, and SCF methods discussed above in the previous section are the same as in

other computational tools. CASTEP has provisions for implementing local density,

gradient corrected density, and non-local density approximation methods for calculating

exchange-correlation term in the Hamiltonian. Various schemes implemented are PW91

[67], PBE [72], RPBE [73], and WC [74] functionals as proposed by White et al., [75]. In

this study all the calculations are done using gradient-corrected density functionals

(PW91).

In DMoL[3], functionals implemented to estimate the exchange correlation energy

include VWN [68], PWC [67], PW91 [67], PBE [72], BLYP [76, 77], BOP [78], HCTH

[79], and BP [67, 76]. In this study, PW91 correlation functional is used in all

calculations.

## 2.1.2 Transition State Theory

Transition state theory predicts the rate of a chemical reaction by predicting the energy difference between the activated or transition complex connecting reactants and products along a particular reaction coordinate and the reactants on the potential energy surface. Activated complex is a relatively high energy super-molecule in equilibrium with reactants and with information related to transformation from reactants to products. The rate constant of the reaction is given by the product of rate at which the products are formed ($\hat{k}$) from activated complex and the equilibrium constant of reaction ($K_c$) that proceeds from reactants to the activated complex. Using macroscopic thermodynamic relationships, equilibrium constant is related to the free energy of activation by Arrhenius law ($\Delta G = -RT \ln(K_c)$). Another approach for rate constants formulation is using the concepts of statistical thermodynamics [80]. According to this theory, one of the vibrational modes is associated with the first order rate constant ($\hat{k}$) that corresponds to the motion along the reaction coordinate from the activated complex to the products. Evaluated vibrational modes of the activated complex would result in all positive frequencies except one that has imaginary value that corresponds to the transformation [80].

In this study, we are interested in finding the free energy and enthalpy of activation for hydrogen evolution from sodium alanates. Transition state calculation as implemented in DMoL$^3$ predicts the transition path from reactants to products along a particular reaction coordinate, obtains the conformation of the activated complex that has maximum energy along the path and minimizes its energy. Geometry and electronic minimization of transition complexes is followed by further optimization and

confirmation calculations to obtain a true transition state complex that connects the reactants and products via a minimum energy path on the PES. The transition state is identified by one vibrational mode that corresponds to the transition and movement along the reaction coordinate. Free energies of reactants and activated complexes are calculated and the free energies and enthalpies of activation are determined as the difference between free energies of activated complexes and reactants.

### 2.1.2.1 Locating Transition States

The most difficult task in transition state calculations is to locate a true transition state. Many proposed methods for predicting transition states, thereby evaluating energy barriers in reactions are well suited for homogeneous fluid and gas phase transformations. Popular search methods include linear/quadratic synchronous transit (LST/QST), eigenvector following (EF), nudged elastic band (NEB) [81], dimer method [82], VTST [83].

LST/QST and EF methods are used in this study. The transition state search using the LST method proposed by Halgren and Lipscomb [84] linearly interpolates the distance between the pairs of atoms in reactants and products to generate a set of structures connecting reactants and products. Interpolation parameter varies between 0 and 1, and the internuclear distance is defined as a function of the interpolation parameter. The LST search performs a single interpolation along the proposed reaction pathway to find the structure with maximum energy along that reaction coordinate. QST methods perform constrained minimizations to obtain a transition state with higher accuracy than LST. In EF method, hessian of the located transition state using LST or QST technique is used to find the particular vibration frequency mode that connects the

reactants and products, and then the minimum energy structure along that mode is calculated.

In this study, LST/QST method followed by optimization is used to obtain the transition states. The LST/QST method locates the transition state first by linear interpolation followed by applying the QST technique to find the transition state from the one that was obtained using LST. The obtained transition state through LST/QST method is then minimized using conjugate gradients to search for a nearly true transition state. Conjugate gradients minimization searches for the minimum energy structure along all the conjugate directions, but still connects reactants and products to the obtained transition state from LST/QST method. Besides searching, transition state conformation is also implemented in DMoL$^3$ similar to nudged elastic band (NEB) method [81].

## 2.1.3 Molecular Dynamics

Molecular dynamics is used to study the changes in the system as a function of time and predicting static and dynamic properties of the system as a function of interactions between the atoms [85]. It is a deterministic method, which means the state of the system in future is a function of present state. MD simulations start with the definition of an initial configuration and assign velocities to the atoms based on the Maxwell-Boltzmann distribution. The expected kinetic energy is used to calculate the temperature of the system. Calculated temperature is used and new velocities are calculated and assigned to the atoms. Then the system proceeds by a pre-specified time step. For each time step, the forces on the atoms are calculated, and the new coordinates and velocities are found. This process is iterated until the pre-specified time limit is reached [85]. Numerical integration algorithms used in these calculations include leap frog algorithm, verlet algorithm [86], velocity-verlet algorithm [87], predictor-corrector

algorithms [88] and Beeman algorithm [89]. The Verlet algorithm uses the positional and acceleration data at the present time $t$ and positional and acceleration data at time $t-\delta t$ to calculate the positional and velocity data at time $t+\delta t$. Advantages of this basic algorithm includes integration of only the positional data and inexpensive computation since force evaluation is done only once per integration cycle. Limitations include large errors in predicted velocities. Improvement to this algorithm is to take the positional data from present time $t$ and velocity data from time $t - (\delta/2*t)$ to compute the forces at present time $t$ and velocities at time $t + (\delta/2*t)$. This algorithm is known as the leap frog algorithm. This algorithm has some improved performance over the basic algorithm, but still the calculated velocities are approximate. The velocity-verlet algorithm uses the positional, acceleration and velocities at time $t$ to compute the positional, acceleration, and velocities at time $t+\delta t$. This algorithm is computationally expensive but more precise than the previous algorithms.

Conventional molecular dynamics describes the potential energy of a system as a function of nuclear coordinates based on the force field. Force field based MD schemes determine the energy based on the nuclear positions treating the atoms as hard spheres. Forcefield methods take care of the interactions due to bond stretching, angle bending, and torsions in the molecular geometry as well as the non bonded interactions between the atoms. In this scheme, acceleration of the atoms are derived by using Newton's second law ($F = m \cdot a$), where $F$ is the force on the atom, obtained from force field and $m$ is the mass of the atom, and $a$ is the acceleration, which is a second derivative of the displacement of the atoms.

DFT/MD simulations are essentially similar to conventional force-field based MD methods except the energy and forces between the atoms after each step is calculated using DFT formalism. Electronic minimization is performed after each MD step that provides an accurate representation of forces and energy of the system. However, this procedure is computationally more expensive than the conventional MD due to energy and force evaluation using DFT after each step. Algorithms used for integrating equations of motion are similar in both conventional and DFT/MD schemes. CASTEP uses the velocity-verlet algorithm for integrating equations of motion in MD. It also uses wavefunction extrapolation [90] and charge density extrapolation [91] schemes between MD steps to provide a good starting configuration for electronic minimization in succeeding steps.

Ensembles available in CASTEP that are used in this study are micro-canonical (NVE-constant number of particles, constant volume, and constant energy) and canonical ensembles (NVT-constant number of particles, constant volume, and constant temperature). A variety of structural, energetic, and dynamic properties can then be calculated from the averages or the fluctuations of these quantities over the ensemble generated. NVE ensemble is used in calculations to explore the dynamics of the systems in a constant-energy conformational space. NVT ensemble is used to study the dynamics of systems under the influence of fixed temperature keeping the volume and chemical potential of the system unchanged.

## 2.2 Concepts in Modeling Periodic Systems

Periodic systems or crystals are infinite repetitions of identical structural units in space. The periodic array where the repeated units are arranged is called a Bravais lattice.

A 3D Bravais lattice consists of all points with position vectors $R$ where $R = n_1 \cdot a_1 + n_2 \cdot a_2 + n_3 \cdot a_3$; $n_1$, $n_2$ and $n_3$ are integers and $a_1$, $a_2$ and $a_3$ are the primitive lattice vectors. A primitive cell is the minimum volume enclosed by the three vectors in the lattice and is called a primitive unit cell if it has only one lattice point inside the cell. A conventional cell or a unit cell is a set of primitive cells that when translated through some subset of vectors of a Bravais lattice, fill the entire space. Dimensions of the unit cell or conventional cell are referred to as lattice parameters or lattice constants. Primitive cells can be chosen in any manner, and the most common choice is a Wigner-Seitz cell. A Wigner-Seitz cell about a lattice point is the region around that lattice point that is closer to that lattice point compared to any other lattice point [92, 93].

The Fourier space associated with the real lattice is known as a reciprocal lattice. Reciprocal lattice is important in all the studies related to periodic systems. Primitive reciprocal lattice vectors are constructed from primitive vectors of the real lattice, and the wave vector $k$ associated with the reciprocal lattice is equal to $k = m_1 \cdot b_1 + m_2 \cdot b_2 + m_3 \cdot b_3$; $m_1$, $m_2$ and $m_3$ are integers, and $b_1$, $b_2$ and $b_3$ are the primitive reciprocal lattice vectors. A set of all wave vectors $K$ that yield plane waves with the periodicity of a given Bravais lattice is called reciprocal lattice. Wigner-Seitz cell of the reciprocal lattice is called the Brillouin zone. It is the smallest volume enclosed by the planes that are perpendicular bisectors of the reciprocal lattice vectors drawn from a lattice point. Origin (0,0,0) of the first Brillouin zone is known as $\Gamma$ point, and the high symmetry directions in the Brillouin zone correspond to the vectors from the origin along the corners or mid-points of the edges of the polyhedron formed from the bisecting planes

of the reciprocal vectors. Analytic studies on all the solid state materials are done with reference to the Brillouin zone of the reciprocal lattice of that particular crystal [92, 93].

For applying the computational techniques to study periodic systems, an infinite periodic system must be represented as a finite length crystal or a surface. All the molecules must be studied by enclosing them in a box and imposing periodic boundary conditions [94].

## 2.2.1 Plane Wave Basis

Basis functions that describe the wavefunction must have the translation symmetry of the periodic system: $\phi(r) = \phi(r + R)$ where, $r$ is any point in the periodic system, and $R$ is the position vector. Hence, the wavefunction is constructed from a set of plane waves with periodicity equal to that of the lattice [92, 93].

$$\Psi(k,r) = e^{i \cdot k \cdot R} \phi(r)_,$$
(Eq. 2.8)

where $k$ and $R$ determine the number of vectors required to sample the whole space. In principle, infinite numbers of vectors are needed to sample the whole space, but in practice, a kinetic energy cutoff value is chosen to represent the relevant sampling space to accurately represent the wavefunction. According to the Bloch's theorem [92, 93], wavefunction in a periodic system can be expressed as a product of a wave-like part and a cell-periodic part. The cell-periodic part is further expressed as a set of plane waves with reciprocal lattice vectors ($G$) as its wave vectors [95]. The electronic wavefunction is thus expressed as:

$$\Psi(k + G,r) = \sum C_{i,k+G} e^{i \cdot (k+G) \cdot R}$$
(Eq. 2.9)

By expressing it in terms of reciprocal wave vectors, a wavefunction (Eq. (2.9)) is expressed by infinite number of reciprocal space vectors in the first Brillouin zone and

infinite k-points. Plane waves with smaller kinetic energy are of more importance than the ones with higher kinetic energies. Hence a kinetic energy cutoff value is defined, and plane waves with kinetic energies less than the defined cutoff value are considered. However, multiple calculations are done in practice to check for the energy convergence within the required tolerance when compared over different kinetic energy cutoff values. Infinite k-points that are required to sample the Brillouin zone can be reduced to only a few numbers of special points in the irreducible segment of the Brillouin zone since the electronic wavefunctions at k-points that are close together and that are symmetrical images of the k-points in the irreducible segment, are almost identical. One of the most popular schemes is Monkhorst-Pack method [96] for generating a uniform grid of k-points in the Brillouin zone. Similar to the number of plane waves, energy convergence is checked against the density for k-point mesh in practice to determine the optimum k-point sampling of Brillouin zone.

### 2.2.2 Pseudopotentials

Pseudopotentials are one of the important aspects of plane-wave total energy methods. Using all-electron functions would tremendously increase the computational cost as the electron wavefunctions near the core of the atoms oscillate rapidly and the number of plane waves to represent the oscillations increases enormously. Hence, the nucleus along with the tightly bound electrons near the core is considered to be frozen, and valence electrons are treated explicitly. Pseudopotentials replace the strong coulomb potential near the core by a weaker pseudopotential which acts on the constructed pseudo wavefunctions to represent the electrons (Figure 2.1). This approximation is valid since only the valence electrons take part in inter-atomic interactions that describes most of the chemically bonded systems [97-99].
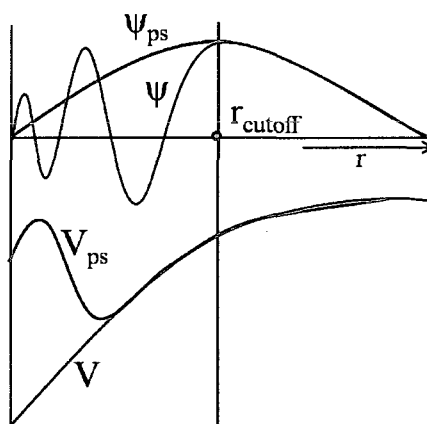
Figure 2.1 Pictorial representation of a pseudopotential. Strong columbic potential near the nucleus is replaced by a weaker pseudopotential and with pseudo wavefunctions with no nodes inside the cutoff radius [95].

A cutoff radius or core radius is defined in pseudopotential generation. Outside the core radius, the generated pseudo wavefunctions and pseudopotential must reproduce the original wavefunction and potential. Pseudopotentials are represented as:

$$V_{ps} = V_{loc} + \sum_{l,m} (V_l - V_{loc}) \hat{P}_{l,m} ,$$  (Eq. 2.10)

where $V_{loc}$ is the arbitrary local potential, and $V_l$ is potential for angular momentum $l$ [100]. When $V_l = V_{loc}$, then the pseudopotential is called a local pseudopotential, and when they are different, the pseudopotential is known as a non-local pseudopotential. Pseudopotentials are generated using all-electron DFT methods for an isolated atom. True wavefunctions are first calculated and are modified in the core region to replace the nodes by softer pseudo wavefunctions with the norm-conservation constraint [101]. Using Schrödinger equation, the pseudopotential is calculated with a particular cutoff radius or core radius. Thus, the generated pseudopotentials can be transferred to the particular atom in any chemical system [102, 103]. Pseudopotentials are also measured on the basis of a degree of hardness. If a small number of Fourier

components are needed to accurately represent the pseudopotential, it is considered to be soft; otherwise, it is hard.

Two types of pseudopotentials are used in this study: norm-conserving [102, 104] and ultrasoft [105]. Conditions for norm-conserving pseudopotentials are accurate match between the real and pseudopotentials, wavefunctions, charge densities and squared amplitudes of pseudo wavefunctions over the entire region [101]. Norm-conserving pseudopotentials are generally harder than ultrasoft pseudopotentials. Ultrasoft scheme reduces the hardness of pseudopotentials by using a few Fourier coefficients and relaxing the norm-conserving criterion over the core region [105]. Due to the softer nature of ultrasoft pseudopotentials, the kinetic energy cutoff is usually less than that specified in norm-conserving case.

Non-linear core correction (NLCC) to the pseudopotentials must be included when the core and valence shells are close together, and the exchange-correlation energy is non-linear [106]. These non-linear core corrections are introduced by adding the core charge to the valence charge for exchange-correlation potential and keeping only the core charge for the remaining calculations. In CASTEP, partial core correction is used that replaces the full core density by a function of the density that approximates the full core density outside a certain radius. NLCC is important in case of magnetic systems and spin non-polarized systems with shallow semi core states.

## 2.2.3 Electronic and Geometry Minimization

Electronic minimization options in CASTEP include both all-bands and density mixing schemes. Density mixing schemes [107] minimize the sum of electronic eigenvalues in a fixed potential unlike the all bands method [95] where the expansion coefficients of plane wave basis functions are minimized to obtain the minimum energy.

In the density mixing scheme, the new charge density obtained at the end of the minimization is mixed with the initial density, and the process is repeated until convergence is reached. The Pulay density mixing scheme is used in this study. In this method, input charge densities and residual vectors are stored, and the input density is obtained in each step by a linear combination of previous charge densities. A new density obtained after each step minimizes the norm of the residual vector subject to number of electrons. This density mixing scheme depends on a number of previous optimization steps, mixing amplitude, and the cutoff wave vector [107]. Convergence of density mixing schemes is superior over all bands method for both insulators and metals [107]. In all the calculations, the mixing amplitude of 0.8 and optimization history of 20 steps is used.

Predicting optimum geometry of the initial configurations requires minimization of both cell and atomic coordinates. The Broyden-Fletcher-Goldfarb-Shanno (BFGS) minimizer is used in all the calculations, and that minimizer uses an initial hessian in mixed space of cell and atomic coordinates and recursively updates the hessian during optimization [108]. Other implemented schemes include damped MD involving minimization of internal coordinates with cell parameters fixed.

## 2.2.4 Electronic Properties

Electronic properties such as bond population analysis, band structure, electronic total, and local DOS, and electron density maps can be obtained from calculations in CASTEP as a part of geometry optimization run or a separate calculation on a selected structure requesting properties.

## 2.2.4.1 Bond Population Analysis

Bond population analysis schemes implemented in CASTEP are used to determine the strength of the bonds in the observed multi atomic complexes. In molecular orbital methods, molecular orbitals formed from the linear combination of atomic orbitals are more localized around the atoms and provide a way to partition the electron density as a function of overlap and density matrices. In plane wave methods due to the delocalized nature of plane waves, information about localized electrons cannot be determined. In CASTEP, bond population is based on projection of plane wave states onto the generated pseudo-atomic orbitals from pseudopotentials [109] and Mülliken population analysis [110]. The quality of projection is measured by a spilling parameter that ranges between zero and one with value of one when the projected states and pseudo-atomic orbitals are orthogonal and value of zero when they are perfectly aligned [111].

Absolute values of Mülliken charges derived from bond population has little physical meaning as they are sensitive to the atomic basis functions used. However, relative values are of importance when all the configurations are represented with the same basis functions. Based on the bond population analysis, bonding character can be predicted. Its values, on a scale from -1 to 1, represent a bonding state when the overlap population values are positive and an anti-bonding state when the values are negative. Values with zero overlap indicate no significant interaction between two atoms [111]. Results presented in this study show no anti-bonding states. Hence, all the presented overlap population values are on a scale from 0 (no bond) to 1 (strong bond). Besides bonding states, covalence of the bond can also be determined since it is proportional to the overlap population. Hence, the closer the bond population to 1, the more covalent the bond between the atoms [112]. Relative overlap population between two atoms in

different compounds would indicate the degree of covalence of the same bond in different situations. Furthermore, ionicity of the bond can be indicated from the effective Mülliken charges on the participating atoms [112].

## 2.2.4.2 Born Effective Charge Tensors

Since charge on the atoms/ions is not a quantum mechanics observable quantity, one of the many available charge approximations, Mülliken population analysis, appropriates the electron density equally between the two nuclear centers of interest in evaluating the existence of bond between them. This charge approximation is not considered the most accurate prediction in evaluating charges on ions. Born effective charges are calculated in terms of response of the dipole moment of the system with respect to perturbations. Here charge calculated is a tensor that is obtained from derivatives of three Cartesian components of dipole moments with displacements in three Cartesian coordinates. Since dipole moment is a quantum mechanical observable, charge analysis based on born effective charge tensors (Z) is particularly attractive.

## 2.2.4.3 Band Structure and Density of States

Band structure calculation returns the electronic energies along high symmetry directions in the Brillouin zone. The number of properties can be deduced from band structure. Free electron bands corresponding to s and p states and narrow bands corresponding to d and f states can be identified. Bands that contribute to optical absorption can be identified by looking at the flat and dispersionless bands in the band structure plot. Bandgap of the material can also be calculated by taking the least difference between two states (valence and conduction) at the high symmetry points in the Brillouin zone. The standard path for each type of lattice is taken as defined by

Bradley et al., [113]. In this study, the band structure for sodium aluminum hydride is plotted, and dispersion in bands as well as its bandgap is evaluated from the results.

Density of states provides a qualitative picture of the width of conduction and valence bands, band gap, and the electronic structure of the material with contributions of each atomic species to the total density in a particular band. Density of states in a particular band ($N_n(E)$) is calculated by integrating the difference between the energy and the dispersion of the given band over the predefined k-points in the Brillouin zone.

$$N_n(E) = \frac{1}{4\pi^3} \int \delta(E - E_n(k)\, dk \qquad \text{(Eq. 2.11)}$$

The sum of the density of states (Eq. (2.11)), $N(E)$, is calculated as a summation over all bands, and the total electrons in the cell is given by integrating from negative infinity to the Fermi level. CASTEP uses linear interpolation of band energies [114] between the reference points formed by the k-point mesh generated using Monkhorst-Pack scheme [96]. DOS plots in this study show the contributions from $s$, $p$ or $d$ orbitals of different atoms that result in the peaks observed in conduction and valence bands at different energy levels. Peaks in total DOS (TDOS) plots show the sum of all the contributions from participating atomic species, and peaks in partial DOS plots (PDOS) showing individual contributions to the sum. DOS plots are also used in observing the change in electronic structure in case of impurities present in the crystals compared to the pure crystals.

## 2.2.5 Phonons

Phonons or quanta of lattice vibrations are calculated to understand the lattice dynamics in terms of infrared, Raman, and neutron scattering spectra as well as thermal properties of solids. Vibrations in crystals result from displacements of atoms from their

equilibrium positions. Since all the atoms in a lattice are coordinated, displacements in one atomic plane results in displacement of all corresponding planes in that lattice [92, 93]. Since the potential well encountered by each atom in a typical lattice is very steep, the displacements about their equilibrium positions are usually very small compared to the interatomic distance in the lattice. The potential energy of the system, ( $U(u_1, u_2, ..., u_N)$ ), can thus be written as a function of displacements ($u$) of the atoms from their equilibrium positions and expanded using Taylor's series about the point at which the displacement is equal to zero. This expansion results in the energy due to displacements as a quadratic function of relative displacement of any two points in a lattice and is written as [80]:

$$U(u_1, u_2, ..., u_N) = U(0, 0, ..., 0) + \frac{1}{2} \sum_{i,j}^{N} (\frac{\partial^2 U}{\partial u_i \partial u_j}) |_{u=0} u_i u_j + ... ,$$ 
(Eq. 2.12)

where $\dfrac{\partial^2 U}{\partial u_i \partial u_j}$ is a set of force constants. Cubic and higher order terms are neglected due to small atomic displacements with respect to their mean positions. Phonons can be determined once the force constant matrix $F(R - R')$, ($R$ and $R'$ are the initial and displaced positions of atoms in the lattice), is determined. In reciprocal space, the force constant matrix is called dynamical matrix (Eq. (2.13)) and is written as a function of wave vectors.

$$D_{i,j}(q) = \frac{1}{N_R} \sum_{R} F_{i,j}(R) \exp(-iqR)$$ 
(Eq. 2.13)

Each atomic displacement, $u(R,t) = \varepsilon \exp(i(qr - \omega(q))t)$ is now written as a form of a plane wave, where $\varepsilon$ is the eigenvector of the 3N dimensional problem: $M\omega(q)^2 \varepsilon = D(q)\varepsilon$. The dependence of frequency on wave vector is called phonon

dispersion [115]. Phonon vibrations are classified into acoustic and optical modes. Every lattice has three acoustic modes (two transverse and one longitudinal) and 3N-3 optical modes. Acoustic modes are zero at $\Gamma$ point, and optical modes have finite value. Acoustic modes are long wavelength modes and describe the dynamics of movement of different cells in phase. Optical modes describe the dynamics of movement in a particular cell and form as bands of frequencies when coupled with optical modes from different cells.

Phonon density of states is computed in a similar fashion as electronic density of states. Partial phonon DOS is the contribution of each atom to the total phonon DOS. Contribution to the DOS on each atom $i$, from each phonon band ($N_i(E)$) is given by integrating the difference between the energy and the energy mode $j$ multiplied with the square of eigenvalue ($\varepsilon_j(i)$) associated with a particular mode $j$.

$$N_i(E) = \frac{1}{4\pi^3} \int |\varepsilon_j(i)|^2 \delta(E - E_j(k)) dk \qquad \text{(Eq. 2.14)}$$

The projected density of states (Eq. (2.14)) is then obtained by summation of these contributions over all phonon bands. By construction all the projected phonon DOS sum up to the true phonon DOS.

Two popular approaches are used in modern day computations to compute phonon dispersion relations and phonon density of states: supercell or direct force constant [116, 117] and linear response or density functional perturbation theory (DFPT) [115]. In supercell approach, atoms are displaced by a small amount and reaction forces are calculated. This calculation requires a supercell to take into account the long range interactions in some crystals, especially polar and ionic crystals. In polar crystals the long range ionic interactions decay as a factor of $r^{-5}$ or less. Hence the dimension of the cell needs to be artificially increased. In practice cell dimensions greater than or equal to 10 Å

x 10 Å x 10 Å are chosen. A cutoff radius is also chosen that needs to be less than or equal to half the cell dimension beyond which the force constants are assumed to be zero. This assumption may lead to errors that are negligible in some cases but are more pronounced when optical properties are of interest. This method is memory intensive due to the increased number of k-points in the cell under investigation and the size of the force constant matrix. On the other hand, this method is easier to implement as it can be attached to the available electronic structure program through which reaction forces can be calculated.

Linear response method calculates the second order derivatives to the total energy in response to a perturbation. The force constants matrix can be obtained by differentiating the Hellmann-Feynman forces on atoms, with respect to ionic coordinates. This procedure reveals that the force constants matrix depends on the ground state electron charge density and on its linear response to a distortion of atomic positions [115]. CASTEP implements a variational DFPT scheme suggested by Gonze et al., [118] DFPT minimizes the second order perturbation in energy which results in first order changes in density, wavefunctions, and potential. The dynamical matrix at a particular wave vector is then calculated from minimized first order wavefunctions and densities. In CASTEP, a set of dynamical matrices obtained from calculations in real space is used to construct the dynamical matrix using the Fourier interpolation scheme. Advantages with this method include accurate representation of optical modes in both metals and non-metals, and no artificial increase in size of the unit cells. Options for runtime optimization in CASTEP include a choice of k-point grids and interpolation. In practice, calculations

are performed on a coarse k-point grid and are further interpolated onto a finer k-point grid. This practice is helpful in reducing the computational cost.

### 2.2.6 Thermodynamic Properties

Results from phonon density of states can be used to calculate thermodynamic functions such as enthalpy, free energy, entropy, and heat capacity as functions of temperature [92, 93]. Temperature dependent enthalpy is given by adding the total energy obtained from the electronic structure program to the sum of zero point energy and enthalpic contributions. Zero point energy is given by:

$$E_{ZP} = \int \frac{1}{2} F(\omega) \hbar \omega \, d\omega \,, \qquad \text{(Eq. 2.15)}$$

where $F(\omega)$ is the phonon density of states. Enthalpy is given by:

$$H(T) = E_{elec} + E_{ZP} + \int \frac{\hbar \omega}{\exp(\frac{\hbar \omega}{kT}) - 1} F(\omega) \, d\omega \qquad \text{(Eq. 2.16)}$$

Helmholtz free energy as a function of temperature is given by:

$$F(T) = E_{elec} + E_{ZP} + kT \int F(\omega) \ln \left[ 1 - \exp(-\frac{\hbar \omega}{kT}) \right] d\omega \qquad \text{(Eq. 2.17)}$$

Entropy is given by: $S(T) = k \left[ H(T) - \frac{F(T)}{T} \right]$, and the lattice contribution to heat capacity is given by:

$$C_v = k \int \frac{\left( \frac{\hbar \omega}{kT} \right)^2 \left( \exp\left( \frac{\hbar \omega}{kT} \right) \right)}{\left( \exp\left( \frac{\hbar \omega}{kT} \right) - 1 \right)^2} F(\omega) \, d\omega \qquad \text{(Eq. 2.18)}$$

### 2.2.7 Basis Functions and Pseudopotentials in DMoL$^3$

Electronic structure and energetics of molecules, solids and surfaces can be modeled and analyzed using DMoL$^3$ module in Materials Studio. Point group symmetry is implemented, but space group symmetry is not recognized by DMoL$^3$; therefore, only models with P1 symmetry can be studied. In this study, DMoL3 and DSolid are used for optimization runs of initial, final, and transition states of two layered surface slabs (explained in Chapters 3 and 4) of $NaAlH_4$ to study the kinetics of hydrogen desorption in sodium alanates. Basis sets and pseudopotentials used in DMoL$^3$ are discussed in this section.

Numerical basis sets are implemented in DMoL$^3$. The basis functions are given numerically as values on an atomic-centered spherical-polar mesh, rather than as analytical functions (i.e., Gaussian or Slater orbitals). The angular portion of each function is the appropriate spherical harmonic, and the radial portion is obtained by solving the atomic DFT equations numerically and are piece-wise analytic. Cutoff distance from the nucleus is specified and checked for accuracy. It uses a confinement potential that ensures strict localization and no singularities at the cutoff radius. Advantages of numerical basis sets over analytical basis sets include faster convergence, computational speed, and minimal basis set superposition error [119]. These basis sets can be increased in size to accommodate more degrees of freedom. The minimal basis set is called 'MIN' and when a second set of basis functions are added, it is called 'DN' (Double Numerical). Polarization functions also can be added. When $d$ functions are added, it is called DND (Double Numerical with $d$ polarization), and when both $d$

functions on heavier atoms than hydrogen and $p$ functions on hydrogen are added, it is called 'DNP'. In all the calculations in this study using DMoL$^3$, DNP basis set is used.

Three types of pseudopotentials are implemented: DSPP (DFT semi-core pseudopotentials), ECP (Effective core potentials) [120] and scalar relativity. DSPPs are generated using all electron relativistic DFT results, and ECPs are generated by replacing the core potential by some value. In scalar relativity pseudopotentials, core electrons are not replaced but pseudopotentials supplement the core electron with relativistic effects. All-electron relativistic potentials are used in this study.

# CHAPTER 3

# SODIUM ALUMINUM HYDRIDE (NaAlH₄)

Sodium Aluminum Hydride ($NaAlH_4$) falls under complex metal hydrides with hydrogens bonded to aluminum and ionically bound sodium ions to $AlH_4$ complexes. This Chapter presents results from first principles calculations determining the ground state structure; electronic properties such as electronic density of states, band structure, and charge population analysis on the atomic/ionic species; vibrational properties and thermodynamic properties of $NaAlH_4$.

## 3.1 Ground State Structure Calculations

A sodium alanate unit cell is built according to its tetragonal structure, which belongs to the I4₁/a space group (#88) with sodium, aluminum, and hydrogen atoms occupying the 4(a), 4(b) and 16( f) Wyckoff positions, respectively, with $x_H = 0.2662$, $y_H = 0.6084$ and $z_H = 0.0442$ based on the reference data from ICSD database [22, 121, 122]. It is optimized to obtain a ground state structure using GGA exchange and PW91 correlation with plane-wave basis set using both norm-conserving and ultrasoft pseudopotentials as implemented in CASTEP. Convergence criteria for energy, force, stress, and displacement are set at $1 \times 10^{-6}$ eV atom$^{-1}$, $1 \times 10^{-3}$ eV/Å, $1 \times 10^{-2}$ GPa and $1 \times 10^{-3}$ Å, respectively. Fixed basis set quality is used in all the calculations. Different k-point mesh configurations with k-point separation values of 0.05 Å$^{-1}$ to 0.02 Å$^{-1}$ are

checked for convergence. Various energy cutoff values in the range of 800-900 eV in case of norm-conserving pseudopotentials and 400-500 eV in case of ultrasoft pseudopotentials are used to obtain the optimally converged structure among all configurations modeled. Variation in total energy per formula unit values with respect to the k-point mesh as well as energy cutoff values is plotted in the Figure 3.1. Calculated total energy values at each specified cutoff and k-point spacing are plotted relative to the total energy calculated with 500 eV cutoff and 0.02 $\text{Å}^{-1}$ k-point mesh spacing in case of ultrasoft pseudopotentials (Figure 3.1(a)), and 900 eV cutoff and 0.02 $\text{Å}^{-1}$ k-point mesh spacing in case of norm-conserving pseudopotentials (Figure 3.1(b)).
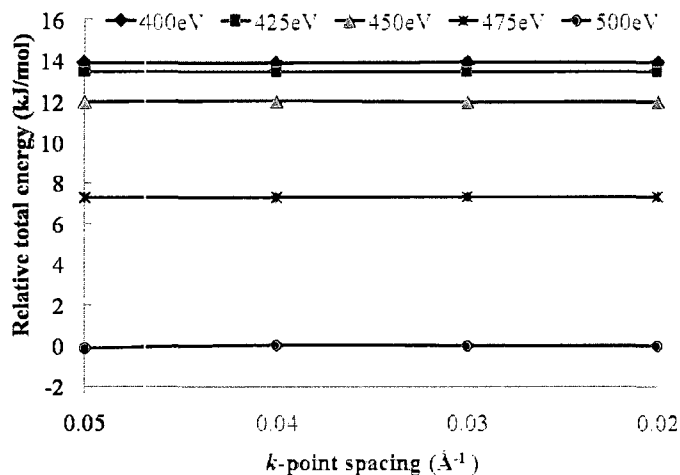
**(a)**
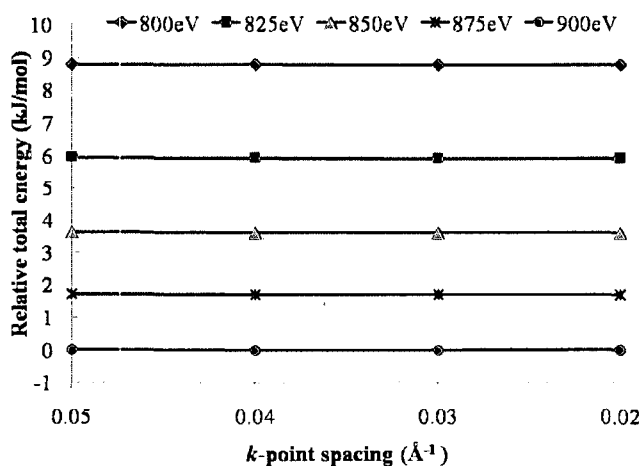


**(b)**

Figure 3.1 Variations in total energy at specified cutoff values as function of k-point mesh spacing using (a) ultrasoft and (b) norm-conserving pseudopotentials.

From the Figure 3.1(a), we can see that the variations in converged total energy values are insignificant with respect to changes in k-point mesh spacing; however, total energy decreased with increase in specified kinetic energy cutoff values. Difference in total energies, with 400 eV and 500 eV kinetic energy cutoff and ultrasoft pseudopotentials is in the order of 16 kJ/mol, and is in the order of 9 kJ/mol in case of norm-conserving pseudopotentials with 800 and 900 eV kinetic energy cutoff values.

Sodium alanate unit cell optimized using ultrasoft pseudopotentials, 500 eV kinetic energy cutoff and 0.02 $Å^{-1}$ k-point mesh spacing is analyzed in subsequent sections to investigate the geometric details, electronic properties and electron density maps. To determine vibrational properties of sodium alanate, linear response method is used which is implemented only in conjunction with norm-conserving pseudopotentials in CASTEP. Hence for determining vibrational properties and free energy of sodium alanate, optimized conformation using norm-conserving pseudopotentials, 900 eV kinetic energy cutoff, and 0.02 $Å^{-1}$ k-point mesh spacing is used. Figure 3.2 shows the optimized conformations of primitive and conventional cells of $NaAlH_4$. Primitive cell has two and conventional cell has four formula units of $NaAlH_4$. $NaAlH_4$ crystal structure comprises $AlH_4$ tetrahedral units and Na ions with Na and Al occupying *4a* and *4b* sites and H in *16f* sites of the tetragonal unit cell.



**(a)**          **(b)**
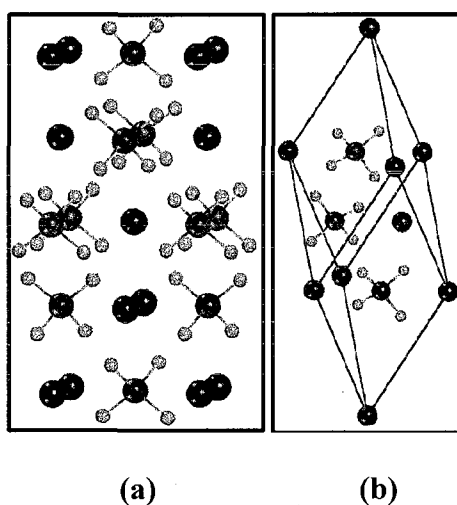
Figure 3.2 Optimized configurations of sodium alanate (a) conventional cell and (b) primitive cell.

Optimized lattice parameters, tabulated in Table 3.1, agree well with the reported experimental information [22, 122]. Calculated bondlengths between Al-H atoms in $AlH_4$

complexes (1.638 Å) and Na ions and AlH$_4$ complexes (3.535 Å), compare well with the reported bond lengths of 1.63 Å and 3.52 Å [22]. AlH$_4$ tetrahedra are slightly distorted with two sets of H-Al-H angles of 107.5° and 113.4°. Unsigned error in calculated bondlengths compared to experimental values is in the range of 0.002-0.007 Å, which is in the typical error range of 0.5-0.1% observed in bondlengths [123] and error less than 0.5% in lattice parameters [124] using plane wave methods.

Table 3.1 Optimized structural parameters of NaAlH$_4$.

| Lattice parameters | Calculated | [22] |
|---|---|---|
| I4 1/a (Tetragonal) #88 | a=b=4.99, c=11.08 $\alpha=\beta=\gamma=90$ | a=b=4.99, c=11.07 $\alpha=\beta=\gamma=90$ |
| Bondlengths(Å) | Calculated | Expt. [22] |
| Al-H | 1.638 | 1.631 |
| Na-Al | 3.532 | 3.528 |
| Na-H | 2.399 | 2.401 |
| Angles(°) | Calculated | Expt. [22] |
| H-Al-H | 107.5° 113.4° | 107.5° 113.5° |

## 3.2 Electronic Properties

Electronic configuration of NaAlH$_4$ is presented from the calculations of total and partial electronic density of states, band structure in NaAlH$_4$, charge and bond population analysis using Mülliken charge distribution on ionic/molecular species, and charge analysis using born effective charge tensors.

### 3.2.1 Band Structure and Density of States

Band structures provide useful information related to dependence of electronic energies with respect to k-vector along the high symmetry directions in the Brillouin zone. Interesting properties such as optical absorption, dispersion along high symmetry directions in the Brillouin zone, and bandgap of the materials can be calculated from

band structure plots. In this study band structure plot is used to identify the bandgap in $NaAlH_4$. Figure 3.3 shows the bands observed along the high symmetry k-vectors in brillouin zone Z (0.5, 0.5, -0.5), Γ (0.0, 0.0, 0.0), X (0.0, 0.0, 0.5), P (0.25, 0.25, 0.25) and N (0.0, 0.5, 0.0) in the range of -8 to 8 eV. Curves in red represent the bands in valence band region, and curves in black represent the bands observed in conduction band. Fermi level is shown as a dotted blue line at zero energy. Based on the difference between the electronic energies of valence bands and conduction bands at Γ point (as shown in Figure 3.3), the bandgap in $NaAlH_4$ is estimated to be equal to 4.8 eV, and that matches exactly with the reported bandgap of $NaAlH_4$ [22].
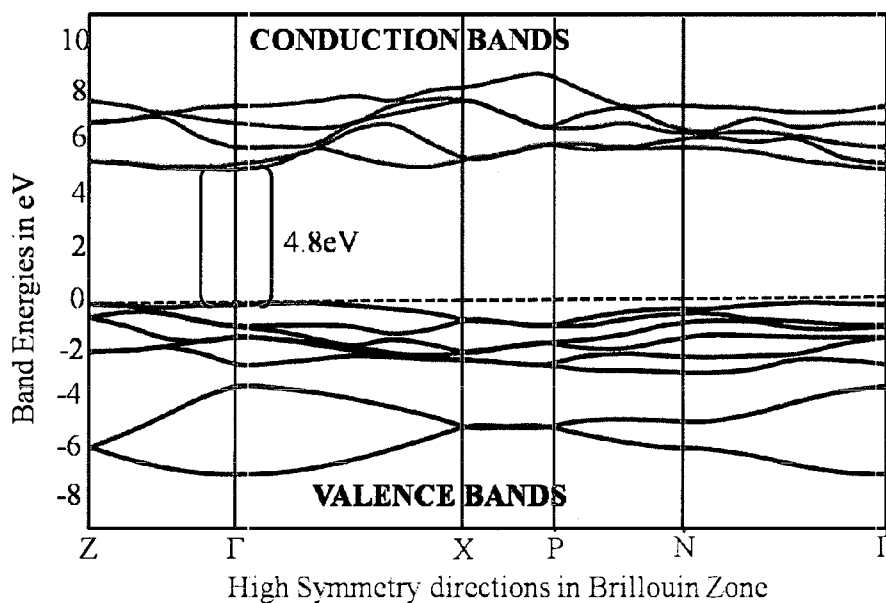
Figure 3.3 Electronic band structure of $NaAlH_4$. Dispersion along the high symmetric directions in the Brillouin zone is shown. Lines in red indicate dispersion of valence bands, and lines in black indicate dispersion of conduction bands.

Besides band structure, total and partial density of states are plotted to obtain information regarding bond structure in sodium aluminum hydrides. Analysis of DOS (explained in Chapter 2, Section 2.2.4.3) is done by Gaussian smearing (0.02 eV) of the

energy levels of each band followed by the histogram sampling. This sampling reproduces the general shape of DOS without Van Hove singularities. The plots in Figure 3.4 show the density of states (total DOS) in sodium alanate as well as partial DOS of each atomic species present in sodium alanate (Na, Al and H). Interpolating total and partial DOS plots of $NaAlH_4$, we can see that the valence band is occupied with $s$ and $p$ states of aluminum and hydrogen, and the conduction band is occupied with $s$ and $p$ states of sodium and aluminum. Main contributions to the peaks observed below the Fermi level (0 to -3 eV) are from $s$ orbitals of hydrogen and $p$ orbital of aluminum, and the peaks below -3 eV (-3 to -6 eV) arise from contributions of $s$ orbital of hydrogen and $s$ orbital of aluminum. The DOS in the valence band indicate the covalent bond structure due to hybridized $sp$ orbitals from $s$ of hydrogen and $p$ of aluminum with energies in the range of 0 to -3 eV. No contribution from outer $s$ orbitals of Na is seen in the valence band indicating the non-covalent interactions between Na and $AlH_4$ groups. The $s$ orbitals of sodium are well buried below the Fermi level that is not seen from the plot, and the $p$ orbitals of sodium are present in the conduction band. Both the bands are separated by a bandgap nearly equal to 4.8 eV indicating the insulating behavior of sodium alanate, which is consistent with the observation from the band structure plot. Further analysis of bond structure observed between Al and H is explored using electron density maps and bond population analysis in subsequent sections.
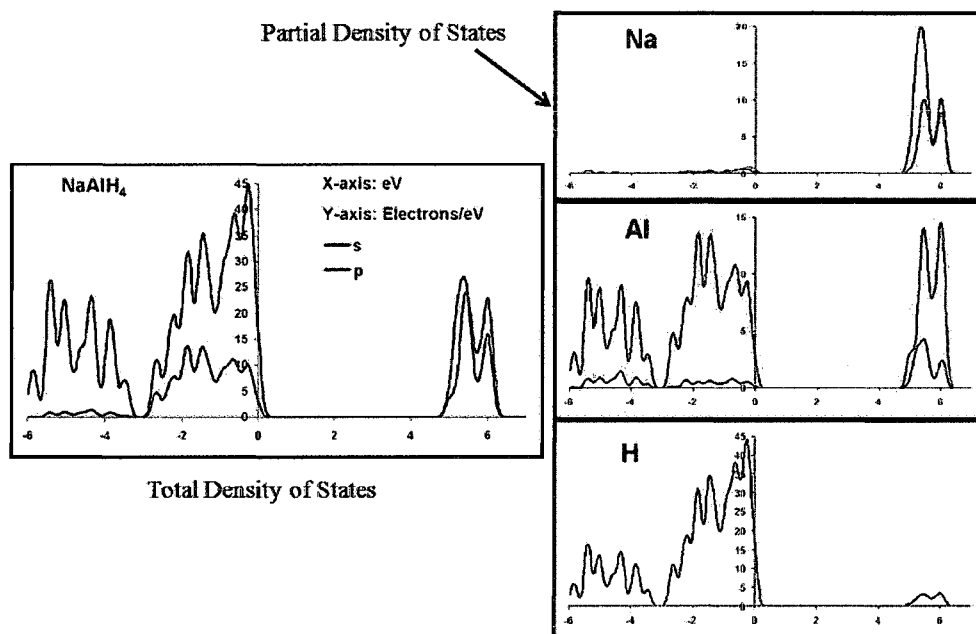
Figure 3.4 Partial and total density of states (PDOS and TDOS) in NaAlH₄. Lines in blue indicate the contributions from *s* orbital, and lines in pink indicate contributions from *p* orbitals.

### 3.2.2 Electron Density Maps

Electron density maps are constructed by mapping the total electron density calculated from our DFT calculations onto the atoms. Mapped electron density is plotted on a color scale of 32 values with zero (red) representing minimum value, 32 representing (blue) mean value, and the numbers between zero and 32 (color gradient from red to blue in a rainbow) representing the gradient in the observed electron density.
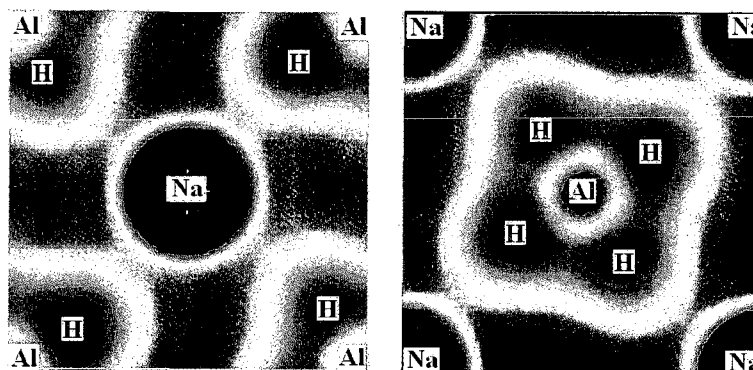
Figure 3.5 Electron density maps with electron density mapped over the atoms in NaAlH$_4$. Minimum electron density regions are shaded in red, and mean to maximum values are shaded in blue. The color gradient from blue to red indicates the electron density values normalized over the values from blue to red.

From the maps in Figure 3.5, a smeared electron density cloud is seen in the AlH$_4$ group between Al and H atoms. This cloud indicates electron sharing between Al and H atoms with a possibility of existence of covalent bonds between Al and H atoms in AlH$_4$ group and is consistent with our observations form density of states calculations. Blue colored areas around hydrogen atoms in AlH$_4$ groups indicate higher electron density values that are possible due to the higher electronegativity values for hydrogen than aluminum. Minimum or no electron density is seen between Na ions and AlH$_4$ groups indicating no bond formed by sharing electrons between two groups. Blue areas around Na ions are due to the filled electrons in $2p$ orbital of sodium, which are taken into account as valence electrons by the pseudopotential used. From the electron density maps of NaAlH$_4$, it can be deduced that covalent bonding exists between Al and H atoms in AlH$_4$ groups and Na ions are electrostatically bound (ionic bonding) to AlH$_4$ groups, and stabilize the lattice.

### 3.2.3 Mülliken Bond Population Analysis

Bond population analysis schemes implemented in CASTEP are used to determine the strength of the bonds in the observed multi atomic complexes. Bond population is based on projection of plane wave states onto the generated pseudo-atomic orbitals [109] and Mülliken population analysis [110]. Its values, on a scale from -1 to 1, represent a bonding state when the overlap population values are positive and an anti-bonding state when the values are negative. Values with zero overlap indicate no significant interaction between two atoms [111]. Results presented in this study show no anti-bonding states. Hence, all the presented overlap population values are on a scale from zero (no bond) to one (strong bond). Besides bonding states, covalence of the bond can also be determined since it is proportional to the overlap population. Hence, the closer the bond population to one, the more covalent the bond between the atoms [112]. Relative overlap population between two atoms in different compounds would indicate the degree of covalence of the same bond in different situations. Furthermore, ionicity of the bond can be indicated from the effective Mülliken charges on the participating atoms [112]. Calculated atomic populations in Na, Al and H and bond population in Al-H and Na-H bonds are listed in Table 3.2.

Table 3.2 Mülliken bond population analysis and Mülliken atomic population and charge on Na, Al and H species in NaAlH$_4$.

| Atomic/Ionic Species | Mülliken Atomic Population | | | |
|---|---|---|---|---|
| | s | p | Total | Charge (e) |
| H | 1.46 | 0 | 1.46 | -0.46 |
| Al | 0.92 | 1.56 | 2.48 | 0.52 |
| Na | 2.03 | 5.64 | 7.67 | 1.33 |
| Bond Population Analysis | | | | |
| Bond | Bond Population | | Bond Length (Å) | |
| Al-H | 0.85 | | 1.638 | |
| Na-H | < 0 | | 2.403 | |

Analyzing the bond population in AlH$_4$ groups, high bond population of 0.85 is found between Al-H bonds, giving indication that the bonding in the AlH$_4$ tetrahedral complexes is indeed covalent. Bond population value between Na and H is less than zero indicating the bond is non-covalent. Moreover, the effective charge on Na (+1.33e) and therefore the sum of effective charges in AlH$_4$ group (-1.32e) shows the existence of ionic bonds between Na atoms and AlH$_4$ groups in the NaAlH$_4$ unit cell.

### 3.2.4 Born Effective Charges

We present here analysis of charges on Na, Al, and H based on born effective charge method. Calculated born effective charge tensors of Na, Al, and H are tabulated in Table 3.3.

Table 3.3 Calculated born effective charge tensors on Na, Al, and H atoms in NaAlH$_4$.

| Atomic/Ionic Species | $Z_{xx}$ | $Z_{yy}$ | $Z_{zz}$ | $Z_{xy}$ | $Z_{xz}$ | $Z_{yx}$ | $Z_{yz}$ | $Z_{zx}$ | $Z_{zy}$ |
|---|---|---|---|---|---|---|---|---|---|
| Na | 1.23 | 1.23 | 1.13 | -0.02 | 0 | 0.02 | 0 | 0 | 0 |
| Al | 1.55 | 1.55 | 1.85 | 0 | 0 | 0 | 0 | 0 | 0 |
| H | -0.75 | -0.64 | -0.75 | 0.09 | 0.13 | 0.09 | -0.08 | 0.11 | -0.11 |

Charge tensors of Na and Al are diagonal, and H is off-diagonal indicating low symmetry with respect to Na and Al. Charges on Na (1.13 to 1.23 e) and H (-0.64 to -0.75 e) are close to their nominal charges (+1 and -1 e, respectively) whereas charge on Al is lower than its nominal ionic charge of +3. Charge distribution thus obtained from born effective charge tensors also show an existence of ionic interactions between Na ions and H ions in $AlH_4$ groups with charge concentrated around H ions in $AlH_4$ groups. These charges also have prominence in determining LO/TO splitting calculations near the Gamma point in case of phonon dispersion modes in lattice that are later explained in Vibrational Properties section of this Chapter.

### 3.3 Vibrational Properties

Phonon dispersion relations and phonon density of states are calculated to obtain the vibrational spectrum of $NaAlH_4$ (Figure 3.6). Linear response method as implemented in CASTEP (explained in Chapter 2, Section 2.2.5) is used to calculate the phonons in $NaAlH_4$.
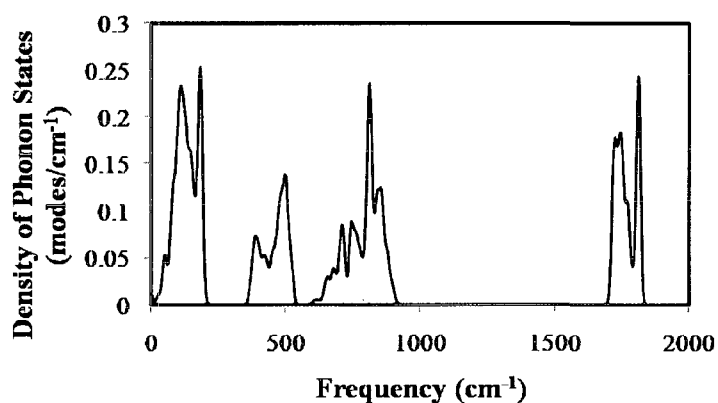


Figure 3.6 Phonon DOS spectrum of $NaAlH_4$.

No imaginary modes in the phonon spectrum indicate a stable ground state structure. Obtained phonon DOS spectrum is divided into three regions: high frequency region (1700-1900 $cm^{-1}$), medium-to-low frequency region (300-900 $cm^{-1}$), and low frequency region (< 300 $cm^{-1}$). Modes in the high frequency region correspond to stretching of bonds in covalently bound complexes in the materials, and frequencies in medium-to-low region correspond to the both rotational and vibrational modes (librational) in the crystal. Low frequencies in the spectrum correspond to the translational motion of atomic/ionic species in the crystal. From the analysis of vibrational frequencies in the calculated structures of $NaAlH_4$, normal modes in IR spectrum corresponding to Al-H symmetric stretching in the $AlH_4$ tetrahedra are found to be $1808cm^{-1}$ and asymmetric stretching modes at 1737 and $1704cm^{-1}$. These modes agree well with the experimental reported vibrations of $1850cm^{-1}$ for Al-H symmetric stretch and $1670cm^{-1}$ peak assigned to asymmetric stretch [125]. Three peaks related to IR active modes at 867, 835 and $705cm^{-1}$ that correspond to Al-H bending region at $\Gamma$ point along the three high symmetry directions Z (0.5, 0.5 -0.5), X (0.0, 0.0, 0.5) and N (0.0, 0.5, 0.0) and one IR active mode at $750cm^{-1}$ along X and $601cm^{-1}$ along N are found in the phonon DOS spectrum. Peaks observed in the experimentally reported IR spectrum by Gomes et al. in Al-H bending region at $\Gamma$ point are located at 900, 800, 735 and 695 $cm^{-1}$.

### 3.4 Thermodynamic Functions

Thermodynamic functions such as enthalpy, entropy, and free energy are plotted as a function of temperature (Figure 3.7(a)-(c)). In Figure 3.7, H(0), S(0) indicate enthalpy and entropy values at 0 K and H(T), S(T) and G(T) indicate the calculated enthalpy, entropy and free energy values at a particular temperature (T). Zero point

energy, enthalpic and entropic corrections as a function of temperature is obtained from phonon DOS calculations as explained in Chapter 2. Total enthalpy at a particular temperature is calculated by adding the electronic energy to the sum of zero point energy and enthalpic contributions at that temperature. Gibbs free energy is obtained by the difference between total enthalpy and the product of entropy and temperature. Contributions from change in volume are neglected as the total changes in volume with respect to temperature are negligible in solids.
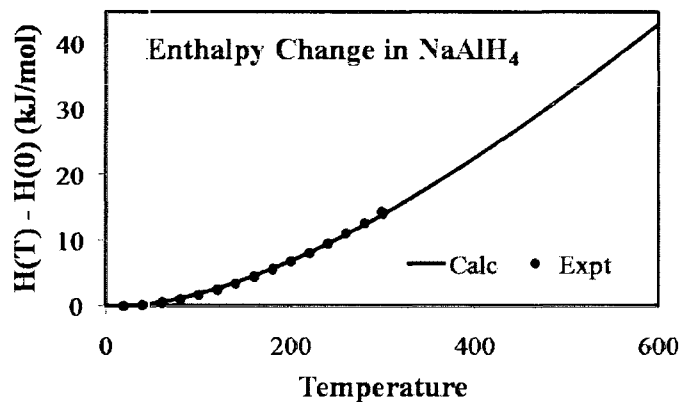
(a)
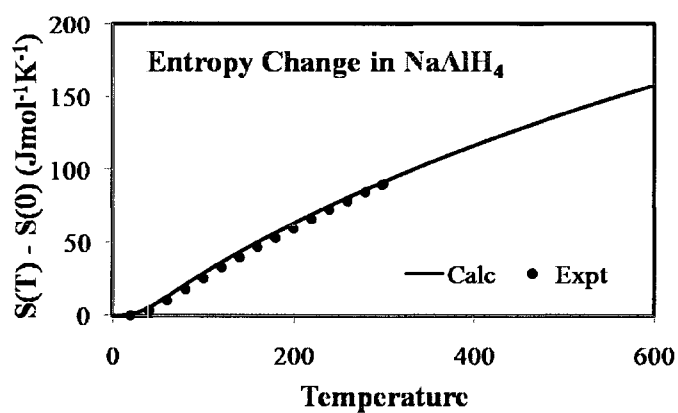


(b)
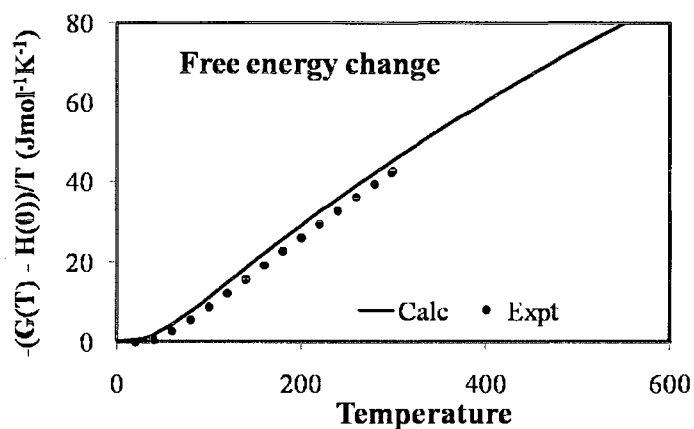


(c)

Figure 3.7 Thermodynamic functions plotted as a function of temperature. Reference values are obtained from Bonnetot et al. [126].

Experimental reported values for the thermodynamic functions are available for the temperature range of 0-300 K. In the temperature range of 0-300 K, calculated values agree well with the experimental values validating our calculations. However, beyond 450 K the curves may be unreliable as the melting point for $NaAlH_4$ is noted as 453 K and harmonic approximation of phonons is no longer valid. Based on the excellent agreement with experimental values, similar methods are extended to other ionic crystals such as $Na_3AlH_6$ and NaH. Free energy per formula unit of $NaAlH_4$ is obtained by dividing the total free energy by the number of formula units of $NaAlH_4$ in the conventional/primitive cell.

## 3.5 Extended Lattice Models and Surfaces

Until now the calculations are carried out on a conventional or primitive cell to understand the structural, electronic, and vibrational properties of $NaAlH_4$. Since space group symmetry is followed in CASTEP, ions and their symmetric images are affected by any changes that are induced at particular lattice sites. To study the effects of vacancies or impurities or dopants that replace the atoms or ions in lattice sites, extended lattice structures must be modeled to avoid the interactions between that particular lattice site and its periodic images. In this study, effects of titanium dopants that replace the Na lattice sites, and sodium alanate supercell with some vacant lattice sites that may be introduced due to Ti dopants, are modeled. Hence to model these structures, an optimized sodium alanate conventional cell is extended in two lattice directions *a* and *b* to build a 2x2x1 supercell with dimensions nearly equal to 10 Å x 10 Å x 11 Å (Figure 3.8). Figure 3.8 presents the modeled extended lattice structure of $NaAlH_4$. Constructed models provide few lattice sites that are independent of symmetric images inside the supercell,

and the images in adjacent supercells are separated by a distance nearly equal to 10 Å. This distance satisfies the requirement of enough separation distance for the forces to converge near to zero and a well defined force constant matrix with cutoff distance specified at 5 Å as explained in Chapter 2. Results of the simulations on effects of Ti dopants introduced in bulk of $NaAlH_4$ are presented in Chapter 5.
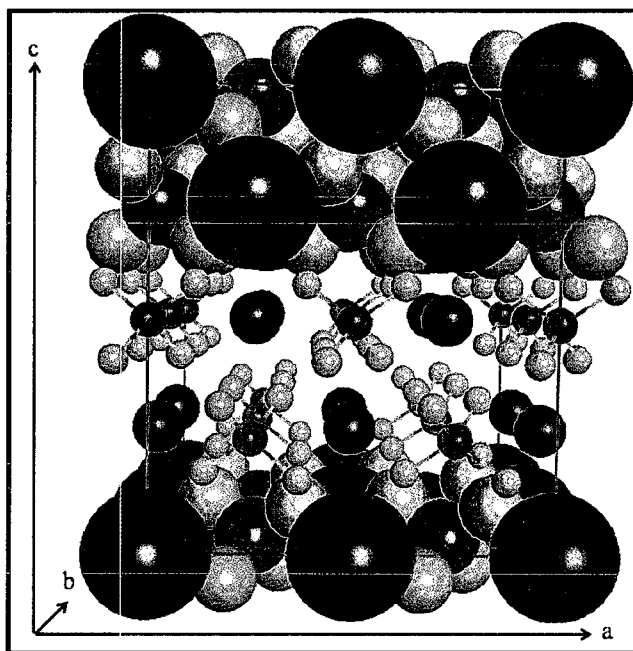


Figure 3.8 2x2x1 supercell of $NaAlH_4$ with 16 formula units.

To study the effects of Ti dopants that reside on the surface and play a role in chemical reactions occurring at the surface, structures revealing (001) termination of $NaAlH_4$ lattice are modeled. Surface energy of (001) surface termination is less when compared to the other terminations such as (011) or (100) [27]. Hence, all the surfaces that are modeled in this study expose (001) termination of $NaAlH_4$. Surfaces are constructed by selecting the appropriate bulk model and cleaving it along (001) direction. Once the surfaces are cleaved, it is enclosed in a 3D box to run further calculations.

Thickness of the slab is controlled by the cleave depth and width is controlled by the size of the supercell. Depending on the number of layers that interact with dopants and that take place in the surface interactions, depth of the slab is chosen. Width of the slab is chosen in such a way that the dopants that reside above the surface should interact only with the atoms in that particular cell and any interactions between dopants in adjacent cells must be avoided. Besides width and thickness of the constructed slab, vacuum space that is left above the surface is also an important factor to avoid interactions between the periodic images of atoms in the slabs in adjacent cells.

In this study, three types of surfaces are modeled: a first with two layers thick and a vacuum space of 5 Å (Figure 3.9(a)), a second with two layers thick and 15 Å vacuum space above the surface, and a third with four layers thick and 15 Å vacuum space above the surface (Figure 3.9(b)).
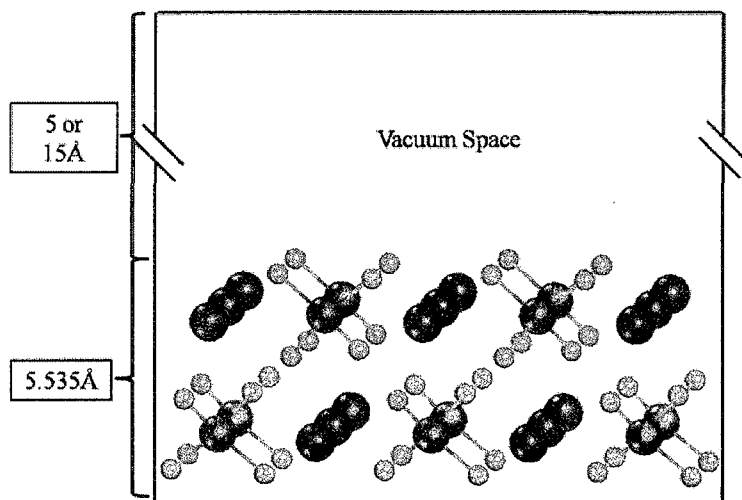
**(a)**
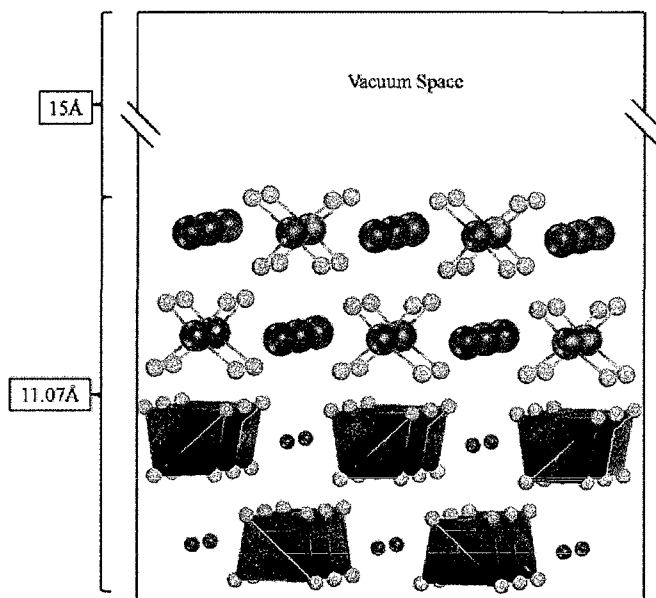


**(b)**

Figure 3.9 Modeled NaAlH$_4$ slabs exposing (001) surface termination with (a) two layers thick with 5 and 15 Å vacuum space and (b) four layers thick with 15 Å vacuum space above the surface.

First surface model with two layers of sodium alanate formula units is used in calculations to explore the preferred sites for Ti dopants on NaAlH$_4$ surface explained in Chapter 5. These surfaces are also used to study the dynamics of formed Ti-Al-H

compounds at elevated temperatures. The second surface model is used in calculations to study the kinetics of hydrogen desorption in pristine sodium alanates. These studies require a local site with enough formula units to describe the possible reaction mechanism for hydrogen desorption and enough vacuum space above the surface to accommodate the desorbed species from the surface with no interactions with the periodic image in the adjacent cell above it. Results from kinetics calculations are reported in Chapter 4. The third surface is used in calculations to validate the calculations using the first surface model and to study the effect of Ti dopants in improved kinetics of hydrogen desorption in Ti-doped $NaAlH_4$ reported in Chapter 6. Optimization and dynamics calculations to study the formed Ti-Al-H compounds using both the surface models with two and four layers yielded similar results. However, the dynamics of hydrogen hopping and rearrangement of Na and Al species in the layers below the surface at elevated temperatures is not observed from two layer models that are further explained in calculations using four layer surface models.

### 3.6 Summary

Structural, electronic, vibrational properties and thermodynamic functions of sodium alanate are calculated and discussed in this Chapter. Optimized lattice parameters, bond lengths, and bond angles compare well with the reported experimental values providing ground state geometry for further calculations. Band structure, electron density maps, density of states, and charge population analysis using both Mülliken and Born effective charge tensors are calculated to provide insights into the electronic structure of sodium alanates. In sodium alanates structure, Na ions are bound electrostatically to the covalently bound $AlH_4$ groups with a band gap of 4.8 eV. Electron

density maps provide a pictorial description of electron density distribution and density of states results show the contributions from each atomic species. Overall the predicted properties from these calculations agree well with the reported information. Vibrational properties and derived thermodynamic observables that are predicted from our calculations are also presented. Extended lattice models and surfaces as built are also explained in Chapter 3 and are used for subsequent calculations.

# CHAPTER 4

# THERMODYNAMICS AND KINETICS OF
# HYDROGEN DESORPTION IN NaAlH₄

## 4.1 Thermodynamics of Hydrogen Desorption

Decomposition of sodium alanate proceeds through a two step reaction resulting

in $Na_3AlH_6$ and aluminum phases in the first step and NaH and aluminum phases in the

second step. Total hydrogen desorbed from the native material adds up to 5.6 wt%.

Decomposition reactions of pristine sodium alanates have been widely studied using

experiments and theoretical methods. They are repeated in this study to provide better

predictions, to validate our methodology, and to precede further investigations on

thermodynamics of Ti-doped sodium alanates.

### 4.1.1 Computational Details

Evaluation of vibrational properties thereby estimating the thermodynamic

properties at different temperatures using direct force constant approach is reported for

pure crystal structures of $NaAlH_4$ and $Na_3AlH_6$ as well as their corresponding

decomposition reactions [127]. Evaluating phonon DOS to calculate the zero point

energies, vibrational, translational, and rotational contributions to the total free energy is

one of the most computationally complex and expensive tasks. Direct force constant

approach (finite displacement/supercell method) calculates the reaction forces on atoms

by inducing small displacements from their mean positions. A force constant cutoff is

used in the calculations beyond which the forces on the atoms are assumed to be zero. Limitation in finite displacement/supercell method is to increase the size of the cell (memory intensive) to accommodate the decay of the potential to near zero. Limitations in this method often result in significant deviation in the observed properties such as temperature of hydrogen desorption. In case of Coulombic attractions between ionic species in crystals, the force constant matrix decays to zero, typically, in 8-10 Å. Specifying a smaller number as a force constant cut-off may introduce some wrap-around errors that may manifest as imaginary frequencies. Hence, this supercell approach requires the supercells with cell edges ranging in lengths from 16-20 Å, which in turn increases the memory requirements for the task to be computed. For metals, FCM decays to zero sooner than the insulators, which can be evaluated fairly easy using finite displacement/supercell methods. DFPT formalism has obvious advantages over the finite displacement/supercell approach in terms of size of the cell and the value of the force constant. Lattice dynamics using DFPT formalism is calculated by minimizing the second order perturbation in the total energy. Force constants matrix thus depends on the ground state electron charge density and on its linear response to a distortion of atomic positions, which is calculated by differentiating the Hellmann-Feynman forces on atoms, with respect to ionic coordinates. DFPT calculations are accurate but computationally expensive as well as complex to be implemented for metals. Hence DFPT is implemented only for insulators in CASTEP. Based on the above reasons and to provide more realistic predictions of observable properties at macro scale, in this study, thermodynamic relations explaining the two step decomposition of sodium alanate resulting in hydrogen desorption are studied using combination of both methods.

Calculation of vibrational properties of crystalline structures is performed using computing phonon density of states (DOS) through linear response method, finite displacement/supercell (direct force constant) method as implemented in CASTEP. In CASTEP, the linear response method is only implemented for insulators and with a restriction of using norm-conserving pseudopotentials. In our calculations, for calculation of phonons using the linear response method, compounds with band gaps greater than 1 eV are reoptimized using norm-conserving pseudopotentials with energy cutoff set at 900 eV. Electronic parameters for phonon calculations are consistent with the geometry optimization calculations. In linear response method phonon dispersion and phonon density of states are evaluated on a coarse/medium k-point grid and are interpolated onto a finer grid with k-point grid spacing of 0.04 $\text{Å}^{-1}$. In the case of metals (band gaps < 1 eV), USPP and finite displacement/supercell method with supercells sized greater than 10x10x10 Å are used, and phonon DOS are evaluated at $\Gamma$ point only. To be consistent in evaluation of enthalpies and free energies, electronic energy is taken from the geometry optimization calculations using norm-conserving pseudopotentials at 900 eV cutoff (for all compounds), and free energy contributions are taken from the appropriate calculated models. Vibrational properties are estimated by applying the appropriate technique (linear response or direct force constant/supercell). Linear response method is used for models with a band gap > 1 eV ($NaAlH_4$, $Na_3AlH_6$ and $NaH$), and finite displacement/supercell (direct force constant) method is applied for models that are metallic with no or band gaps less than 1 eV ($Al^0$) since linear response method is not implemented for metals in CASTEP.

To estimate the macroscopic thermodynamic observables of the above decomposition reactions such as enthalpy, Gibbs free energy, and desorption temperature, structures of the reactants and products are geometry optimized, and electronic and vibrational properties are calculated as explained in Chapter 2. Gibbs free energy of the reaction ($\Delta G_{REACTION}$) and enthalpy of the reaction ($\Delta H_{REACTION}$) are calculated by taking the difference between the sums of respective properties of products and reactants. Thermodynamic properties of each compound are calculated according to the equations listed below:

$$G(T) = H(T) - TS \qquad \text{(Eq. 4.1)}$$

$$H(T) = U(T) + PV \qquad \text{(Eq. 4.2)}$$

$$U(T) = U_0 + U_{ZPE} + U_{VIB} + U_{TRANS} + U_{ROT} \qquad \text{(Eq. 4.3)}$$

In Eqs. (4.1-4.3), $G$ is the free energy, $H(T)$ is the temperature dependent enthalpy, and S is the entropy. $U(T)$, the total internal energy, is obtained by adding the energies related to electronic, translational, rotational, and vibrational degrees of freedom. $PV$, is equal to the contribution to enthalpy from total volume changes. In case of solids, since change in volume is negligible, enthalpy is equal to the total internal energy. Electronic energies of solids are obtained from our electronic structure calculations, and zero point energy along with other contributions to obtain the enthalpy and entropy at different temperatures are obtained from the phonon density of states calculations. Electronic energy of hydrogen is obtained from plane wave calculations using norm-conserving pseudopotentials and the other contributions from statistical mechanics evaluations of hydrogen as ideal gas. In case of hydrogen, $P$ is equal to one

atm and $V$ is the molar volume of hydrogen. Desorption temperature or the reaction temperature is equal to the temperature at which $\Delta G_{REACTION}$ is equal to zero.

### 4.1.2 Structure and Thermodynamic Observables

Thermodynamic observables for each compound that participates in decomposition reaction of sodium alanate are obtained from evaluated phonon DOS calculations on the optimized structures using our DFT calculations. This section presents information related to evaluated functions of each compound, and their agreement with the experimental information. Extensive study on $NaAlH_4$ is presented in Chapter 3. Lattice parameters of unit cells of $NaAlH_4$, $Na_3AlH_6$, $NaH$ and $Al$ obtained from our geometry optimization calculations are in agreement with the reported experimental values (Table 4.1). Further study on $Na_3AlH_6$, $NaH$, and aluminum is presented in subsequent parts of this section.

Table 4.1 Calculated lattice parameters of $NaAlH_4$, $Na_3AlH_6$, $NaH$ and $Al$. Experimental values for $NaAlH_4$ and $Na_3AlH_6$ from [22] and Aluminum from [128] and NaH from [129].

| Unit cell | Ultrasoft pseudopotentials | Norm-conserving pseudopotentials | Expt [22, 128, 129] |
|---|---|---|---|
| $NaAlH_4$ | a=b=4.99, c=11.08 $\alpha=\beta=\gamma=90$ | a=b=4.99, c=11.35 $\alpha=\beta=\gamma=90$ | a=b=4.99, c=11.07 $\alpha=\beta=\gamma=90$ |
| $Na_3AlH_6$ | a=5.36,b=5.54, c=7.72 $\alpha=\gamma=90$, $\beta=89.90$ | a=5.37, b=5.56, c=7.75 $\alpha=\gamma=90$, $\beta=89.89$ | a=5.32, b=5.56, c=7.72 $\alpha=\gamma=90$, $\beta=89.72$ |
| $Al$ | a=b=c=4.05 $\alpha=\beta=\gamma=90$ | a=b=c=4.01 $\alpha=\beta=\gamma=90$ | a=b=c=4.06 $\alpha=\beta=\gamma=90$ |
| $NaH$ | a=b=c=4.87 $\alpha=\beta=\gamma=90$ | a=b=c=4.86 $\alpha=\beta=\gamma=90$ | a=b=c=4.89 $\alpha=\beta=\gamma=90$ |

## 4.1.2.1 Na₃AlH₆

The initial structure of Na₃AlH₆ is taken from the ICSD database [121] and is optimized using DFT formalism as implemented in CASTEP. Figure 4.1 shows the optimized structure of Na₃AlH₆ using norm-conserving pseudopotentials with 900 eV cutoff and a k-point spacing of 0.02 Å⁻¹. Na₃AlH₆ structure comprises three $Na^+$ ions electrostatically bound to $AlH_6^{3-}$ forming a monoclinic structure and Al occupying *2a*, one Na in *2b*, and two other Na ions and hydrogens at *4e* sites of the lattice. Calculated lattice parameters (Table 4.1) agree well with the experimental reported parameters.
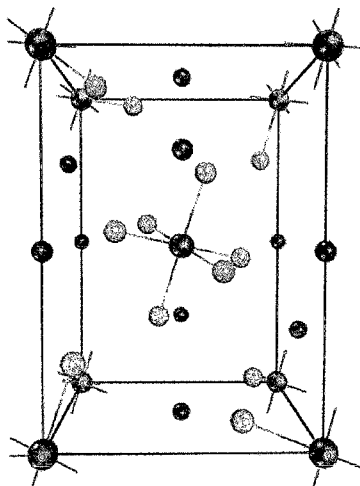


Figure 4.1 Orthographic view of optimized structure of Na₃AlH₆ showing only the atoms inside the conventional cell. Atom colors: Purple (Na), magenta (Al) and grey (H).

No imaginary modes are found in the calculated phonon DOS spectrum (Figure 4.2) and the maximum interpolation error that measures the accuracy of the dynamical matrix is in the order of 9 cm⁻¹. Multiple peaks are found in the high frequency region (>1200 cm⁻¹) that correspond to the Al-H bond stretching. One peak around 1405 cm⁻¹ corresponds to symmetric stretching of the Al-H bond, and the frequencies around 1280 cm⁻¹ and 1330 cm⁻¹ are doubly degenerate and correspond to the asymmetric

stretching of Al-H bonds in the $AlH_6^{3-}$ covalent anion complex in $Na_3AlH_6$. The peak shown in the phonon DOS plot that is greater than 1500 $cm^{-1}$ is a Raman active and infrared inactive mode. Other peaks that are in range of 650 $cm^{-1}$ and 1000 $cm^{-1}$ correspond to the bending and rocking motion of Al-H groups in the crystal. Frequencies that are less than 500 $cm^{-1}$ correspond to rocking and translation motion of the ions in $Na_3AlH_6$ lattice.
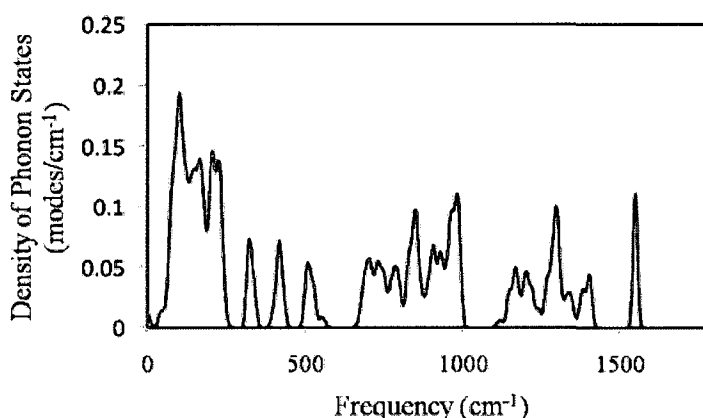


Figure 4.2 Phonon DOS spectrum of $Na_3AlH_6$.

From the evaluate phonon DOS, thermodynamic functions such as enthalpy, free energy, and entropy are calculated and are plotted as a function of temperature. Figures 4.3(a) and 4.3(b) show the agreement between the calculated values of change in enthalpy, entropy, and free energy as a function of temperature with the reported experimental values by Bonnetot et al., [126] from 0-300 K. Outputs from these calculations are further used in evaluating the free energies of decomposition of sodium alanate to yield hydrogen.
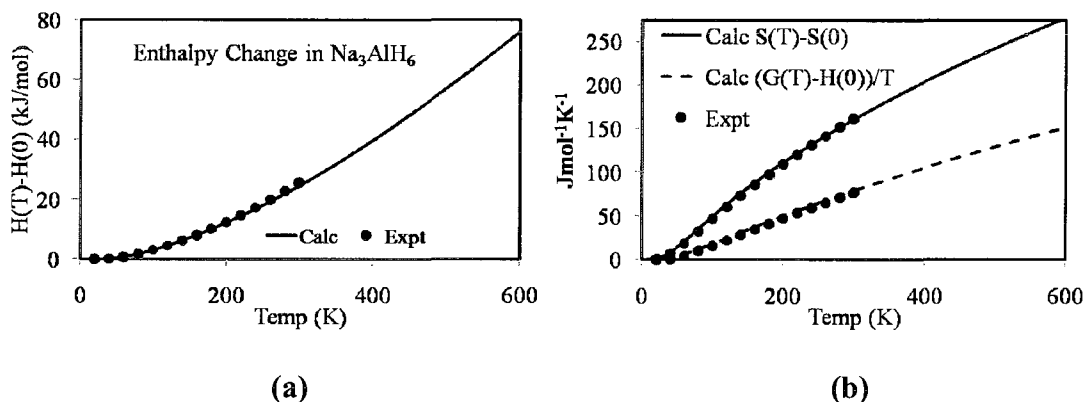
Figure 4.3 (a) Enthalpy and (b) free energy and entropy changes in $Na_3AlH_6$ as a function of temperature. Experimental values are taken from [126].

### 4.1.2.2 NaH and Al

Following the agreement between the calculated structural parameters and reported values of NaH and aluminum, further analysis on evaluating thermodynamic properties is done from phonon DOS. Here we present the phonon dispersion plots obtained from our calculations with frequency of phonon modes on the *y-axis* and high symmetric directions in the Brillouin zone along the *x-axis*. No imaginary modes are present in both plots that indicate a stable structure.

Figure 4.4(a) shows the phonon dispersion plot obtained from calculations of NaH. The phonon dispersion plot has a total of six frequencies that correspond to three acoustic and three optical modes. Acoustic modes have negligible dispersion coefficient near $\Gamma$ point and the three high frequency modes correspond to displacement of much lighter H compared to Na in NaH lattice. The highest frequency in NaH is equal to 878 $cm^{-1}$ and the two degenerate modes near $\Gamma$ point have a frequency equal to 470 $cm^{-1}$. In aluminum (Figure 4.4(b)), three frequencies correspond to the longitudinal phonons in the lattice that have dispersion equal to zero at the $\Gamma$ point. These results agree well with

the experimental observations. Hence, the thermodynamic functions derived from these calculations are well suited for evaluating the thermodynamics of hydrogen desorption in sodium alanates that is presented in next section.



(a)                                                    (b)
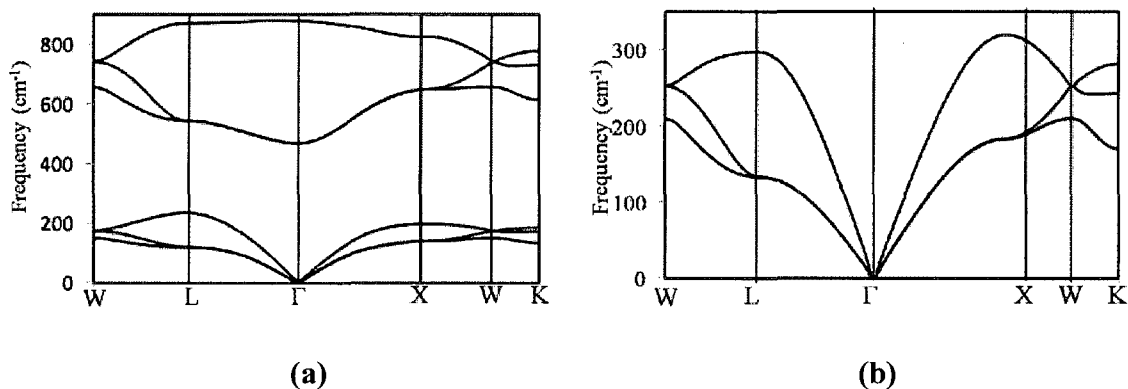
Figure 4.4 Phonon Dispersion plots of (a) NaH and (b) Al along the high symmetric direction in the Brillouin zone

### 4.1.3 Thermodynamics of NaAlH₄ Decomposition

Evaluated free energies and enthalpies of the decomposition reactions (Eqs. (1.1) and (1.2)) are plotted as a function of temperature in Figure 4.5. $\Delta G_{REACTION} = 0$ indicates the phase change from reactants to products, and the temperature associated with it is calculated and compared with the experimental observed values. This temperature signifies the start of the decomposition of sodium alanate phase and the evolution of hydrogen in the first reaction (Eq. (1.1)) and the decomposition of sodium aluminum hexahydride and the evolution of hydrogen in the second reaction (Eq. (1.2)).
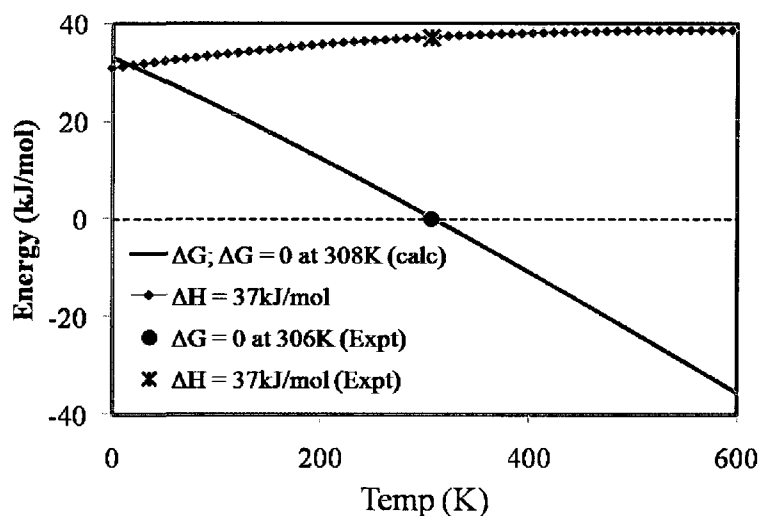
(a)
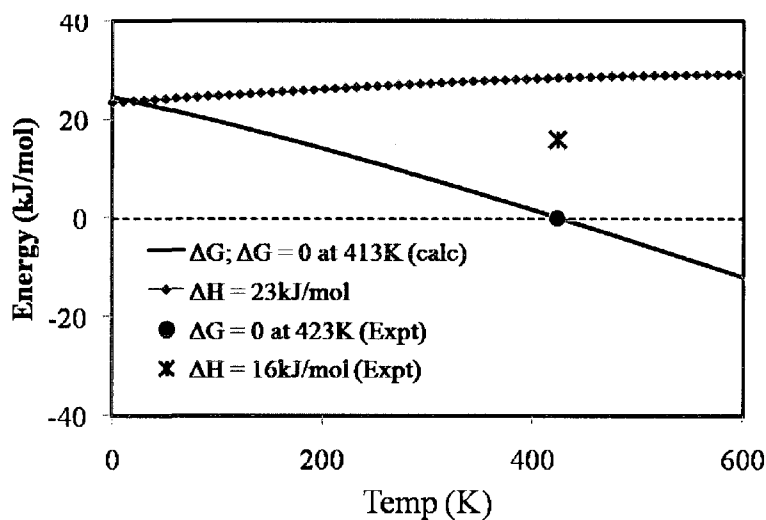


(b)

Figure 4.5 Thermodynamics of hydrogen desorption reactions in NaAlH$_4$. (a) First step of desorption reactions: Eq. (1.1) and (b) second step: Eq. (1.2). Red solid lines in both figures represent free energy changes; red dots represent enthalpies as a function of temperature, and the dotted line represents the zero reference. Experimental values in (a) are from [14] Experiment value for transition temperature in (b) is from [9] and enthalpy value from [15].

Solid lines represent temperature dependent free energies of the reactions, and the dotted lines represent the enthalpies of the reactions. The dashed line in Figure 4.5 represents the zero reference energy. From Figure 4.5(a), it is shown that the reaction is

predicted to take place at 308 K from polynomial fit of the values plotted. Enthalpies at various temperatures are plotted, and from the curve fit of the values, the enthalpy of the reaction at the reaction temperature is found to be 37 kJ/mol, which compares well with the reported value of 37 kJ/mol [14] determined from liquid state dehydriding, and 40.9 kJ/mol [15] determined from solid state dehydriding of $NaAlH_4$. In Figure 4.5b, the free energy line crosses the zero reference line (i.e. the free energy of reactants is equal to free energy of products) at 413 K, and the enthalpy of the reaction is predicted to be 23 kJ/mol, which is overestimated by 7 kJ/mol compared to experimental observation of 16 kJ/mol [15]. Transition temperatures of solid $NaAlH_4$ and $Na_3AlH_6$ are reported to occur between 306 K for one atm of hydrogen plateau pressure to 353 K for 7 atm of hydrogen plateau pressure [14] and 423 K [9], respectively.

### 4.1.4 Observations and Summary

From our calculations, we see all our conclusions compare well with the reported observations. Temperature of the desorption reaction predicted from Gibbs free energy of reactions predict a temperature of 306 K for the first reaction (Eq. (1.1)), and the enthalpy of the reaction is positive (~37 kJ/mol) over the range of temperatures from 0 to 600 K indicating it as an endothermic reaction. Entropy difference between the products and reactants in the first reaction (Eq. (1.1)), is equal to the change in entropy of hydrogen from condensed to gas phase. In 300-400 K range, calculated entropy of gaseous hydrogen from our DFT calculations is between 136-144 J $mol^{-1}$ $K^{-1}$, and the entropy change in the reaction is equal to 120-123 J $mol^{-1}$ $K^{-1}$. From this data we can conclude that the total entropy change in the reaction is equal to the entropy change due to transformation of hydrogen from condensed to gas phase, and the contributions from solids is negligible. This calculated entropy change is also in agreement with the reported

value of 130 J mol$^{-1}$ K$^{-1}$ for condensed to gas phase change in hydrogen [130]. In the second reaction (Eq. (1.2)), predicted values of reaction temperature and enthalpy of the reaction are 413 K and 23 kJ/mol, respectively. The discrepancies in calculated values at higher temperatures are due to the anharmonicity introduced in the vibrations, which is not very accurately predicted by the harmonic approximation used in the methodology. However, the calculated values closely approximate the macroscopic observables.

## 4.2 Kinetics of Hydrogen Desorption

Section 4.2 aims at understanding the fundamental reaction path involved in the decomposition of pristine sodium alanates for hydrogen desorption, and identifying the rate limiting steps in the reaction path using computational techniques. To the best of our knowledge, extensive investigation on the reaction paths in complex metal hydride decomposition leading to hydrogen evolution using theoretical methods has not been reported yet. In this study, the reaction progress leading to the formation of various phases is studied from a kinetic point of view using transition state theory. During the decomposition of pristine sodium alanate, the transition from $AlH_4^-$ to $AlH_6^{3-}$ is not clearly understood (Eq. (1.1)). Suggested progress of the first decomposition reaction is by transition from $AlH_4^-$ anion to $AlH_6^{3-}$ anion combined with nucleation and growth of the Al phase [8]. Early studies by Gross et al. using in-situ X-ray diffraction [9], have shown the possibility of transition through long range diffusion of heavier mass species than hydrogen. This observation is further supported by recent isotope scrambling experimental studies that indicate diffusion of hydrogen as the atomic or molecular species is unlikely to precede the diffusion of heavier mass species than hydrogen [46]. Recent computational studies by Gunaydin et al., [47] have shown the possibility of $AlH_3$

vacancy assisted hydrogen desorption and that the formation of $AlH_3$ vacancy is favorable over the NaH vacancy formation proposed by Walters et al., [48]. Possible reactions leading to the transition of $AlH_4^-$ to $AlH_6^{3-}$ studied here agree well with the reported computational and experimental observations [9]. This study is believed to provide a greater insight into the rate limiting steps in hydrogen desorption in sodium alanates that can later be applied to engineer other viable light complex metal hydrides as onboard storage materials.

### 4.2.1 Kinetics in Solids

Desorption of hydrogen from sodium alanates results in transition of the tetragonal phase of sodium alanate to a monoclinic sodium aluminum hexahydride, FCC Al phases, and gaseous hydrogen. Many proposed methods for predicting transition states thereby evaluating energy barriers in reactions are well suited for homogeneous fluid and gas phase transformations [81, 131-133]. In the case of solid-solid transitions, most material transformations include variation in cell vectors and rearrangement of atomic/molecular species in addition to short or long range diffusion that are not accurately described by the popular transition state search methods. Reports by Trinkle et al., [134] and Caspersen et al., [135] define solutions for phase transformations in solids though the solution proposed by the first group may lead to an physically unrealistic transition state as they define the change in cell vectors as a function of movement of nuclear coordinates. Solid state nudged elastic band method proposed by the later group is developed only for a single mechanism of martensitic transformation in steel that includes only movement of ions excluding diffusion. Desorption mechanism in complex metal hydrides include phase transformation from solid-solid and solid-gas (diffusion). Hence, global transformation from reactants phase to product phase is too difficult to

model. This problem of hydrogen desorption from $NaAlH_4$ is more research specific, and it requires a strategy to model the transformations rather than providing an algorithmic solution to determine the activation barriers.

### 4.2.2 Reactant and Product Models

In this study, local deformations in the reactant model to represent the seed for nucleation and growth of the resulting product phases are considered and activation energy for initiation of product phase is calculated. Calculations in this study require a slab model constructed based on the symmetry of the reactant phase, and a local region, with sufficient atomic/molecular species that can transform into a seed for product phase, is selected. The selected region is well isolated from its symmetric image in the adjacent cells. Different phases of transformation are modeled, and transition states connecting various local deformations are identified using synchronous search transition state methods as explained in Chapter 2, Section 2.1.2. From our calculations, we could predict the activation enthalpy and activation energy for transition from $AlH_4^-$ anionic species present in tetragonal $NaAlH_4$ to $AlH_6^{3-}$ anionic species present in monoclinic $Na_3AlH_6$ and yielding gaseous hydrogen.

In Section 4.2.2, we identify and study the possible reactions leading to hydrogen desorption mediated by diffusion of $AlH_3$ species in $NaAlH_4$. Transition from $AlH_4^-$ anionic species to $AlH_6^{3-}$ anionic species in the first step of decomposition reaction is proposed to follow the following reaction path:

$$2AlH_4^- \leftrightarrow AlH_3 + AlH_5^{2-} \qquad \text{(Eq. 4.4)}$$

$$AlH_5^{2-} + AlH_4^- \leftrightarrow AlH_6^{3-} + AlH_3 \qquad \text{(Eq. 4.5)}$$

$$2\,AlH_3 \leftrightarrow Al_2H_6 \qquad\qquad \text{(Eq. 4.6)}$$

$$\frac{1}{3}\,Al_2H_6 \leftrightarrow Al + H_2 \uparrow \qquad\qquad \text{(Eq. 4.7)}$$
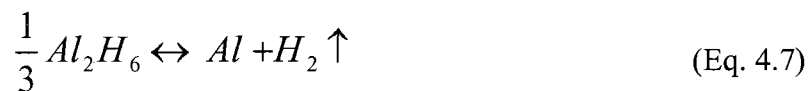
To model the reactions (Eqs. 4.4-4.7) to obtain the free energy (activation) barriers and heats of the reactions, the reactants and products are built and optimized using DFT combined with numerical basis sets, and all electron relativistic pseudopotentials as described in Chapter 2. Two layered slabs are used to identify the rate limiting steps to study the kinetics of hydrogen desorption in pristine sodium alanates. Transition state theory calculations are done as implemented in module DMoL$^3$ in the Materials Studio$^®$ software by Accelrys, Inc [136]. Initial structures of reactants and products are geometry optimized using GGA, PW91 correlation functional, all electron minimizer and numerical basis functions (DNP-double numerical plus polarization and diffuse functions). The reaction path connecting reactant and product is predicted using linear synchronous transit (LST) tools by Halgren and Lipscomb [84]. The transition state along the reaction path is found using combined linear and quadratic synchronous transit (LST/QST) methods. First the maximum along the reaction path is found using LST search and the resulting configuration minimized using conjugate gradients [137]. The obtained transition state is used to find a maximum using QST followed by minimization using conjugate gradients. This process is iterated until the true transition state is obtained, which is verified by confirming one imaginary frequency related to the maximum along the reaction coordinate and minimum along all other directions. Vibrational analysis is then performed on all the optimized configurations of the reactants, the products, and the transition states. Transition states are verified by

confirming one imaginary frequency related to the maximum along the reaction coordinate and minimum along all other directions. From the vibrational analysis, enthalpic and entropic contributions to the total free energy are obtained. Total free energy of each configuration is calculated by the difference between enthalpy (includes electronic energy) and temperature multiplied by entropy. All the free energies are divided by number of formula units in the reactant model.



(a) Reactant1          (b) Product1 / Reactant2

(c) Product 2/ Reactant3     (d) Product 3/ Reactant4     (e) Product 4
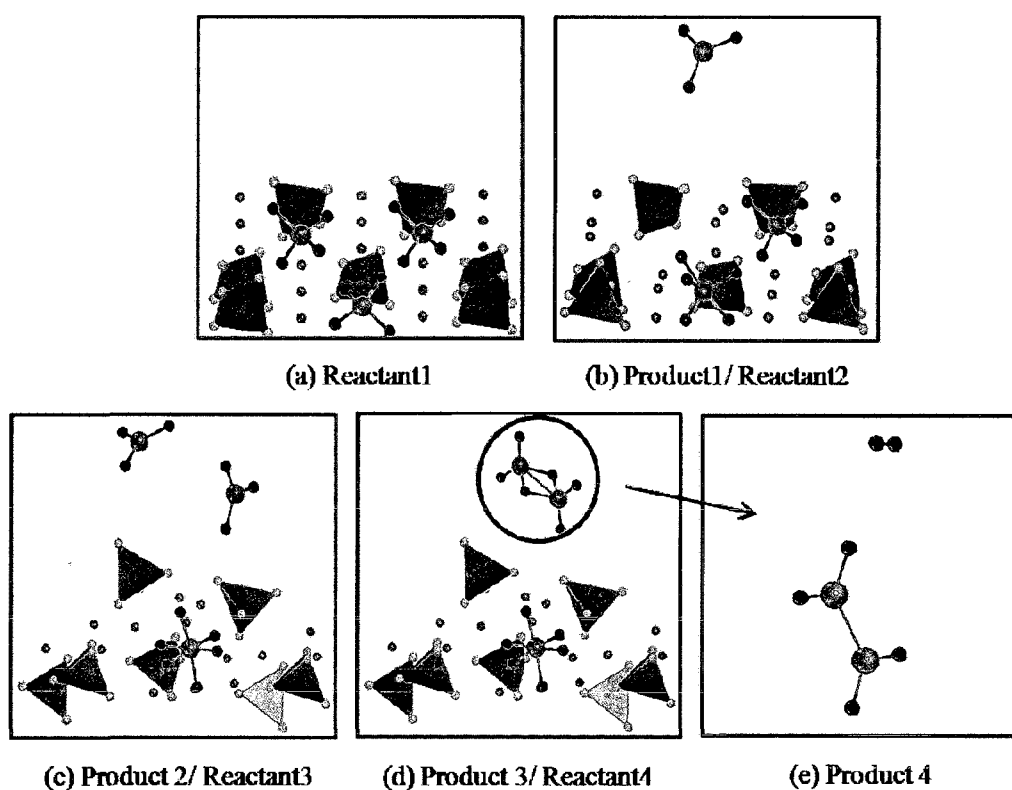
Figure 4.6 Models representing reactants and products in reactions listed in Eqs. 4.4-4.7. $AlH_4$ groups are shown in as polyhedrons, and Na ions are shown as balls. Colors in the figure indicate magenta-aluminum, grey-hydrogen, and purple-sodium. $AlH_4$ groups involved in reactions are represented in ball and stick model (magenta-aluminum and red-hydrogen).

In the first reaction (Eq. (4.4)), the reactant is the pristine $NaAlH_4$ slab (Figure 4.6(a) - Reactant1), and the product is built by dragging an $AlH_3$ unit from one of

the $AlH_4^-$ groups on surface, leaving the hydride ion in the lattice. Aluminum is constrained (zero degrees of freedom) in its position; however, the hydrogen atoms bonded to aluminum and the other groups in the slab are left unconstrained. Optimization calculations follow to obtain the relaxed geometry with optimized electron density and forces between the atoms (Figure 4.6(b); Product1/Reactant2). This procedure is followed to ensure the product configuration showing two distinct species resulting in the system. In the case of all the species are left unconstrained, configurations resulting from optimization would predict the reactant configuration as the reaction is endothermic, and reactant configuration is the optimum configuration among the two configurations (reactants and product).

The product from the first reaction shown in Eq.(4.4) (Figure 4.6(b); Product1/Reactant2), is taken as reactant for the second reaction, and the product for the second reaction (Eq. (4.5)) is modeled to represent the transition from $AlH_5^{2-}$ to $AlH_6^{3-}$ as shown in Figure 4.6(c) (Product2/Reactant3). In Figure 4.6(c), aluminums in created $AlH_3$ species are constrained, and the remaining groups in the lattice are unconstrained. The third reaction (Eq. (4.6)) represents the association of aluminum as in Figure 4.6(d) (Product3/Reactant4). In this product model, the lattice with $NaAlH_4$ groups is constrained and aluminums in $AlH_3$ species are left to result in a minimized state. The final step leading to evolution of hydrogen is the model in Figure 4.6(d) (Product3/Reactant4) and product (Figure 4.6(e); Product4) is modeled by dragging two hydrogens to form molecular hydrogen from the associated $AlH_3$ species in aluminum phase.

### 4.2.3 Kinetics Mechanism

The first reaction (Eq. 4.4) indicates one $AlH_4^-$ group, highlighted in Figure 4.6(a), possibly on the surface, losing one hydride species and forming an $AlH_3$ group that diffuses towards the $NaAl_3H_6$-Al interface. The extra hydride ion is shared by one of the nearest diagonally located $AlH_4^-$ groups (Figure 4.6(b)) forming $AlH_5^{2-}$ species along with rearrangement of two Na ions to satisfy the charge neutrality in the lattice. Further transition from $AlH_5^{2-}$ to $AlH_6^{3-}$ (Eq. 4.5) is possible by similar loss of a hydride ion from one of the nearest diagonally located $AlH_4^-$ groups and diffusion towards the formed $AlH_5^{2-}$ ion (Figure 4.6(c)). This transition creates another $AlH_3$ species that diffuses towards the $NaAl_3H_6$-Al interface. The single hydride ion diffuses towards the formed $AlH_5^{2-}$ ion transforming it into the $AlH_6^{3-}$ ion (Figure 4.6(c)) combined with rearrangement of Na ions to satisfy the charge neutrality. Movement of hydride ion from one $AlH_4^-$ group can be termed as reorientation and hopping from one $AlH_4$ tetrahedra to the other rather than diffusion of hydride species. The diffused $AlH_3$ species associate (Eq. (4.6)) and further decompose to evolve hydrogen leaving Al in its crystalline phase (Eq. (4.7)). As indicated in the first decomposition reaction (Eq. 1.1), three $NaAlH_4$ groups participate in the formation of one $Na_3AlH_6$ group, two Al species, and three molecules of hydrogen. Combining all the $AlH_4$ groups that are involved in transition and evolution of hydrogen, the stochiometry of the first decomposition reaction (three $AlH_4$ groups react resulting in one $AlH_6^{3-}$ anion, two metallic Al atoms and three $H_2$ molecules) is well detailed in the proposed reaction path in this study.

Various phases resulting from the preceding reactions are also present in the succeeding reactions to provide a realistic environment representing the experimental observations. These modeled reactions can be explained in a computational point of view

by saying all the eight formula units that are present in the reactant are still present in the product phase. This presence enables the calculation of energies of all the further phases resulting from reactant relative to the energy of reactant providing one reference to all the barriers and also providing cancellation of systematic errors. The reaction path is predicted using the LST tool and the transition state connecting the reactants and products is predicted using the combined LST/QST tool as explained in Chapter 2. The free energy barrier from reactants is computed by taking the difference between the free energies of transition state and the reactant.

### 4.2.4 Free Energy Barriers

Free energies of reactants, transition states, and products at finite temperatures are calculated by adding the free energy contributions to the electronic energies of the respective models and dividing by the number of formula units in the model. Figure 4.7 shows the calculated free energy barriers for the proposed set of reactions.
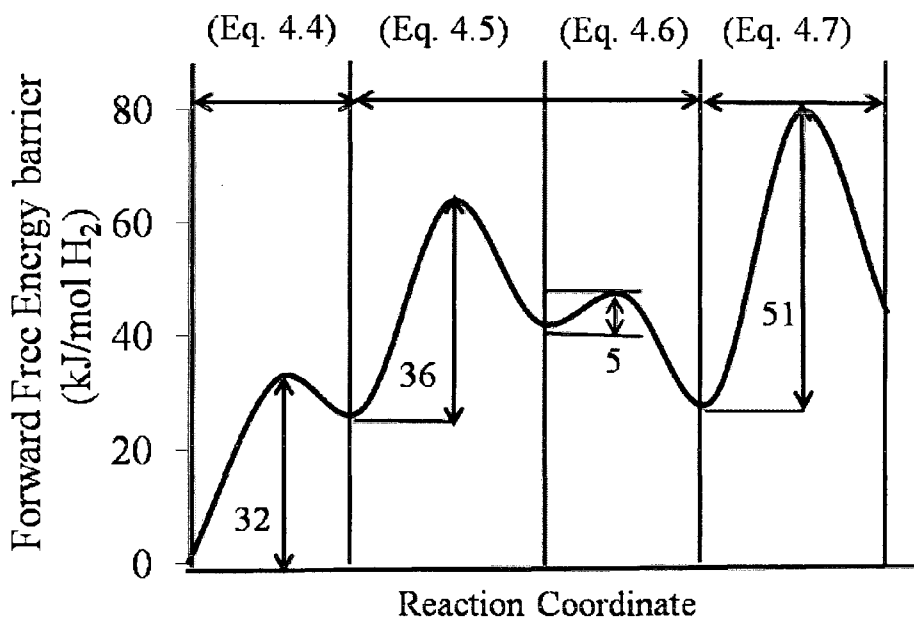
Figure 4.7 Forward free energy barriers at 298.15 K for the reactions (Eqs. 4.4-4.7) leading to transition from $AlH_4^-$ to $AlH_6^{3-}$ anion combined with nucleation of Aluminum and evolution of one $H_2$ molecule. Reaction numbers in the figure follow the order in proposed reaction pathway for first decomposition reaction of sodium alanates. All the free energies are in kJ/mol $H_2$. Total free energy barrier for the first decomposition reaction is 124 kJ/mol $H_2$.

Optimizing the modeled product of the first reaction in the proposed reaction path (Eq. 4.4), the hydride ion left in the lattice in place of $AlH_4^-$ group as well as the nearest diagonally located $AlH_4^-$ group move towards each other to form $AlH_5^{2-}$ ion (Figure 4.6(b)). $Na^+$ ions surrounding the vacant space left by the $AlH_4^-$ group on surface displace from their lattice positions and rearrange to bind with the formed $AlH_5^{2-}$ ion. Calculated forward free energy barrier at 298.15 K is 32 kJ/mol, corresponds to the first reaction leading to one $AlH_3$ species and transitioning from $AlH_4^-$ to $AlH_5^{2-}$. In the second (Eq. (4.5)) and the third reactions (Eq. (4.6)), leading to the transition from $AlH_5^{2-}$ to $AlH_6^{3-}$ combined with Al nucleation through association of created $AlH_3$ species, forward free energy barriers in the two steps correspond to 36 kJ/mol and 5 kJ/mol, respectively.

The fourth reaction (Eq. 4.7) resulting in evolution of hydrogen has shown a forward free energy barrier of 51 kJ/mol to release one molecule of hydrogen. The fourth reaction resulting in the release of one $H_2$ molecule from the associated $AlH_3$ species is the rate limiting step among the four reactions. Hence, the minimum energy required to release one $H_2$ molecule is equal to the energy required to cross the free energy barrier associated with the fourth reaction that is equal to 80 kJ/mol $H_2$. The enthalpy of activation from our calculations is equal to 82 kJ/mol $H_2$.

In the case of faster kinetics, the reactions follow the proposed order without any heat loss between the reactions. Otherwise, heat loss that occurs between the reactions is dissipated in the lattice and the total free energy barrier to release one molecule of hydrogen is equal to the sum of the free energy barriers associated with each reaction. The total free energy barrier associated with one molecule of hydrogen at 298.15 K, when the barriers in all the reactions are added, is equal to 124 kJ/mol $H_2$. Summing up the enthalpies of activation (determined from the difference between enthalpies of transition state and reactants at 298.15 K), total activation enthalpy for one hydrogen molecule release is determined as 120 kJ/mol $H_2$. Hence it can be concluded that our calculations predict the free energy barrier associated with one molecule of $H_2$ release lies in the range of 80-124 kJ/mol $H_2$ and the enthalpy of activation lies between 82-120 kJ/mol $H_2$. This observation is well in agreement with the reported value of the activation enthalpy of $\approx$120 kJ/mol $H_2$ [30].

Free energy of the reaction at 298.15 K is equal to 44 kJ/mol. Evaluating heats of reaction and summing up to determine the total heat of reaction for the first decomposition reaction, it is calculated to be equal to 49 kJ/mol $H_2$ that overestimates the

experimental reported heat of reaction of 38.5 kJ/mol [14]. This deviation from experimental observation is due to the calculation from intermediate transition phases instead of from the final fully grown sodium aluminum hexahydride and aluminum phases.

### 4.2.5 <u>Summary</u>

Pristine sodium alanates suffer from inherent limitations related to thermodynamics and kinetics of ab/desorption of hydrogen. In this dissertation, studied kinetic reaction paths leading to gaseous hydrogen revealed a four step reaction for transition from $AlH_4^-$ anion to $AlH_6^{3-}$ anion that completes one of the two proposed hydrogen desorption reactions in sodium alanates. Besides the above reaction path, diffusion of $AlH_3$ species in the lattice should also be considered in total hydrogen desorption from $NaAlH_4$ lattice. The diffusion barrier for $AlH_3$ species is reported to be 12 kJ/mol by Gunaydin et al., [47]. From all these reactions proposed, the rate limiting step determined is associated with hydrogen evolution form association of $AlH_3$ species nucleating aluminum phase. This step is 15 kJ/mol higher than the nearest highest barrier in the reaction path related to the transition from $AlH_5^{2-}$ to $AlH_6^{3-}$.

# CHAPTER 5

## STRUCTURE AND ENERGETICS OF

## Ti-DOPED NaAlH$_4$

In Chapter 5, vacancy and Ti dopant effects in the sodium alanate bulk, at the (001) surface, and on top of the (001) surface are studied considering Na lattice sites and interstitial sites. Structure and energetics of pristine and modified NaAlH$_4$ models are presented and discussed in terms of bond lengths, bond population analysis, TDOS, PDOS, and cohesive ($E_{coh}$), substitution ($\Delta E_{subst}$) and titanium-addition ($\Delta E_{add}$) energies. Results from DFT-MD simulations of the most possible optimized Ti-doped sodium alanates to study the structure and stability of Ti-Al-H complexes are also presented.

### 5.1 Bulk Models

A (2x2x1) supercell consisting of 16 NaAlH$_4$ units (Na$_{16}$Al$_{16}$H$_{64}$) with $N = 96$ atoms is built (as explained in Chapter 3, Section 3.5) by extending the tetragonal $I4_1/a$ sodium alanate cell twice along the '$a$' and '$b$' lattice dimensions. A Na atom inside the NaAlH$_4$ bulk occupying the B$_{Na}$ site is chosen to be removed (vacancy creation) or substituted by a Ti dopant. Hence, lattice models representing a vacancy at this Na bulk site (0→B$_{Na}$) and Ti in B$_{Na}$ site (Ti→B$_{Na}$) are constructed and geometry optimized using plane wave DFT techniques. Changes in structure due to vacancy (0→B$_{Na}$) and Ti dopant in NaAlH$_4$ bulk (Ti→B$_{Na}$) are discussed here.

85
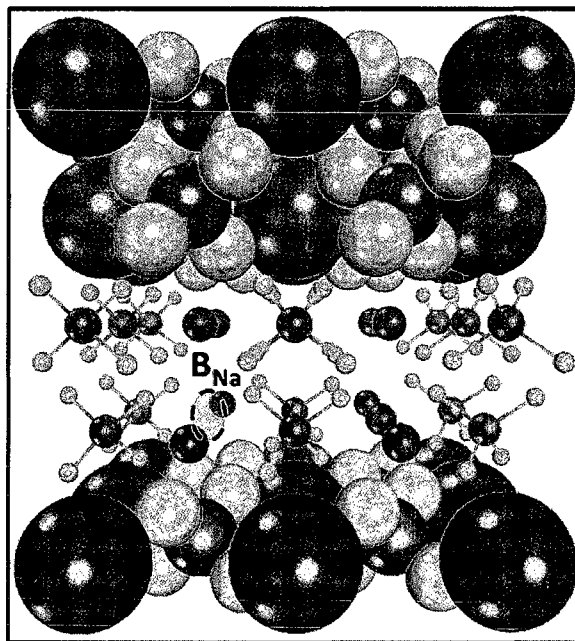
Figure 5.1 Model representing Na lattice site in bulk ($B_{Na}$) that is to be replaced by a vacancy or Ti dopant.

Calculations show that the lattice structure is preserved in both cases (0→$B_{Na}$ and Ti→$B_{Na}$); however, changes in bond lengths are seen mainly in the Ti→$B_{Na}$ case (Table 5.1). The first row in Table 5.1 represents the average $B_{Na}$ nearest neighboring Al-X bond lengths where X = Na (pristine), 0 (0→$B_{Na}$), and Ti (Ti→$B_{Na}$); that is, either the $B_{Na}$ site is occupied by Na, left vacant, or replaced by the Ti dopant. The native Al-Na bond length is 3.523 Å; however, when Na is substituted by Ti dopant, the new bond length, Al-Ti, is decreased by ~0.3 Å. The second row in Table 5.1 represents the average $B_{Na}$ nearest neighboring H-X bond lengths (X = Na, 0, Ti). The calculated H-Ti bond length is ~2 Å, which is 0.4 Å shorter than the corresponding Na-H in pristine sodium alanate. The third and fourth rows in Table 5.1 show values for the $B_{Na}$ nearest neighboring Al-H and Na-Al bond lengths. These Al-H bond lengths increased in the order of 0.06 Å for Ti→$B_{Na}$, whereas a slight increase in this distance (by 0.014 Å) is found when 0→$B_{Na}$. A

significant decrease in the Na-Al bond lengths (~0.12 Å) compared to the Al-H distances is found when titanium substitutes Na in $B_{Na}$, whereas the decrease in Na-Al distance when Na is substituted by a vacancy is in the order of 0.05 Å when compared to the pristine lattice. Finally, the fifth row in Table 5.1 represents the average Al-H bond lengths other than the $B_{Na}$ nearest neighboring distances in the $AlH_4$ groups. Relative to the Al-H bond lengths in pristine $NaAlH_4$, the corresponding distances decrease by 0.005 Å in the Ti→$B_{Na}$ case and remain almost the same when 0→$B_{Na}$.

Table 5.1 Bond distances between Al and H with vacancy (0) and Ti dopant in bulk Na site ($B_{Na}$).

| Species in $B_{Na}$ Site <br> Bond Lengths (Å) | Na | 0 | Ti |
|---|---|---|---|
| Al | 3.523 | - | 3.219 |
| H | 2.410 | - | 2.028 |
| Al – H <br> (Nearest Neighbors) | 1.612 | 1.583 - 1.626 | 1.599 - 1.671 |
| Na – Al <br> (Nearest Neighbors) | 3.523 | 3.477 | 3.400 |
| Al – H <br> (Average, other than nearest neighbors) | 1.612 | 1.611 | 1.606 |

All the structural differences found mainly when Ti→$B_{Na}$ can be attributed to the difference in atomic radii of sodium (1.86 Å) and titanium (1.47 Å) atoms. The presence of titanium dopants replacing the native sodium sites $B_{Na}$ results in a decrease of the lattice parameters and shows changes in the distances between sodium and hydrogen as well as aluminum and hydrogen. Elongation and therefore weakening of the Al-H bond in the presence of a Ti at $B_{Na}$ is observed and supported by calculations of density of states and electron density maps from the changes in the overall electronic structure [138].

Change in the electronic structure indicates possible formation of intermetallics such as Ti-Al and Ti-H compounds.

In order to get insights on Ti diffusion into the $NaAlH_4$ bulk, surface models of sodium alanate are built, and Ti-substituted surface Na as well as Ti addition in surface interstitial sites, and on-top Na and interstitial surface site models are investigated and discussed in the next section.

## 5.2 Surface and On-Top Surface Models

The (001) $NaAlH_4$ surface is investigated in this work (Figure 5.2). This surface is found to be closely packed and has the least surface energy compared to the $NaAlH_4$ (100), and (101) and higher order crystallographic planes such as (110) and (112) [27]. In order to facilitate modeling of Ti doping on and above the (001) $NaAlH_4$ surface, a two layer slab exposing the $NaAlH_4$ (001) crystallographic surface with a vacuum thickness of 5 Å is built by cleaving the 2x2x1 supercell to expose the (001) crystal surface (Figure 5.2). The total system consists of eight $NaAlH_4$ units ($Na_8Al_8H_{32}$) containing $N = 48$ atoms.
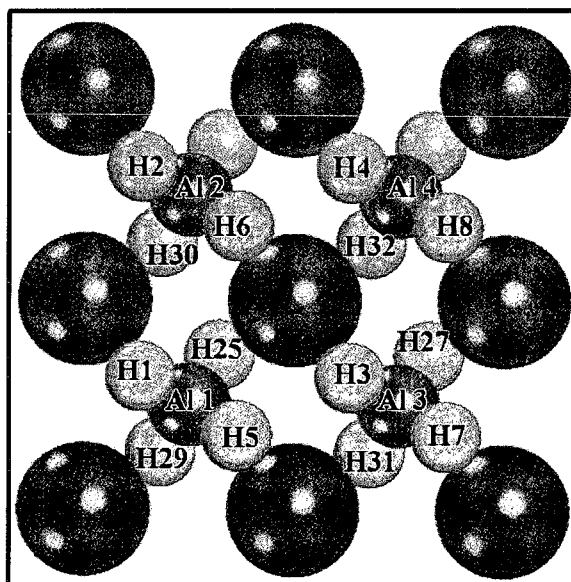
**(a)**
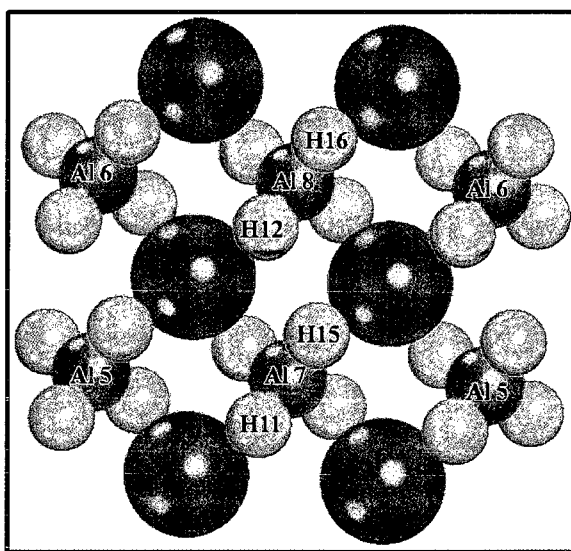


**(b)**

Figure 5.2 Top and bottom layers of (001) surface with atoms numbered. Atom numbers are referred to in the following text. In Figure 5.2(a), Na atoms in the corners and centers of the edges represent only one Na atom. In Figure 5.2(b), $AlH_4$ groups on the left side are symmetric images of the ones on right.

Four different models are constructed to investigate vacancy creation and effects of Ti dopants. Test sites for substitution/addition of point defects (Ti dopant) are

designated as 'S$_{Na}$' (Na lattice site in top layer) (Figure 5.3(a)), 'S$_I$' (interstitial site between two Na lattice sites and two Al lattice sites in top layer) (Figure 5.3(a)), 'T$_{Na}$' (site on top of S$_{Na}$) and 'T$_I$' (site on top of S$_I$) (Figure 5.3(b)). Hence, the four models considered are Ti→S$_{Na}$ (Ti-substituted Na at S$_{Na}$), Ti→S$_I$ (Ti added to the interstitial surface S$_I$ site), Ti→T$_{Na}$ (Ti placed on-top the surface S$_{Na}$ site), and Ti→T$_{.I}$ (Ti placed on-top the surface interstitial S$_I$ site).
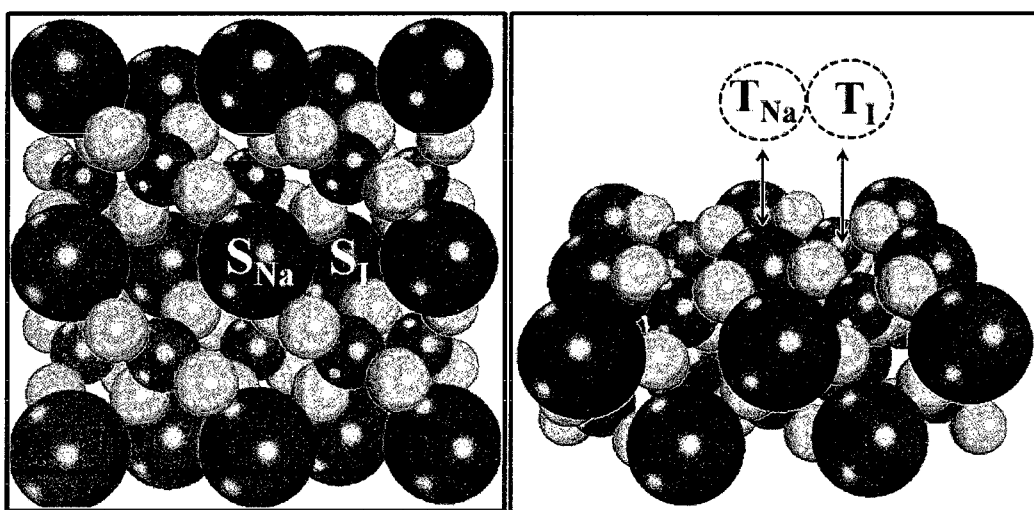


Figure 5.3 Models representing Na lattice sites and interstitial sites on (001) surface of NaAlH4 (a) Lattice and interstitial sites on surface and (b) Sites on top of lattice and interstitial sites. Four models are constructed by replacing the sites by Ti dopants Ti→S$_{Na}$, Ti→S$_I$, Ti→T$_{Na}$, and Ti→T$_I$.

Constructed models with titanium dopants on surface and on top of the surface are geometry optimized and ground state conformations are shown in Figure 5.4. The Ti dopant (red) at S$_{Na}$, (Ti→S$_{Na}$ model (Figure 5.4)), settles between the surface and sub-surface layers forming bonds with hydrogen and aluminum atoms in surrounding accessible AlH$_4$ groups. This phenomenon creates a distortion in the crystal lattice mainly due to the difference between ionic radii of titanium and sodium atoms. From the Ti local environment in the Ti→S$_{Na}$ model it is observed that the Ti atom coordinates to seven H

atoms at distances in the 1.81-1.97 Å range, and two aluminum atoms at distances in the 2.6-2.7 Å range. Up to eight hydrogen and five aluminum atoms have been found at distances from the Ti dopant in the 1.84-2.00 Å and 2.61-3.40 Å ranges, respectively in this case [27]. Since typical Ti-Al and Ti-H bond lengths in TiAl and TiH compounds such as $TiAl_3$ and $TiH_2$ are in the 2.7-2.9 Å [139], and in the order of 1.92 Å [140] respectively, the possible formation of a Ti-Al-H complex ($TiAl_2H_7$) is predicted in our calculations. In such a complex, the calculated average distance between Ti dopant and the two nearest neighboring Al atoms is 2.65 Å, and the seven nearest neighboring hydrogen atoms is 1.9 Å in very good agreement with bond lengths in typical TiAl and TiH compounds.
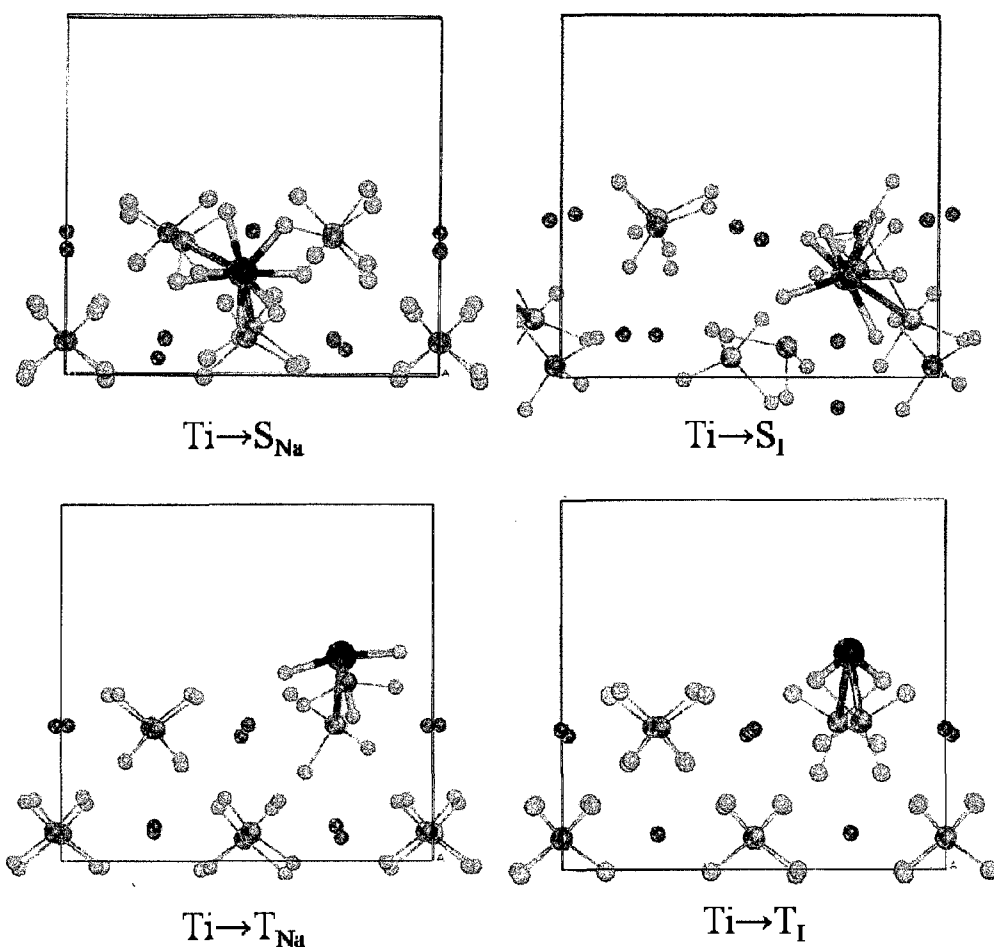
Figure 5.4 Optimized models of Ti-doped NaAlH4 models with Ti dopants present at surface and on top of surface lattice and interstitial sites.

The optimized Ti→$S_I$ model (Figure 5.4) shows that Ti dopant resides in the interstitial space right below the surface and forms a Ti-Al-H complex with neighboring lattice Al and H atoms. From the Ti dopant local environment in this model it is observed that the Ti coordinates to five H and three aluminum atoms at distances in the 1.81-1.90 Å and 2.51-2.93 Å (average 2.75 Å) ranges, respectively. Hence, the possible formation of a $TiAl_3H_5$ complex is seen in the Ti→$S_I$ case.

After placing the Ti dopant on top of the surface Na site, $T_{Na}$, (Ti→$T_{Na}$ model, Figure 5.4), it migrates to the $T_I$ site during the geometry optimization calculation. After

optimization is complete, the Ti dopant resides above the crystal surface and, therefore, little distortion is introduced in the NaAlH$_4$ lattice structure. In this case, a more localized Ti-Al-H complex is formed. The Ti atom is coordinated to three hydrogen and two aluminum atoms at distances in the 1.74-1.86 Å and 2.50-2.75 Å ranges, suggesting the possible formation of a TiAl$_2$H$_3$ compound. Similarly in the case of Ti→T$_I$ model (Figure 5.4), the Ti dopant resides above the crystal surface and, therefore, little distortion is introduced in the NaAlH$_4$ lattice structure. TiAl$_2$H$_2$ compound seems to form with Ti-H bond length of 1.73 Å and Ti-Al bond lengths in the range of 2.74-2.77 Å.

## 5.3 Cohesive, Addition and Substitution Energies

Cohesive energy is defined as the difference between the energy of the total system and the sum of the individual atomic energies. The substitution energy per atom of Na by X (= vacancy or Ti), $\Delta E_{subst}$, is defined by Eq. (5.1)

$$\Delta E_{subst} = \frac{E_{coh}(XNa_{n-1}Al_nH_{4n}) - E_{coh}(Na_nAl_nH_{4n})}{N}, \qquad \text{(Eq. 5.1)}$$

where $N$ is the total number of atoms in the model, $n = 16$ for bulk substitution and $n = 8$ for surface substitution, respectively, according to the lattice models used. The energies per atom resulting from titanium-addition to interstitial and on-top surface sites, $\Delta E_{add}$, is defined by Eq. (5.2).

$$\Delta E_{add} = \frac{E_{coh}(TiNa_8Al_8H_{32}) - E_{coh}(Na_8Al_8H_{32})}{N} \qquad \text{(Eq. 5.2)}$$

From the cohesive energy calculations (Table 5.2) is seen that Ti→B$_{Na}$ is 1.88 eV more stable than the pristine NaAlH$_4$, and the later is 6.85 eV more stable than the case in which a vacancy is created at B$_{Na}$ (0→B$_{Na}$). The cohesive energies of models Ti→S$_{Na}$, Ti→S$_I$, Ti→T$_{Na}$, and Ti→T$_I$, are higher than the corresponding pristine NaAlH$_4$ surface

model, and therefore possible. In order to analyze the preferred sites for titanium dopants on the (001) $NaAlH_4$ surface, the energy required to perform $Ti{\rightarrow}S_{Na}$, $Ti{\rightarrow}S_I$, $Ti{\rightarrow}T_{Na}$ and $Ti{\rightarrow}T_I$, with respect to the pristine case, is calculated. Hence, the substitution energy (Eq. 5.1) for the $Ti{\rightarrow}S_{Na}$ model and titanium-addition energies (Eq. 5.2) for the $Ti{\rightarrow}S_I$, $Ti{\rightarrow}T_{Na}$ and $Ti{\rightarrow}T_I$ models are computed. Calculations show that the energy required for such substitution/addition is $Ti{\rightarrow}S_{Na} \approx Ti{\rightarrow}T_I < Ti{\rightarrow}T_{Na} < Ti{\rightarrow}S_I$ (Table 5.2). The difference between the energy required for $Ti{\rightarrow}S_{Na}$ and $Ti{\rightarrow}T_I$ is 0.003 eV atom$^{-1}$, while the energy required for $Ti{\rightarrow}S_I$ is substantially higher than the corresponding one in the other three cases. Since the energy required for $Ti{\rightarrow}S_{Na}$ and $Ti{\rightarrow}T_I$ is less compared to others, these two sites ($S_{Na}$ and $T_I$) and probably $T_{Na}$ would be preferred by the Ti dopants over $S_I$. However, occupation of the $S_I$ sites by Ti dopant would be also possible at elevated temperatures due to increased in supplied energy as well as diffusion of the dopants on the surface and/or into the lattice.

Table 5.2 Cohesive energy relative to pristine system, $E_{coh}$*, Ti-addition energy, $\Delta E_{Ti}$, and substitution energy (vacancy (0) $\rightarrow$Na and Ti$\rightarrow$Na), $\Delta E_{subst}$.

| Site | Species in Site | System | $E_{coh}$* (eV) | $\Delta E_{Ti}$ (eV atom$^{-1}$) | $\Delta E_{subst}$ (eV atom$^{-1}$) |
|------|------|------|------|------|------|
| $B_{Na}$ | Na | $Na_{16}Al_{16}H_{64}$ | 0.00 | | |
| | 0 | $Na_{15}Al_{16}H_{64}$ | -6.85 | | -0.07 |
| | Ti | $TiNa_{15}Al_{16}H_{64}$ | 1.88 | | 0.02 |
| $S_{Na}$ | Na | $Na_8Al_8H_{32}$ | 0.00 | | |
| | 0 | $Na_7Al_8H_{32}$ | -6.68 | | -0.14 |
| | Ti | $TiNa_7Al_8H_{32}$ | 3.23 | | 0.07 |
| $S_I$ | Ti | $TiNa_8Al_8H_{32}$ | 6.58 | 0.13 | |
| $T_{Na}$ | Ti | $TiNa_8Al_8H_{32}$ | 3.89 | 0.08 | |
| $T_I$ | Ti | $TiNa_8Al_8H_{32}$ | 3.46 | 0.07 | |

Since the stable and probable structures based on energetics are Ti→$S_{Na}$ and Ti→$T_I$ models, these models are further discussed using results obtained from bond population, DOS and DFT-MD calculations.

## 5.4 Density of States and Bond Population Analysis

Similar DOS plots are obtained for the optimized Ti→$S_{Na}$ and Ti→$T_I$ models (Figure 5.5). Looking at the contributions from different atomic orbitals of Ti, Al and H species in doped-$NaAlH_4$ it is possible to elucidate the particular Ti-Al-H complexes that are believed to form when Ti→$S_{Na}$ and Ti→$T_I$ in $NaAlH_4$. A shift in the Fermi level towards the conduction band is seen with introduction of Ti dopant in the lattice at both, $S_{Na}$ and $T_I$ sites. The calculated band gaps, are respectively, 1.00 and 0.93 eV in the Ti→$S_{Na}$ and Ti→$T_I$ models. The pristine $NaAlH_4$ TDOS plot (Figure 5.5(a)) shows contributions from the $s$ orbital of hydrogen and the $p$ orbital of aluminum. The TDOS and PDOS of the Ti→$S_{Na}$ model (Figure 5.5(b)) show that the energy states found right below the Fermi level are mainly formed by contributions from the $d$ orbital of titanium, while in the case of Ti→$T_I$ (Figure 5.5(c)), they are formed by contributions from the $d$ orbital of titanium and $p$ orbital of aluminum.
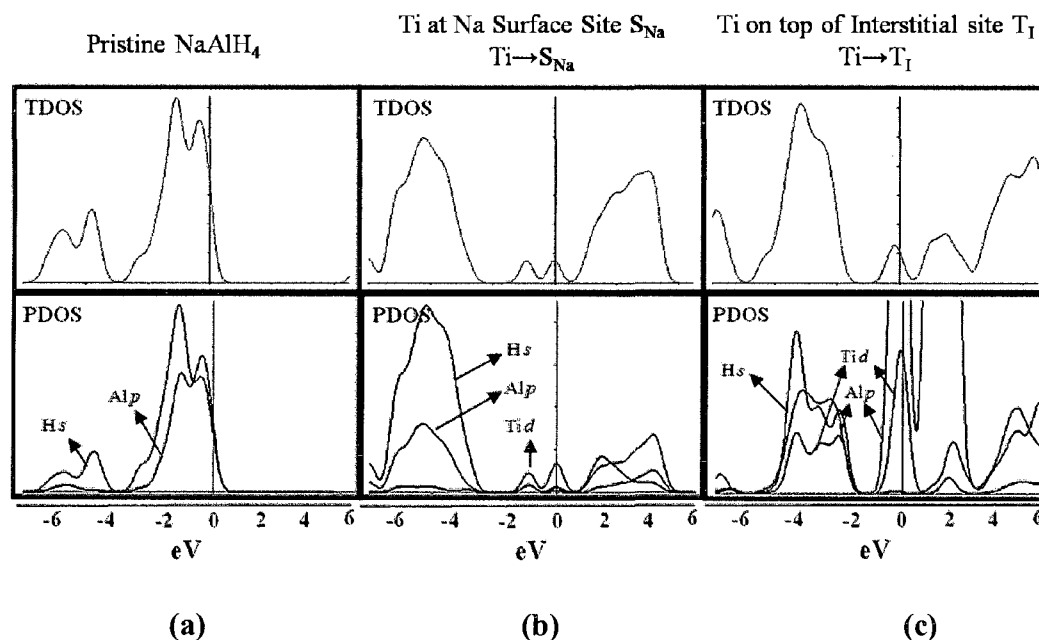
Figure 5.5 TDOS and PDOS plots from optimized (a) pristine, (b) Ti→S$_{Na}$ and (c) Ti→T$_I$ models.

Analysis of the bond strength is done by calculating overlap population in the bonds in Ti-Al-H complexes observed in optimized surface models. Overlap population in the bonds can be used to determine the covalence of a bond, and relative overlap population between two atoms in different compounds would indicate the degree of covalence of the same bond in different situations as explained in Chapter 2. In Ti→S$_{Na}$ model, two aluminum atoms and seven hydrogen atoms are seen with a positive bond population (Table 5.3) between observed bonds resulting in a TiAl$_2$H$_7$ complex. Bond population between the Ti-Al bonds show positive values that indicate the bonding state, and the covalence of the bond is not so high when measured on the scale of zero to one with one pointing to a highly covalent character. In case of Al-H bonds, bond population is decreased when compared with the identical Al-H bonds in optimized Ti→S$_{Na}$ model. Decrease in bond population indicates decrease in covalent character, which in turn

indicates the bonds between Al-H atoms are weakened due to the hydrogen atoms that were previously bonded only to aluminum are now shared between titanium and aluminum. Change in the bond length is also observed in Al-H bonds in the range of 0.03 to 0.2 Å. In Ti→$T_I$ model, two aluminum atoms and two hydrogen atoms are seen with a positive bond population resulting in $TiAl_2H_2$ complex. In this case, relatively high overlap population is seen in Ti-Al and Ti-H bonds.

Table 5.3 Bond population analysis of observed $TiAl_2H_6$ and $TiAl_2H_2$ complexes in optimized Ti→$S_{Na}$ and Ti→$T_I$ models. Values in parentheses represent the bond populations in pristine $NaAlH_4$ structure.

| Ti at Na Lattice Site ($S_{Na}$) | | | | | |
|---|---|---|---|---|---|
| Bond | Bond Population | Bond Length | Bond | Bond Population | Bond Length |
| Ti-Al2 | 0.18 | 2.581 | Al3-H3 | 0.67 (0.89) | 1.643 (1.609) |
| Ti-Al8 | 0.24 | 2.729 | Al8-H12 | 0.32 (0.81) | 1.829 (1.619) |
| Ti-H3 | 0.11 | 1.944 | Al7-H15 | 0.63 (0.81) | 1.666 (1.619) |
| Ti-H12 | 0.43 | 1.813 | Al1-H25 | 0.61 (0.81) | 1.664 (1.620) |
| Ti-H15 | 0.21 | 1.925 | Al2-H30 | 0.42 (0.81) | 1.735 (1.620) |
| Ti-H25 | 0.13 | 1.969 | Al4-H32 | 0.56 (0.81) | 1.696 (1.620) |
| Ti-H30 | 0.28 | 1.853 | | | |
| Ti-H32 | 0.16 | 1.974 | | | |
| Ti on top of Interstitial Site ($T_I$) | | | | | |
| Bond | Bond Population | Bond Length | Bond | Bond Population | Bond Length |
| Ti-Al3 | 0.67 | 2.772 | Al3-H3 | 0.00 (0.89) | - |
| Ti-Al4 | 0.67 | 2.740 | Al4-H8 | 0.00 (0.89) | - |
| Ti-H3 | 0.52 | 1.733 | Al3-H27 | 0.71 (0.81) | 1.643 (1.620) |
| Ti-H8 | 0.52 | 1.734 | Al4-H32 | 0.70 (0.81) | 1.644 (1.620) |

In Ti→$S_{Na}$ model, Ti is coordinated to two aluminum and seven hydrogen atoms resulting in the possible formation of a $TiAl_2H_7$ complex. These selected Ti-Al and Ti-H bonds (Figure 5.4) have positive bond population. Moreover, since the individual Al-H bond lengths increase with respect to the bonds in the pristine lattice, it is seen that the

Al-H bond lengths in the AlH$_4$ groups are weakened (by 0.03 to 0.20 Å) suggesting the possible formation of a TiAl$_2$H$_7$ complex.

In the case of Ti→T$_I$, Ti is coordinated to two aluminum and two hydrogen atoms resulting in the possible formation of a TiAl$_2$H$_2$ complex. Moreover, since the individual Al-H bond lengths increase with respect to the bonds in the pristine lattice, it is seen that the Al-H bond lengths in the AlH$_4$ groups are weakened (by 0.20 Å) suggesting the possible formation of a TiAl$_2$H$_2$ complex. Hydrogen atoms H3 and H8 (Figure 5.2) that were previously bonded to aluminum in pristine NaAlH$_4$, have shown no significant interaction with Al after optimization of the Ti→T$_I$ model which is shown by their zero bond population values. Aluminum atoms are at a distance of 2.75 Å from the Ti atom and hydrogen atoms at 1.77 Å in the TiAl$_2$H$_2$ complex. The energy required to free the hydrogen atoms bound to AlH$_4$ groups in pristine NaAlH$_4$ is decreased due to introduction of titanium resulting in the TiAl$_2$H$_7$ and TiAl$_2$H$_2$ complexes with hydrogen atoms shared between Al and Ti. DOS of Ti doped NaAlH$_4$ and bond population analysis of Ti-Al-H complexes, illustrates a possible catalytic role of Ti, i.e. lowering the formation energy of AlH$_3$-type species and, therefore, the barrier for H$_2$ desorption.

Our DFT results show that the complex observed in Ti→T$_I$ model is a precursor to the complexes observed in Ti→S$_I$ and Ti→T$_{Na}$ models when subjected to elevated temperatures. Hence, further analysis is concentrated on the Ti-Al-H complexes that are believed to form in the Ti→S$_{Na}$ and Ti→T$_I$ models. For this reason, in the next section, the dynamics of TiAl$_2$H$_7$ and TiAl$_2$H$_2$ complexes over time at different temperatures are discussed, and insights into the diffusion of Ti dopants in the NaAlH$_4$ lattice are presented.

## 5.5 Dynamics of Ti-Al-H Compounds in Ti-Doped NaAlH$_4$

The time evolution of TiAl$_2$H$_7$ (Figure 5.6) and TiAl$_2$H$_2$ (Figure 5.7) complexes formed in Ti→S$_{Na}$ and Ti→T$_I$ models at 423 and 448 K are investigated with DFT-MD simulations. Initial total environment around dopant is shown in Figure 5.4, Ti→S$_{Na}$ (TiAl$_2$H$_7$) and Ti→S$_I$ (TiAl$_2$H$_2$), and subsequent pictures in Figures 5.6 and 5.7 show the snapshots of the local complex environments at three different time intervals (0, 1, and 2 ps) at both temperatures, respectively. Different views are taken in Figures 5.6 and 5.7 with respect to Figure 5.4 for better visualization of the complexes and association of aluminum atoms. In Figure 5.7 the atoms circled black represent hydrogen atoms that hop from neighboring AlH$_4$ groups to dopant accessible AlH$_4$ groups.

From the results of DFT-MD simulations of Ti→S$_{Na}$ model at 423 K and 448 K, it is noticed that the Ti dopant settles between surface and subsurface layers, and no further diffusion into the lattice is seen. The neighboring six AlH$_4$ groups are drawn towards the Ti dopant, and increased association of aluminum atoms as well as hydrogen atoms with Ti is found after dynamics at 423 and 448 K.
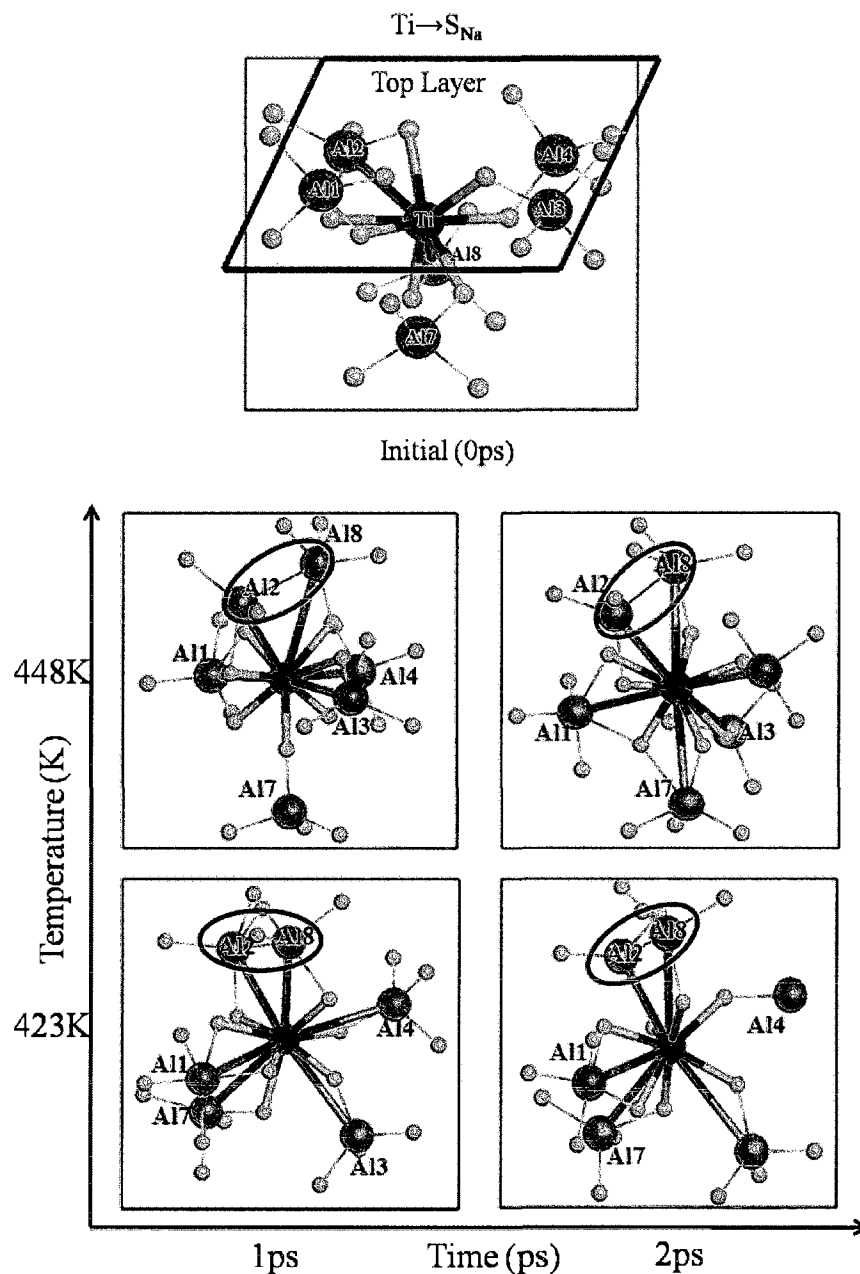
Figure 5.6 Snapshots showing the time evolution of TiAl₂H₇ complexes in Ti→S_Na model at two time steps from DFT-MD simulations at 423 and 448 K. Atom colours: Red (Ti), magenta (Al), and grey (H).

After 1 ps at 423 K, the number of aluminum atoms coordinating with titanium in the complex increase from two (at distances in the 2.6-2.7 Å range) to five (at distances in the 2.6-2.7 Å range). The number of hydrogen atoms (seven) coordinating with

titanium are at distances in the 1.76-2.02 Å range, resulting in the possible formation of TiAl$_5$H$_7$ complex at 423 K after 1 ps. Besides the formation of a Ti-Al-H complex, Al-Al association (with a 2.97 Å bond length) is also seen from the DFT-MD results at this temperature. After 2 ps, no significant changes are observed in the complex except for the rearrangement of the Ti-Al-H complex with the Al2-Al8 bond length of 2.62 Å. All the other bond lengths remain unaltered. When temperature is set to 448 K, no significant changes in the TiAl$_5$H$_7$ complex is seen over time. Rearrangement of Al and H atoms in this complex is, however, observed, but the number of hydrogen and aluminum atoms associated with the complex remains the same. The Al-Al distance reduces to 2.78 Å and 2.46 Å after 1 and 2 ps, respectively, at this temperature.

Changes observed in the strength of the bonds calculated over the presence of covalent character of the formed bonds are done by bond population analysis. From the tabulated bond population values of Ti→S$_{Na}$ model after 1 ps (bond population of Ti-H are not shown) in Table 5.4, we can see that the six coordinating hydrogen atoms and five coordinating aluminum atoms in TiAl$_5$H$_6$ have positive overlap population indicating presence of physical bonds in the complex. After 2 ps, seven hydrogen atoms and five aluminum atoms have shown positive overlap population. Al-Al bond population is significantly high (0.55 after 1 ps and 0.58 after 2 ps) indicating a strong covalent bond between the two aluminum atoms. At 448 K, rearrangement of overlap populations between the coordinating hydrogen aluminum atoms is seen, but the Al-Al bond population has increased to 0.67 and 0.71 after 1 and 2 ps indicating increase in bond strength with increase in temperature. Looking at the bond distances between coordinating aluminum atoms and Titanium dopant, TiAl$_5$H$_7$ is possible; however, when

also taking bond population analysis of the Ti-Al-H complexes over time and at different temperatures in case of Ti→$S_{Na}$ into account, it is seen that the $TiAl_2H_7$ complex becomes $TiAl_3H_7$ at 423 K (three aluminums and seven hydrogens with positive bond population) and $TiAl_4H_7$ (four aluminums and seven hydrogens with positive bond population) at 448 K.

Table 5.4 Calculated bond population values at different time steps at different temperatures from MD simulations of Ti→$S_{Na}$ and Ti→$S_l$ models.

| Bond | 0ps | 423 K | | 448 K | |
|---|---|---|---|---|---|
| | | 1 ps | 2 ps | 1 ps | 2 ps |
| **Ti Dopant at Lattice Site ($S_{Na}$)** | | | | | |
| Ti-Al1 | - | - | - | 0.04 | 0.04 |
| Ti-Al2 | 0.18 | 0.18 | 0.04 | 0.2 | 0.11 |
| Ti-Al4 | - | - | - | 0.07 | - |
| Ti-Al7 | - | 0.15 | 0.07 | - | 0.02 |
| Ti-Al8 | 0.24 | 0.23 | 0.2 | 0.2 | 0.1 |
| Al2-Al8 | | 0.55 | 0.58 | 0.67 | 0.71 |
| **Ti Dopant on Top of Interstitial Site ($T_l$)** | | | | | |
| Ti-Al3 | 0.67 | 0.51 | 0.46 | 0.58 | 0.38 |
| Ti-Al4 | 0.62 | 0.38 | 0.56 | 0.58 | 0.37 |
| Ti-Al6 | | 0.09 | 0.05 | - | - |
| Ti-Al8 | | | | 0.01 | 0.03 |
| Na-Al3 | | | | | 0.27 |
| Na-Al4 | | | | | 0.03 |

In the case of Ti→$T_l$ model where the $TiAl_2H_2$ complex is formed, diffusion of dopant into the $NaAlH_4$ lattice is seen with temperature (Figure 5.7) through the top layer with final settling between surface and sub-surface layers. At 423 K and after 1 ps (Figure 5.7), the number of aluminum atoms coordinating with Ti dopant (at distances in the 2.57-2.76 Å range) increases from two to three, and the number of coordinating hydrogen atoms (at distances in the 1.74-2.00 Å range) increase from two to six, resulting in the formation of a $TiAl_3H_6$ complex. After 2 ps at 423 K, the complex remains same

with rearrangement of associated aluminum and hydrogen atoms. Hydrogen hops from one $AlH_4$ group to another after 2 ps at 423 K.
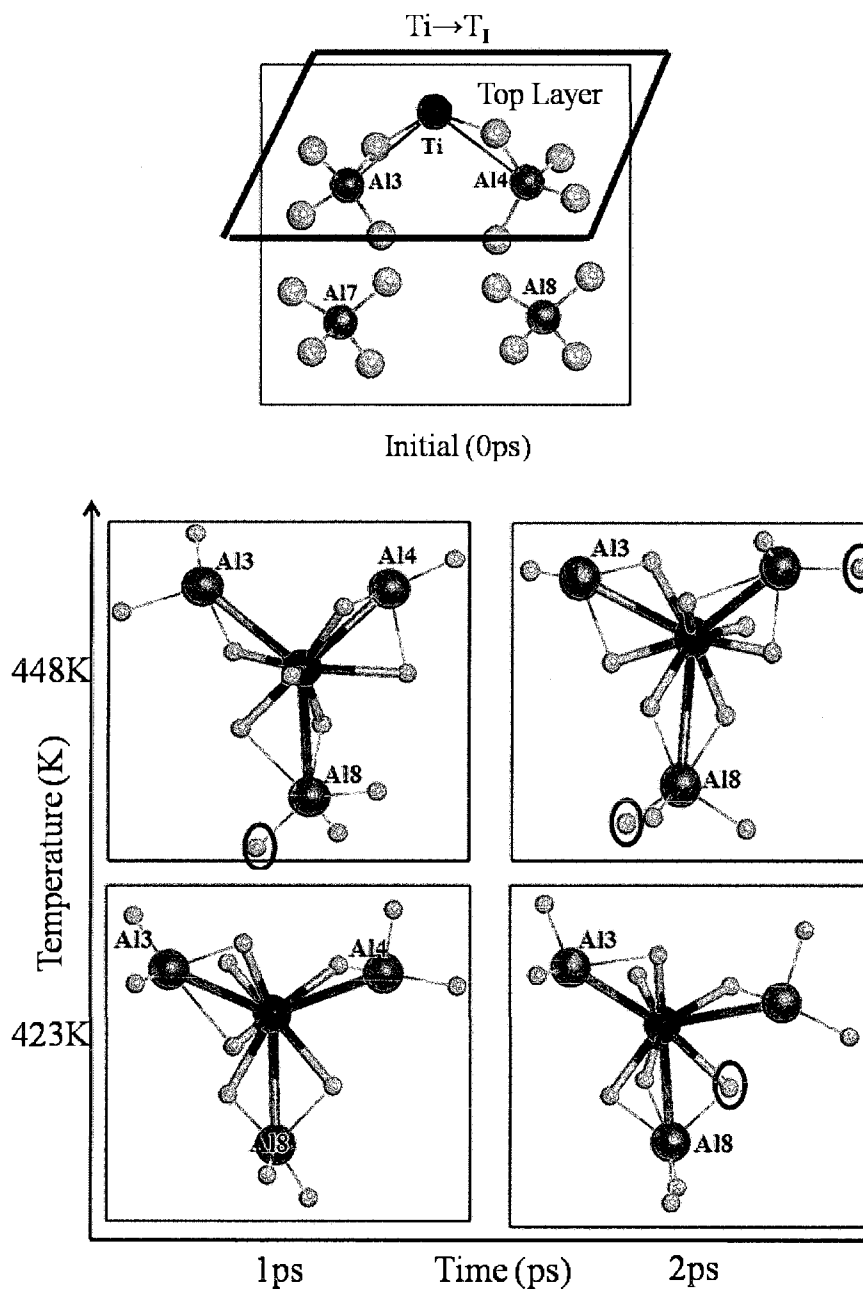


Figure 5.7 Same as Figure 5.6 for $TiAl_2H_2$ in Ti→$T_1$ model. Hydrogen atoms encircled in black represent number of hydrogen atoms associated with the complex as a result of hydrogen hopping from $AlH_4$ groups other than that are shown in the picture.

At 448 K and after 1 ps, the Ti-Al-H complex is the same as the one found after 2 ps at 423 K ($TiAl_3H_6$). After 2 ps at this temperature, the coordinating aluminum atoms remain the same (at an average distance of 2.73 Å from Ti), and coordinating hydrogen atoms increase from six to seven (at distances from Ti in the 1.69-1.97 Å range), resulting in the formation of a $TiAl_3H_7$ complex.

From the bond population analysis of the Ti-Al-H complexes over time and at different temperatures in case of Ti→$T_I$, it is seen that the $TiAl_2H_2$ complex becomes $TiAl_3H_6$ (three aluminums and six hydrogens with positive bond population) at 423 K and $TiAl_3H_7$ (three aluminums and seven hydrogens with positive bond population) at 448 K. From the observed complexes in case of Ti→$T_I$ model at different temperatures, formed complexes is possible with diffusion of Ti dopants on the surface and into the lattice, penetrating through the interstitial site on the surface ($S_I$). From this result it is predicted that the Ti dopant placed initially at a $T_{Na}$ site would diffuse on the surface and penetrate through the interstitial site based on aforementioned discussions. The precursor to this state is seen in the optimized model where the Ti placed at $T_{Na}$ site is settled on top of $S_I$ site, resulting in the formation of a $TiAl_2H_3$ complex. From the optimized model of Ti→$S_I$ model, it is seen that the $TiAl_3H_6$ complex is formed, which is observed by exposing the Ti→$T_I$ model to elevated temperatures.

## 5.6 Observations and Discussion

When compared to the presence of dopants in bulk and surface, $NaAlH_4$ with Ti dopants in bulk tends to be less stable than the case with Ti dopants on surface as observed from the differences in cohesive energies of the different models presented here. From the cohesive energy point of view, Ti→$S_I$ is the most stable conformation

possible. Looking at the energy required to introduce dopants in NaAlH$_4$ lattice through titanium substitution and titanium addition energies ($\Delta E_{subst}$ and $\Delta E_{add}$), bulk substitution is favorable followed by Ti→S$_{Na}$ and Ti→T$_I$. The first step for the dopant before substitution at the lattice site would be to adsorb on the surface and diffuse into the lattice. Hence the preferred sites for Ti dopants to adsorb after initial mechanochemical milling process may be estimated by comparing the possible sites for surface substitution. From the constructed models to simulate NaAlH$_4$ (001) surface doping, two possibilities of substitution at Na lattice site (Ti→S$_{Na}$) as well as substitution on top of interstitial site between two Na and two Al atoms (Ti→T$_I$) have equal probability since the energy required to do that is similar in both cases.

From DFT simulations it is found that the Ti dopant prefers to settle between surface and subsurface layers in case of Ti→S$_{Na}$ and Ti→S$_I$ models, and on the surface in case of Ti→T$_{Na}$ and Ti→T$_I$ models. Optimization of configurations with the Ti dopant placed at possible sites on the NaAlH$_4$ surface (T$_{Na}$, S$_I$ and T$_I$ ) result in the same model after simulating dynamics at elevated temperatures. Formation of TiAl$_2$H$_6$ and TiAl$_2$H$_2$ depend upon the accessible AlH$_4$ groups from the Ti local environment. These complexes are shown to weaken the Al-H bonds in AlH$_4$ complexes since the hydrogen atoms that were previously bonded only to an aluminum atom are now shared between the Ti dopant and aluminum atom. This effect would help in lowering the required energy for hydrogen desorption from the doped-NaAlH$_4$ lattice, facilitating hydrogen desorption by forming a multi atomic complex.

Ti dopants replacing Na atoms would result in a complex with Ti surrounded by all the adjacent six AlH$_4$ groups in case of the NaAlH$_4$ lattice structure. Although only

two aluminum atoms have shown a positive overlap population (at bonding distances of 2.6 Å and 2.7 Å), the remaining Al atoms are at distances in the 3.00-3.40 Å range. This Ti dopant surrounded by six Al atoms can be interpreted as the reported Ti-Al solid solution observed after mechanochemical milling of $NaAlH_4$ and $TiCl_3$ [141]. Since the Ti dopants on the (001) NaAlH4 surface also have equal probability, a more localized complex is seen in Ti→$T_I$, since Ti dopant has access to only two $AlH_4$ groups. $TiH_2$ formation is also observed.

From the dynamics of the formed Ti-Al-H complexes at different temperatures, it is seen that Ti dopant prefers to reside between surface and subsurface layers with no further diffusion into the lattice irrespective of the surface model under consideration. After that diffusion process, mobility of $AlH_4$ groups is observed towards the Ti dopant, resulting in association of more Al atoms with Ti dopants over time at different temperatures. After 2 ps simulation, we have seen Ti forming bonds with five Al atoms and six hydrogen atoms in case of Ti→$S_{Na}$, and three aluminums and six hydrogen atoms in case of Ti→$T_I$. Complex in the case of Ti→$S_{Na}$ model seems like a precursor to the phase with atomic Ti dispersed in aluminum. The complex observed in case of Ti→$T_I$ model seems like a precursor to the $TiAl_3$ phase since association of Ti with three Al atoms is seen with formed Ti-Al bonds.

## 5.7 Summary

In Chapter 5, the preferred sites for titanium dopants in $NaAlH_4$ and the formation of various key intermetallics for improved hydrogen kinetics of sodium alanates is investigated using density functional theory (DFT) with plane-wave basis and PW91 functional. The $NaAlH_4$ lattice structure and stability upon Ti-substituted bulk and

surface Na sites, as well as Ti addition in surface interstitial sites and Ti on-top Na and interstitial surface sites, are investigated. Equal probability of Ti dopant substitution at both lattice and interstitial Na sites in the (001) $NaAlH_4$ surface is found from substitution energies calculations. The composition of Al and H in the observed Ti-Al-H complexes depends on the accessible $AlH_4$ groups around the Ti dopant, and $TiAl_2H_7$ and $TiAl_2H_2$ are found to form after geometry optimization calculations. Periodic density functional theory coupled molecular dynamics (DFT-MD) simulations are then conducted in order to understand the temperature effect on titanium atom diffusion on the doped-$NaAlH_4$ following chemisorption at 423 and 448 K. Results have shown the existence of the observed Ti-Al-H complexes as well as increased association of Al and H with the complexes as time evolves at both temperatures. From DFT-MD simulations it is seen that the $TiAl_2H_7$ complex becomes $TiAl_3H_7$ at 423 K and $TiAl_4H_7$ at 448 K in the case of Ti substitution in the surface Na site, and that the $TiAl_2H_2$ complex becomes $TiAl_3H_6$ at 423 K and $TiAl_3H_7$ at 448 K in the case of Ti substitution on top of the interstitial surface site. The complexes observed after geometry optimization represent the TiAl solid solution observed after ball milling of $TiCl_3$-doped $NaAlH_4$, and the complexes at elevated temperatures represent precursors to amorphous $TiAl_3$ and atomic Ti dispersed in aluminum, making this study consistent with experimental observations.

# CHAPTER 6

## THERMODYNAMICS AND KINETICS OF

## Ti-DOPED NaAlH$_4$

Based on the agreement of calculated values with the reported experimental observations, which validates our calculations in predicting the thermodynamics of hydrogen desorption in sodium alanates, thermodynamics of Ti-doped sodium alanates are studied and reported in Chapter 6. Upon introduction of titanium salts, the thermodynamics of hydrogen decomposition is reported to be improved. This improvement could possibly result from the formation of Ti-Al phases or Ti-Al-H phases that could directly or indirectly help the transition from one anionic species to other thereby improving the thermodynamics of hydrogen desorption [142]. The next section discusses about the possible phases that could result on introduction of Ti dopants in pristine sodium alanates. TiCl$_3$ salt is used as reacting species with NaAlH$_4$ as TiCl$_3$ is reported as the best catalyst to date [17].

Followed by predictions of the kinetic path for transition of AlH$_4^-$ to AlH$_6^{3-}$, the second step is to predict the role of titanium dopants from optimized conformations of Ti-doped sodium alanate models and time dependant dynamics of Ti-doped models at elevated temperatures. Combined density functional theory and molecular dynamics methods are used to evaluate and report the observations.

## 6.1 Thermodynamics of Ti-doped NaAlH$_4$

In Section 6.1, thermodynamic reaction pathways resulting in Ti-Al complexes followed by dehydrogenation of sodium alanate are studied. Out of total six thermodynamic reaction pathways of TiCl$_3$ doped NaAlH$_4$ studied in this dissertation, first four reaction pathways are deduced from observations reported in the literature. A brief review of literature is presented here pertaining to Ti-doped sodium alanates. Following the reported improvement of thermodynamics of hydrogen desorption by Ti-doped sodium alanates in 1997 [8], in situ X-ray diffraction studies by Gross et al., in 2000 [9] and 2002 [30] have shown the formation of metallic Al phase after ball milling NaAlH$_4$ with TiCl$_3$. Gross et al., [30] have also shown the presence of TiCl$_3$ is necessary in formation of metallic Al since undoped NaAlH$_4$ did not result in Al peak after high energy ball milling. Further research by Mazjoub et al., [49] have shown the results consistent with the reaction with products including NaCl, TiAl$_3$, and gaseous hydrogen from X-ray diffraction experiments. Proposed reaction by Weidenthaler et al., [143] from XRD studies include the product phases of metallic Ti and Al along with sodium chloride salt upon ball milling of NaAlH$_4$ with TiCl$_3$ and formation of TiAl$_3$ alloy at elevated temperatures. Leon et al., [37] and Dobbins et al., [38] have shown the reduction of Ti$^{3+}$ to Ti$^0$ after high energy ball milling of NaAlH$_4$ with TiCl$_3$. Another study by Fitchner et al., [28, 144] used titanium nanoclusters that are also shown to improve the thermodynamics comparable to the TiCl$_3$ doped sodium alanates. As outlined in the introduction Chapter, Brinks et al. [145], and Haiduć et al. [141], observed amorphous Ti-Al alloys before the formation of crystalline Al$_3$Ti alloy. Balde et al. [20] also observed amorphous TiAl$_3$ alloys at temperatures below 225°C and crystalline TiAl$_3$ after heat treatment at 425°C. From all the above observations, it is inferred that the formation

of TiAl$_3$ species is evident and stoichiometrically favorable from the atomic compositions of titanium and aluminum in Ti-doped NaAlH$_4$ models. However, the pathways TiAl$_3$ formation or the intermediate phases that result and take part in improved thermodynamics of dehydrogenation are not completely understood.

### 6.1.1 Thermodynamic Pathways

First four reaction paths identified based on above observations studied here are listed in Eqs. (6.1 - 6.4).

$$3NaAlH_4 + TiCl_3 \rightarrow 3NaCl + TiAl_3 + 6H_2 \uparrow \qquad \text{(Eq. 6.1)}$$

$$3NaAlH_4 + TiCl_3 \rightarrow 3NaCl + Ti^0 + 3Al^0 + 6H_2 \uparrow \qquad \text{(Eq. 6.2a)}$$

$$Ti^0 + 3Al^0 \rightarrow TiAl_3 \qquad \text{(Eq. 6.2b)}$$

$$3NaAlH_4 + TiCl_3 \rightarrow 3NaCl + TiAl + 2Al^0 + 6H_2 \uparrow \qquad \text{(Eq. 6.3a)}$$

$$TiAl + 2Al^0 \rightarrow TiAl_3 \qquad \text{(Eq. 6.3b)}$$

$$\frac{9}{2}NaAlH_4 + Ti \rightarrow \frac{3}{2}Na_3AlH_6 + TiAl_3 + \frac{9}{2}H_2 \uparrow \qquad \text{(Eq. 6.4)}$$
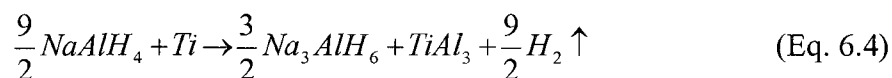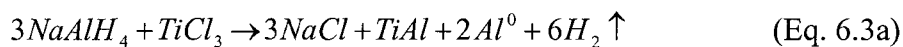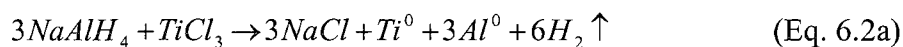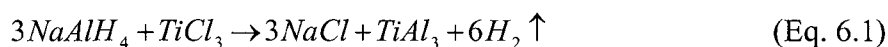
For the formation of the TiAl$_3$ alloy, the source of aluminum is not clearly validated as there are two sources of aluminum present in the doped system: Al in zero oxidation state that results from partial desorption of hydrogen and +3 oxidation state that is present in sodium alanate. Hence in this study, the above four reactions represent the formation of TiAl$_3$ alloy from each source separately in first two reaction paths followed by the combination of both available sources of aluminum in the third. The first reaction path (Reaction Path I) indicates aluminum in +3 oxidation state present in the NaAlH$_4$ reacts with Ti$^0$ forming TiAl$_3$ without any intermediate phases. The second path reports the formation of metallic Ti and Al and titanium reacting with metallic aluminum to form

TiAl$_3$. Reaction Path III suggests the formation of TiAl when Ti reacts with Al present in NaAlH$_4$ along with metallic aluminum and TiAl further reacts with metallic Al resulting in TiAl$_3$. The fourth reaction path evaluates the formation of sodium aluminum hexahydride phase and TiAl$_3$ when the reactants used are metallic titanium and sodium aluminum hydride. This reaction finds the probability when Ti nanoparticles are used as doping agents in place of TiCl$_3$. Recent XPEEM studies by Dobbins et al., [146] reported Al in +3 oxidation state in the vicinity of Ti$^0$ regions after ball milling for five minutes that most likely represents an alane hydride phase rather than a metallic aluminum phase. Hence, besides the above reaction paths, two other routes, based on reported observations from our collaborators [146] and our previous paper on Ti-Al-H dynamics, [142] are also possible. Those include aluminum hydride and TiAl compounds that precede formation of TiAl$_3$. The fifth (Eq. (6.5)), and the sixth (Eq. (6.6)) proposed reaction paths are listed below:

$$NaAlH_4 + TiCl_3 \rightarrow 3NaCl + Ti^0 + 3AlH_3 + \tfrac{3}{2}H_2 \uparrow \qquad \text{(Eq. 6.5a)}$$

$$Ti^0 + 3AlH_3 \rightarrow TiAl_3 + \tfrac{9}{2}H_2 \uparrow \qquad \text{(Eq. 6.5b)}$$

$$NaAlH_4 + TiCl_3 \rightarrow 3NaCl + Ti^0 + 3AlH_3 + \tfrac{3}{2}H_2 \uparrow \qquad \text{(Eq. 6.6a)}$$

$$Ti^0 + AlH_3 \rightarrow TiAl + \tfrac{3}{2}H_2 \uparrow \qquad \text{(Eq. 6.6b)}$$

$$TiAl + 2AlH_3 \rightarrow TiAl_3 + 3H_2 \uparrow \qquad \text{(Eq. 6.6c)}$$
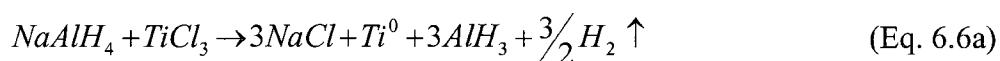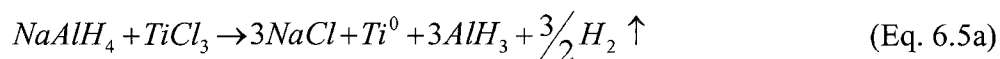
From all the possibilities explained through the listed reactions, the task that now remains is suggesting the most favorable thermodynamic path for hydrogen desorption in Ti-doped sodium alanates.

## 6.1.2 **Enthalpies of Reactions**

Initial structures of all the compounds are imported from ICSD database [121] and are reoptimized to obtain the unit cells with optimum geometry. The phonon DOS is evaluated using the methods explained in Chapter 2, Section 2.2.5, using the optimized configurations of the compounds. The vibrational contributions to the free energy are then derived from phonon DOS. The enthalpies of reactions at 303 K (25°C) evaluated from our calculations are compared across the reactions to find the most favorable reaction path. The enthalpy of each compound is calculated by adding the vibrational, translational and rotational contributions to the sum of its electronic and zero-point energies. The enthalpy of the reaction is calculated by taking the difference between the sum of enthalpies of products and sum of enthalpies of reactants. All the calculated values are listed in Table 6.1.

Table 6.1 Enthalpies of reaction pathways at 303 K studied here. All the energies are in kJ/mol $H_2$.

| Reaction Pathways | $1^{st}$ Step | $2^{nd}$ Step | $3^{rd}$ Step | Total |
|---|---|---|---|---|
| I | -59 | - | - | -59 |
| II | -29 | -179 | - | -208 |
| III | -46 | -77 | - | -123 |
| IV | -3 | - | - | -3 |
| V | -123 | -37 | | -160 |
| VI | -123 | -66 | -23 | -212 |

From the calculated values of the enthalpies of reactions, the products are favored in all the cases. Based on the values from Table 2, the reaction path VI is the most favorable among all the reaction paths proposed. This reaction path predicts aluminum hydride and TiAl intermediates and indicates the source for aluminum is the aluminum present in +3 oxidation state in $AlH_4$ groups of sodium alanate. However, this reaction

path is only 4 kJ/molH$_2$ greater than the reaction path II, that predicts TiAl$_3$ from metallic aluminum and titanium intermediates (observed by Gross et al. [30] and Weidenthaler et al. [143]). The reaction path II indicates the source of Al for the formation of Al$_3$Ti alloy is from the metallic Al that is formed after partial desorption of hydrogen rather than aluminum in sodium alanate. Among the other reaction paths, reaction path I predicting Ti$^0$ reacting with Al$^{3+}$ present in sodium alanate forming TiAl$_3$ directly without any intermediate phases is less favorable by 153 kJ/molH$_2$ compared to the reaction path VI. The reaction paths III and V are less favorable by 89 kJ/molH$_2$ and 52 kJ/molH$_2$, respectively, compared to reaction path VI. The reaction path IV is the least favorable one in which products is favored by 3 kJ/molH$_2$.

Limitations in available methodologies in evaluating all the values (vibrational, translational, rotational, and zero-point energies) that are needed to compute the enthalpy of reaction may induce some errors in the calculations. A clear estimate of errors cannot be made here as the experimental values are not available for the reactions proposed in this paper. A comparison is made between the calculated enthalpy of reaction in reaction path IV with the experimental observation (6 kJ/molH$_2$) by Dobbins et al., [146] which resulted in a mean unsigned error of 3 kJ/molH$_2$. Besides this observation, calculated enthalpies of formation of TiAl$_3$ from metallic Al and Ti species is also compared with the experimental value of -146 kJ/mol, [147] which resulted in a mean unsigned error equal to 33 kJ/mol. Our calculations over predict the formation enthalpy of TiAl$_3$ from the metallic Ti and Al phases. The difference between the most favorable path (reaction path VI) and the second reaction path is less than the possible error in our calculations. Hence, evaluating the most favorable path only from enthalpies of reactions is not

sufficient and calls for further investigation. The next step in this paper is to include entropic contributions and look at the Gibbs free energies of reactions to decide the most probable reaction path.

### 6.1.3 Gibbs Free Energies of Reactions

Free energies of the reactions are calculated by subtracting the temperature dependent entropies from the calculated enthalpies of the reactions. After including entropies, and calculating free energies (listed in Table3), reaction path VI is found to be the most favorable reaction path where the products are favored by 315 kJ/molH$_2$. Competing reaction path II is less favorable by 78 kJ/molH$_2$ than reaction path VI. Reaction path V that predicts the intermediate aluminum hydride species but no TiAl intermediate now falls nearer to reaction path II with a difference in free energy values of 4 kJ/molH$_2$. In spite of the error in our calculations, reaction path VI holds out among all the proposed reaction paths where the products are favored by 315 kJ/molH$_2$.

Table 6.2 Free energies of Reaction pathways at 303 K. All the energies are in kJ/mol H$_2$.

| Reaction Pathways | 1$^{st}$ Step | 2$^{nd}$ Step | 3$^{rd}$ Step | Total |
|---|---|---|---|---|
| I | -92 | – | - | -92 |
| II | -62 | -175 | - | -237 |
| III | -80 | -71 | - | -151 |
| IV | -38 | - | - | -38 |
| V | -166 | -67 | - | -233 |
| VI | -166 | -97 | -52 | -315 |

In an attempt to reduce the error in our calculations, in all metal reactions, such as $Ti^0 + 3Al^0 \rightarrow TiAl_3$ and $TiAl + 2Al^0 \rightarrow TiAl_3$ enthalpies of the reactions are calculated using finite difference/supercell method only as explained in Chapter 2. To validate this approach, the formation enthalpy of TiAl$_3$ is compared with reported experimental

information. Calculated value of -145 kJ/mol differs by one kJ/mol from the experimental reported value. Recalculating using new enthalpy of formation of $TiAl_3$, the enthalpies of reaction paths II and III are -174 kJ/molH$_2$ and -119 kJ/molH$_2$, and the free energies are -207 kJ/molH$_2$ and -147 kJ/molH$_2$ respectively. From the corrected values of enthalpies and free energies of the reactions, reaction path VI is the most favorable one among all the proposed thermodynamic pathways in Ti-doped sodium alanates. Total reaction proceeds through in three steps with aluminum hydrides as intermediates in the first, TiAl in the second and finally $TiAl_3$ in the third reaction.

### 6.1.4 Observations and Summary

In case of Ti-doped sodium alanates, we investigated various thermodynamic pathways to answer the long standing questions related to various resulting phases from doping $NaAlH_4$ with $TiCl_3$. Formation of $TiAl_3$ is stoichiometrically possible from the composition of titanium and aluminum present in $TiCl_3$-doped sodium alanate. However, two of the longstanding questions are (i) the favorable thermodynamic pathway for $TiAl_3$ formation and (ii) the source of aluminum that corresponds to the formation of this $TiAl_3$ alloy. From the first four reactions studied here, reaction paths I and IV show the formation of $TiAl_3$ without any intermediates. However, it is shown that the formation of metallic aluminum and titanium species further leads to the formation of $TiAl_3$ (Reaction Path II-Eq. (6.2)) is deemed favorable and follows the experimental observations [30, 143]. Though the formation of amorphous TiAl is observed in the experimental observations [141, 145] that precede the formation of $TiAl_3$ alloy, the suggested pathways (Eqs. (6.1)-(6.4)) have not shown that the possibility of the reaction path III (Eq. (6.3)) is favored over the reaction path II (Eq. (6.2)). Recent XPEEM studies show that aluminum is present as $Al^{3+}$ around metallic titanium after five minutes ball milling, which

suggested two other possible reaction pathways V (Eq. (6.5)) and VI (Eq. (6.6)). Further investigation in this Chapter based on enthalpy and free energy of the reactions revealed that the reaction pathway VI is the most favorable among all the possible reactions. These observations answer the two questions by illustrating a three step reaction pathway to the formation of $TiAl_3$ (Ti and $AlH_3$ after the first reaction, TiAl after the second, and finally in $TiAl_3$ after the third), and aluminum in its +3 oxidation state present in aluminum hydride species is responsible in the formation of Ti-Al alloys.

## 6.2 Kinetics of Ti-doped Sodium Alanates

Molecular dynamics calculations of pristine and Ti-doped models are done as implemented in the module CASTEP [148] in the Materials Studio® software by Accelrys, Inc [136]. Electronic parameters are consistent with the geometry optimization parameters using plane-wave DFT methods. Time step used is 2fs and equilibration runs using canonical ensemble are set for 2 ps followed by production runs for 2 ps using the micro-canonical ensemble.

Understanding the role of dopants requires predicting the presence of dopants in the $NaAlH_4$ lattice immediately after doping and at elevated temperatures since the decomposition reactions are endothermic and require elevated temperatures for reaction progress. Besides the position of dopants, intermediate compounds that result from doping leading to final phases observed after hydrogen desorption should also be identified. Suitable positions for titanium dopants in sodium alanate lattice are chosen and are investigated to obtain the most probable configurations of Ti-doped sodium alanates. Furthermore, intermediate compounds related to interaction between Ti dopants and $AlH_4$ groups resulting in Ti-Al-H compounds are also detailed and reported in our

previous paper [142] related to structure and dynamics of Ti-Al-H compounds in Ti-doped sodium alanates. In this Chapter, the identified most probable configurations of Ti-doped sodium alanates are taken and analyzed for role of titanium dopants in facilitating the rate limiting step of hydrogen evolution from $NaAlH_4$ lattice. Results based on optimization and DFT coupled molecular dynamics of two layered slabs are reported in Chapter 5 [142]. Similar calculations are extended in this study using four layered slabs with top two layers indicating surface and subsurface layers and bottom two layers indicating bulk of $NaAlH_4$ lattice. Figures 6.1(a) and 6.1(b) show the optimized configurations of Ti dopant placed on top of the interstitial site between to $AlH_4$ units and two Na ions and Ti dopant replacing sodium lattice site on the surface. In both the cases, the identified $TiAl_xH_y$ compounds are similar to the ones that are observed in the two layered slab models reported in previous Chapter. Values of 'x' and 'y' depend on the accessible $AlH_4$ groups around the Ti dopant.

**(a)**                                    **(b)**
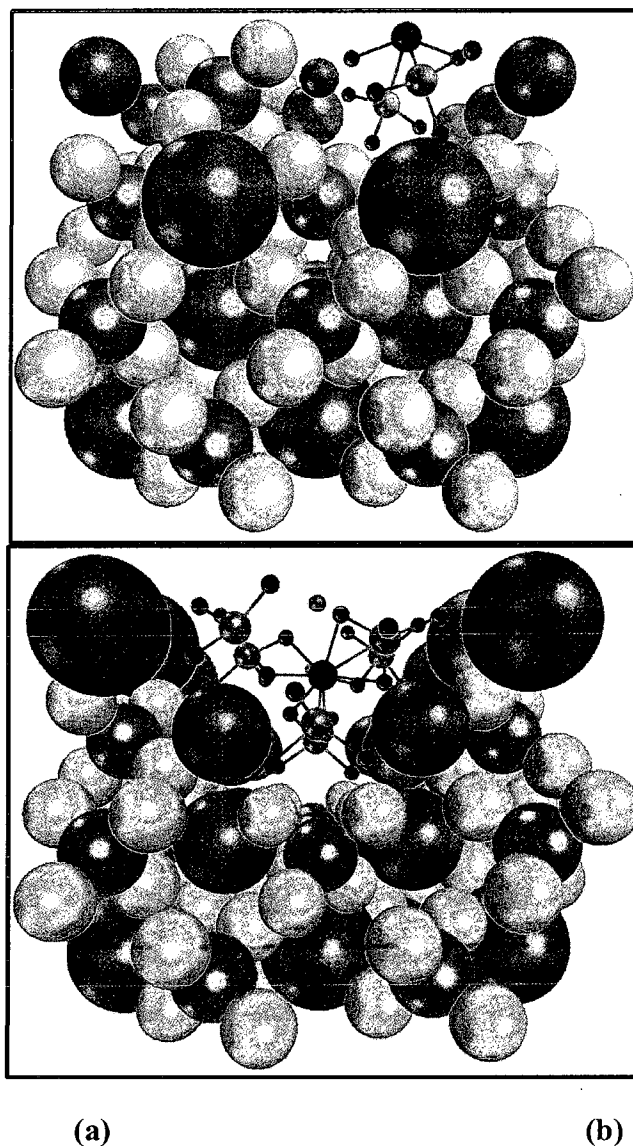
Figure 6.1 Models representing optimized configurations of (a) Ti dopants placed on top
of interstitial site and (b) Ti dopants replacing Na lattice site on the surface.
$AlH_4$ groups and Na ions are shown as balls. Colors in the figure indicate
magenta-aluminum, grey-hydrogen, and purple-sodium. $AlH_4$ groups involved
in reactions are represented in ball and stick model (magenta-aluminum, blue-
titanium, and red-hydrogen).

### 6.2.1 Optimization and Dynamics

From the optimized configurations we can see that the hydrogens that are

previously bonded to only aluminum are now shared between titanium and aluminum

along with aluminums attached to the titanium dopants. In case of titanium on top of

interstitial site Ti is seen forming bonds with two hydrogens from accessible $AlH_4$ groups and in case of Ti replacing sodium lattice site Ti is seen forming bonds with six hydrogens from surrounding $AlH_4$ groups. These configurations can be compared to the ball milled samples of Ti-doped $NaAlH_4$. After optimization of Ti-doped sodium alanates, some of the hydrogens that are seen associated with both titanium and aluminum are detached completely from aluminum exhibiting only bonds with titanium. Reported theoretical studies by Liu and Ge [44], have also shown that the energy to remove hydrogens that are bound to titanium is less compared to the energy required to remove hydrogens that are attached to aluminum in $AlH_4$ groups. This predicts the role of titanium in facilitating the breaking of hydrogens that are covalently bound to the aluminum in $AlH_4$ groups.

Next step is to study the stability and dynamics of the formed intermediates at elevated temperatures. In this study, DFT coupled with MD is used to study the dynamics at 423 K (150°C) of both pristine and Ti-doped sodium alanates. Optimized models from DFT calculations are taken, and molecular dynamics calculations are run for 2 ps in canonical ensemble (constant number of molecules, constant volume, and constant temperature) to equilibrate the structure at 423 K. Following equilibration, another molecular dynamics calculation is run for 2 ps in micro-canonical ensemble (constant number of molecules, constant volume, and constant energy) to observe the behavior of atomic/molecular species at the elevated temperature of 423 K. In the MD calculations, after each MD step electron density is minimized, and the forces between the atoms are calculated using DFT. MD simulations run for a very long time (seconds time scale), ideally, should reproduce the proposed reaction paths, and the phase separations as seen

in experiments. Our simulations span for a very short time (4-5 ps) and predict the precursors to the actual reaction path and the reaction mechanisms are predicted based on our results from MD simulations.

From MD simulations of pristine sodium alanates, reorientation and diffusion of $AlH_4$ groups are seen in the lattice. No sites for aluminum nucleation or breaking of bonds from $AlH_4$ groups are observed. Diffusion of all the groups in four layers of the slab is random in three dimensions representing natural diffusion in lattice. This diffusion indicates the kinetics of transitions from $AlH_4^-$ to $AlH_5^{2-}$, and $AlH_5^{2-}$ to $AlH_6^{3-}$ are not happening at the pico/nano second scale that complements reported slow kinetics of hydrogen desorption in pristine sodium alanates. However, improvement in kinetics is observed in Ti-catalyzed sodium alanates. MD simulations of Ti-doped sodium alanates have shown the formed Ti-Al-H compounds after optimization are still in existence at elevated temperatures. Increased numbers of aluminum are seen associating with titanium, indicating a probable site for nucleation of the aluminum phase. Increased numbers of hydrogens from the surrounding groups are also seen associated with titanium with time and temperature. In both Ti-doped models, titanium is not seen diffusing into the lattice which eliminates the possibility of bulk doping of titanium in $NaAlH_4$ lattice. In the case of Ti replacing the Na lattice site model, the $AlH_4$ groups in the top two layers are seen diffusing towards titanium forming hybrid complexes of Ti-Al-H compounds whereas the movement of $AlH_4$ groups in bottom two layers indicate natural diffusion in lattice. Hydrogens that are previously bonded to aluminum are now transferred to titanium in the complex exhibiting no bonding character with aluminum. In the case of titanium on top of the interstitial site, hydrogens from $AlH_4$ groups in subsurface layer

are seen hopping to attach to aluminums that are attached to titanium. This mechanism can be termed as reorientation and hopping rather than diffusion of hydrogen species in the lattice. The hydrogens that are hopped from $AlH_4$ groups in subsurface layer are expected to transfer to titanium thereby detaching from aluminum and forming molecular hydrogen.

## 6.2.2 Observations and Summary

Role of Ti dopants thus can be explained from our DFT/DFT-MD calculations. From our simulations, we see that the titanium dopants are present on the surface during the whole simulation time and exhibit the role in catalytic splitting of hydrogen from surrounding $AlH_4$ groups. Ti dopants draw the hydrogens from accessible $AlH_4$ groups, and the newly formed bonds between Ti and H are easily broken compared to Al-H bonds in $AlH_4$ or $AlH_3$ groups. This role of Ti explains the lowered kinetic barrier for evolution of hydrogen from $AlH_4$ or $AlH_3$ species in Ti-doped sodium alanates compared to pristine compounds. Besides the catalytic role, Ti dopants also form bonds with Al, and we also see that the $AlH_4$ groups on the surface and that are present in the sub-surface layers are drawn towards the Ti dopants. This action indicates the initiation of Al nucleation site facilitated by Ti dopants.

# CHAPTER 7

# CONCLUSIONS AND FUTURE WORK

## 7.1 Conclusions

First principles calculations are successfully applied in this dissertation study to study the structure, thermodynamics, and kinetics of pristine and Ti-doped sodium alanates. This study is believed to address the longstanding questions laid out in the area of realizing materials based onboard hydrogen storage.

- Structural, electronic and vibrational properties of pristine $NaAlH_4$.

    o Optimized lattice parameters agree well with the reported experimental information. Calculated bondlengths between Al-H atoms in $AlH_4$ complexes (1.638 Å) and Na ions and $AlH_4$ complexes (3.535 Å), compare well with the reported bond lengths of 1.63 Å and 3.52 Å [22]. $AlH_4$ tetrahedra are slightly distorted with two sets of H-Al-H angles of 107.5° and 113.4°.

    o Based on the difference between the electronic energies of valence bands and conduction bands at the $\Gamma$ point shown in band structure plot, the bandgap in $NaAlH_4$ is estimated to be equal to 4.8 eV that matches exactly with the reported bandgap of $NaAlH_4$ [22].

The DOS in the valence band indicate the covalent bond structure due to hybridized sp orbitals from s of hydrogen and p of aluminum. The conduction band is occupied with *s* and *p* states of sodium and aluminum. No contribution from outer s orbitals of Na is seen in valence band indicating the non-covalent interactions between Na and $AlH_4$ groups. Both the bands are separated by a bandgap nearly equal to 4.8 eV indicating the insulating behavior of sodium alanate.

o From electron density maps, a smeared electron density cloud is seen in the $AlH_4$ group between Al and H atoms indicating existence of covalent bonds between Al and H atoms in $AlH_4$ group. Minimum or no electron density is seen between Na ions and $AlH_4$ groups, indicating no bond formed by sharing electrons between two groups. From the electron density maps of $NaAlH_4$, it can be deduced that covalent bonding exists between Al and H atoms in $AlH_4$ groups and Na ions are electrostatically bound (ionic bonding) to $AlH_4$ groups and stabilize the lattice.

o Analyzing the Mülliken bond population in $AlH_4$ groups, high bond population is found between Al-H bonds. This high bond population indicates that the bonding in the $AlH_4$ tetrahedral complexes is covalent. Bond population value between Na and H is less than zero, indicating that the bond is non-covalent. The effective charge on Na (+1.33e) and the sum of effective charges in $AlH_4$ group (-1.32e) shows the existence of ionic bonds between Na atoms and $AlH_4$ groups in the $NaAlH_4$ unit cell. Charge distribution obtained from born effective charge tensors also show an

existence of ionic interactions between Na ions and H ions in $AlH_4$ groups with charge concentrated around H ions in $AlH_4$ groups.

o From the analysis of vibrational frequencies in the calculated structures of $NaAlH_4$, normal modes in the IR spectrum corresponding to the Al-H symmetric stretching in the $AlH_4$ tetrahedra are found to be $1808cm^{-1}$ and asymmetric stretching modes at 1737 and $1704cm^{-1}$. Three peaks related to IR active modes at 867, 835 and $705cm^{-1}$ that correspond to the Al-H bending region at $\Gamma$ point along the three high symmetry directions Z ( 0.5, 0.5, -0.5); X (0.0, 0.0, 0.5); and N (0.0, 0.5, 0.0); and one IR active mode at $750cm^{-1}$ along X and $601cm^{-1}$ along N are found in the phonon DOS spectrum.

o Calculated thermodynamic functions such as change in enthalpy, entropy, and free energy as a function of temperature in the temperature range of zero to 300 K agree well with the experimental values validating our calculations. However, beyond 450 K the curves may be unreliable as the melting point for $NaAlH_4$ is noted as 453 K and harmonic approximation of phonons is no longer valid.

- Possible sites for titanium dopants in $NaAlH_4$ lattice.

Six possible configurations of modified $NaAlH_4$ are studied to get insights into the most probable sites for Ti dopants in $NaAlH_4$.

o Optimized lattice models representing a vacancy at this Na bulk site $(0 \rightarrow B_{Na})$ and Ti in $B_{Na}$ site $(Ti \rightarrow B_{Na})$ both preserve the lattice structure of $NaAlH_4$ with changes in lattice parameters and bond lengths between Al

and H as well as Na and Al in the neighboring groups around the vacancy ($0 \rightarrow B_{Na}$) or Ti dopant (Ti$\rightarrow B_{Na}$).

o All the structural differences found mainly when Ti$\rightarrow B_{Na}$ can be attributed to the difference in atomic radii of sodium (1.86 Å) and titanium (1.47 Å) atoms. The presence of titanium dopants replacing the native sodium sites $B_{Na}$ results in a decrease of the lattice parameters, and shows changes in the distances between sodium and hydrogen as well as aluminum and hydrogen. Elongation and therefore weakening of the Al-H bond in the presence of a Ti at $B_{Na}$ is observed.

o Four different models are constructed to investigate the possible sites for Ti dopants on the (001) surface and on top of the (001) surface. Hence, the four models considered are Ti$\rightarrow S_{Na}$ (Ti-substituted Na at $S_{Na}$), Ti$\rightarrow S_I$ (Ti added to the interstitial surface $S_I$ site), Ti$\rightarrow T_{Na}$ (Ti placed on-top the surface $S_{Na}$ site), and Ti$\rightarrow T_I$ (Ti placed on-top the surface interstitial $S_I$ site).

o From the cohesive energy calculations, it is seen that Ti$\rightarrow B_{Na}$ is 1.88 eV and is more stable than the pristine NaAlH$_4$, and the latter is 6.85 eV more stable than the case in which a vacancy is created at $B_{Na}$ ($0 \rightarrow B_{Na}$). The cohesive energies of models Ti$\rightarrow S_{Na}$, Ti$\rightarrow S_I$, Ti$\rightarrow T_{Na}$, and Ti$\rightarrow T_I$ are higher than the corresponding pristine NaAlH$_4$ surface model, and therefore possible.

o Substitution energy for the Ti→S$_{Na}$ model and titanium-addition energies for the Ti→S$_I$, Ti→T$_{Na}$ and Ti→T$_I$ models show that the energy required for such substitution/addition is Ti→S$_{Na}$ ≈ Ti→T$_I$ < Ti→T$_{Na}$ < Ti→S$_I$.

o The difference between the energy required for Ti→S$_{Na}$ and Ti→T$_I$ is 0.003 eV atom$^{-1}$, while the energy required for Ti→S$_I$ is substantially higher than the corresponding one in the other three cases. Since the energy required for Ti→S$_{Na}$ and Ti→T$_I$ is less when compared to others, these two sites (S$_{Na}$ and T$_I$) would be preferred by the Ti dopants.

- Possible compounds resulting from titanium doping in sodium alanates.

  o The Ti dopant in Ti→S$_{Na}$ model, settles between the surface and sub-surface layers forming bonds with hydrogen and aluminum atoms in surrounding accessible AlH$_4$ groups. From the Ti local environment in the Ti→S$_{Na}$ model it is observed that the Ti atom coordinates to seven H atoms at distances in the 1.81-1.97 Å range, and two aluminum atoms at distances in the 2.6-2.7 Å range. Since typical Ti-Al and Ti-H bond lengths in TiAl and TiH compounds such as TiAl$_3$ and TiH$_2$ are in the 2.7-2.9 Å [139], and in the order of 1.92 Å [140] respectively, the possible formation of a Ti-Al-H complex (TiAl$_2$H$_7$) is predicted in our calculations.

  o In Ti→S$_{Na}$ model, Ti is coordinated to two aluminum and seven hydrogen atoms resulting in the possible formation of a TiAl$_2$H$_7$ complex. Since the individual Al-H bond lengths increase with respect to the bonds in the pristine lattice and it is seen that the Al-H bond lengths in the AlH$_4$ groups

are weakened (by 0.03 to 0.20 Å) suggesting the possible formation of a TiAl$_2$H$_7$ complex.

○ In the case of Ti→T$_I$, Ti is coordinated to two aluminum and two hydrogen atoms resulting in the possible formation of a TiAl$_2$H$_2$ complex. The individual Al-H bond lengths increase with respect to the bonds in the pristine lattice and it is seen that the Al-H bond lengths in the AlH$_4$ groups are weakened (by 0.20 Å) suggesting the possible formation of a TiAl$_2$H$_2$ complex.

○ The complex observed in Ti→T$_I$ model is a precursor to the complexes observed in Ti→S$_I$ and Ti→T$_{Na}$ models when subjected to elevated temperatures.

• Dynamics of the formed Ti-Al-H compounds at elevated temperatures.

○ From the results of DFT-MD simulations of Ti→S$_{Na}$ and Ti→T$_I$ models at 423 K and 448 K, it is noticed that the Ti dopant settles between surface and subsurface layers and no further diffusion into the lattice is observed.

○ In Ti→S$_{Na}$ model at elevated temperatures, the number of aluminum atoms coordinating with titanium in the complex increases from two (at distances in the 2.6-2.7 Å range) to five (at distances in the 2.6-2.7 Å range). Besides the formation of a Ti-Al-H complex, Al-Al association (with a 2.97 Å bond length) is also seen from the DFT-MD results. When temperature is increased from 423 to 448 K, no significant changes in the TiAl$_5$H$_7$ complex is seen over time. Rearrangement of Al and H atoms in

this complex is, however, observed, but the number of hydrogen and aluminum atoms associated with the complex remains the same.

o From the dynamics of the Ti-Al-H complexes over time and at different temperatures in case of Ti→$T_I$, it is seen that the $TiAl_2H_2$ complex becomes $TiAl_3H_6$ (three aluminums and six hydrogens with positive bond population) at 423 K and $TiAl_3H_7$ (three aluminums and seven hydrogens with positive bond population) at 448 K.

o The complex in the case of Ti→$S_{Na}$ model seems like a precursor to the phase with atomic Ti dispersed in aluminum. The complex observed in case of Ti→$T_I$ model seems like a precursor to the $TiAl_3$ phase since association of Ti with three Al atoms is seen with formed Ti-Al bonds.

- Identify the thermodynamic pathways for hydrogen desorption in pristine $NaAlH_4$ and formation of Ti-Al alloys in Ti-doped $NaAlH_4$.

o Temperature of the desorption reaction predicted from Gibbs free energy of reactions predict a temperature of 306 K for the first decomposition reaction (Eq. (1.1)) and the enthalpy of the reaction is positive (~37 kJ/mol) over the range of temperatures form 0-600 K indicating it as an endothermic reaction.

o In the 300-400 K range, calculated entropy of gaseous hydrogen from our DFT calculations is between 136-144 J $mol^{-1}$ $K^{-1}$, and the entropy change in the reaction is equal to 120-123 J $mol^{-1}$ $K^{-1}$. Hence the total entropy change in the reaction is equal to the entropy change due to transformation

of hydrogen from condensed to gas phase and the contribution from solids is negligible.

o In second reaction (Eq.(1.2)), predicted values of reaction temperature and enthalpy of the reaction are 413 K and 23 kJ/mol respectively compared to experimental values of 423 K and 16 kJ/mol. The discrepancies in calculated values at higher temperatures are due to the anharmonicity introduced in the vibrations, which is not very accurately predicted by the harmonic approximation used.

o Six thermodynamic reaction pathways are studied here that show the formation of $TiAl_3$ alloy. From the first four reactions studied here, reaction paths I and IV show the formation of $TiAl_3$ without any intermediates, but it is shown that the formation of metallic aluminum and titanium species that further leads to formation of $TiAl_3$ (Reaction Path II; Eq. (6.2)) is deemed favorable and follows the experimental observations [30, 143].

o Further investigation in this study based on enthalpy and free energy of the reactions, reaction pathway VI predicting aluminum hydride, and TiAl intermediates is the most favorable among all the possible reactions.

o Observations in this study answer the two questions by illustrating a three step reaction pathway to the formation of $TiAl_3$ (Ti and $AlH_3$ after the first reaction, TiAl after the second and finally $TiAl_3$ in the third) and aluminum in its +3 oxidation state present in aluminum hydride species is responsible in the formation of Ti-Al alloys.

- Understand the kinetics of hydrogen desorption in pristine $NaAlH_4$ and elucidate the role of Ti dopants in improved kinetics of Ti-doped $NaAlH_4$.

  o In this dissertation, studied kinetic reaction paths leading to gaseous hydrogen in pristine $NaAlH_4$ revealed a three step reaction for transition from $AlH_4^-$ anion to $AlH_6^{3-}$ anion that completes first of the two proposed hydrogen desorption reactions in sodium alanates.

  o From the proposed mechanism, rate limiting step determined is associated with hydrogen evolution from association of $AlH_3$ species nucleating aluminum phase. This step is 15 kJ/mol higher than the nearest highest barrier in the reaction path related to transition from $AlH_5^{2-}$ to $AlH_6^{3-}$.

  o Role of Ti dopants is explained from our DFT/DFT-MD calculations. From our simulations, we see that the titanium dopants are present on the surface the whole simulation time and exhibit the role in catalytic splitting of hydrogen from surrounding $AlH_4$ groups.

  o Ti dopants draw the hydrogens from accessible $AlH_4$ groups, and the newly formed bonds between Ti and H are easily broken compared to Al-H bonds in $AlH_4$ or $AlH_3$ groups. This role of Ti explains the lowered kinetic barrier for evolution of hydrogen from $AlH_4$ or $AlH_3$ species in Ti-doped sodium alanates compared to pristine compounds.

  o Besides the catalytic role, Ti dopants also form bonds with Al, and we also see that the $AlH_4$ groups on the surface and that are present in the sub-surface layers are drawn towards the Ti dopants. This phenomenon indicates the initiation of Al nucleation site facilitated by Ti dopants.

## 7.2 Suggested Future Work

The targets set by the US DoE include the development of onboard storage materials by 2015 that have gravimetric and volumetric densities greater than system level targets of 7.5 wt% of hydrogen and 0.070 kg-$H_2$/L. In order to achieve the targets set by DoE many light weight materials are currently under research [7]. Of all the materials, ammonia borane ($NH_3BH_3$) is particularly attractive, and the recent surge in research on using boranes based hydrogen storage is due to the achievable gravimetric and volumetric storage densities up to 20% and 0.16 kg-$H_2$/L upon complete dissociation of ammonia borane. Decomposition of ammonia boranes is proposed through a three step reaction forming polyaminoborane ($NH_2BH_2$)$_n$, and polyiminoborane (NHBH)$_n$ as intermediates and finally resulting in boron nitride. However, kinetics and reversibility, and thermodynamics of second and third reactions, are the issues associated with ammonia boranes [149].

Computational techniques used in this study can be applied towards the study of kinetic and thermodynamic mechanisms of catalyst modified ammonia boranes. Improved thermodynamics and kinetics of hydrogen desorption are observed by using $Ni_{1-x}Pt_x$ catalysts and Si nano scaffolds. Figure 7.1 shows the two forms of crystal structure reported at room temperature and at 200 K. At room temperature, $NH_3BH_3$ exhibits tetragonal crystal structure, and at low temperatures it exhibits low symmetry orthorhombic crystal structure. For many years, positions of hydrogen atoms in tetragonal crystal structure could not be identified. Recent work by Bowden et al., [150] have shown that hydrogen exists as a halo around the nitrogen and boron atoms visiting all the symmetric Wyckoff sites around those atoms in a tetragonal structure. The tetragonal

structure shown in Figure 7.1 is built based on the crystallographic information provided by Bowden et al., [150].
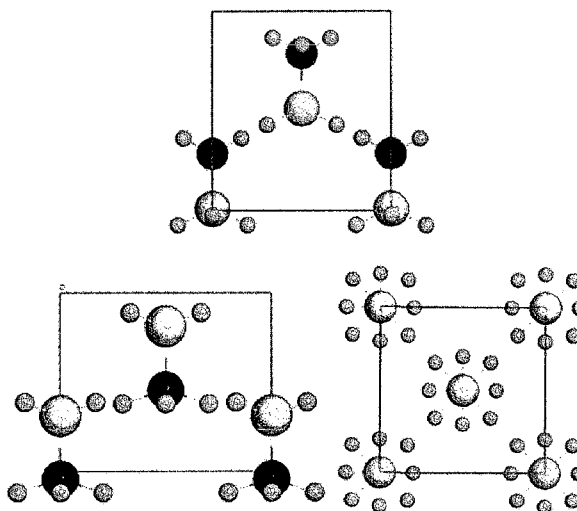


Figure 7.1 Orthorhombic (~200 K) and tetragonal (~298 K) structures of ammonia borane.

Computationally, representing the tetragonal lattice structure is difficult. CASTEP through Materials Studio® offers the technique of specifying the occupancy factor for each atom at a particular site. Specifying an occupancy factor of 0.75 will distribute the three fold symmetric hydrogens around the nitrogen or boron to exist in a fourfold symmetric axis in tetragonal structure. Table 7.1 shows the calculated and reported lattice parameters for ammonia borane.

Table 7.1 Calculated and reported lattice parameters of ammonia borane.

| Method | Lattice type | a(Å) | b(Å) | c(Å) |
|---|---|---|---|---|
| Expt at 200 K [151] | Orthorhombic | 5.395 | 4.886 | 4.986 |
| Calc (DFT) | Orthorhombic | 5.152 | 5.004 | 5.644 |
| Calc (DFT) [152] | Orthorhombic | 5.302 | 4.939 | 5.172 |
| Expt at 298 K [153] | Tetragonal | 5.255 | 5.255 | 5.048 |
| Expt at 298 K [150] | Tetragonal | 5.263 | 5.263 | 5.050 |
| Calc (DFT) | Tetragonal | 5.337 | 5.337 | 4.471 |

Cheng et al., [154] reported the dopants such as Ni-Pt clusters ($Ni_{1-x}Pt_x$ where x = 0, 0.03, 0.06, 0.09, and 0.12) have shown improvement in hydrogen desorption kinetics when hydrolyzed and improvement in thermodynamics when subjected to thermal treatment. Ni-Pt clusters are formed by incorporating Pt in Ni (FCC) structure. Platinum does not change structure of Ni but replaces one of the nickel atoms and Pt and Ni atoms are distributed homogeneously with Pt randomly at the Ni position. Figure 7.2 shows the various forms of dopant clusters that could be used in studying quantum mechanical and molecular dynamics calculations. Tetragonal arrangement in both cases (Ni and Ni-Pt) is energetically more favorable than the rhombohedral arrangement of atoms.
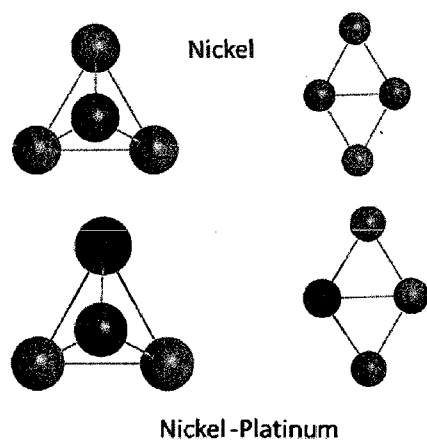
Figure 7.2 Tetragonal arrangements of 4 atom clusters of Ni and Ni₃Pt.

# REFERENCES

[1]    "Hydrogen Posture Plan," 2005. [Online]. Available: www.doe.gov. [Accessed: Mar1, 2009]

[2]    C.W.Forsberg, "The Hydrogen Economy is Coming The Question is Where?" *CEP*, Dec. 2005, pp.20-22.

[3]    S. Satyapal, J. Petrovic, C. Read, G. Thomas, and G. Ordaz, "The U.S. Department of Energy's National Hydrogen Storage Project: Progress towards meeting hydrogen-powered vehicle requirements," *Catalysis Today*, vol. 120, pp. 246-256, 2007.

[4]    E. David, "An Overview of Advanced Materials for Hydrogen Storage," *Journal of Materials Processing Technology*, vol. 162-163, pp. 169-177, 2005.

[5]    M.Jacoby, "Filling Up With Hydrogen," *C&EN*, Jun. 2005, pp. 42-47.

[6]    D. Ross, "Hydrogen Storage: The Major Technological Barrier to the Development of Hydrogen Fuel Cell Cars," *Vacuum*, vol. 80, pp. 1084-1089, 2006.

[7]    "2008 Progress Report for the DOE Hydrogen Program," DoE, 2008. [Online]. Available: www.doe.gov. [Accessed: Mar1, 2009]

[8]    B. Bogdanović and M. Schwickardi, "Ti-doped alkali metal aluminium hydrides as potential novel reversible hydrogen storage materials," *Journal of Alloys and Compounds*, vol. 253, pp. 1-9, 1997.

[9]    K. J. Gross, S. Guthrie, S. Takara, and G. Thomas, "In-situ X-ray diffraction study of the decomposition of $NaAlH_4$," *Journal of Alloys and Compounds*, vol. 297, pp. 270-281, 2000.

[10]   J. J. Reilly and R. H. Wiswall.Jr, "The reaction of hydrogen with alloys of Magnesium and Nickel and the formation of $Mg_2NiH_4$," *Inorganic Chemistry*, vol. 7, pp. 2254-2256, 1968.

[11]   J. J. Reilly and R. H. Wiswall.Jr, "The reaction of hydrogen with alloys of Magnesium and Copper," *Inorganic Chemistry*, vol. 6, pp. 2220-2223, 1967.

[12]     J. J. Vajo, F. Mertens, C. C. Ahn, R. C. Bowman, and B. Fultz, "Altering Hydrogen Storage Properties by Hydride Destabilization through Alloy Formation: LiH and MgH₂ Destabilized with Si," *Journal of Physical Chemistry B*, vol. 108, pp. 13977-13983, 2004.

[13]     B. Bogdanović, M. Felderhoff, S. Kaskel, A. Pommerin, K. Schlichte, and F. Schüth, "Improved Hydrogen Storage Properties of Ti-Doped Sodium Alanate Using Titanium Nanoparticles as Doping Agents," *Advanced Materials*, vol. 15, pp. 1012-1015, 2003.

[14]     B. Bogdanović, R. A. Brand, A. Marjanovi, M. Schwickardi, and J. Tölle, "Metal-doped sodium aluminium hydrides as potential new hydrogen storage materials," *Journal of Alloys and Compounds*, vol. 302, pp. 36-58, 2000.

[15]     C. M. Jensen and K. J. Gross, "Development of catalytically enhanced sodium aluminum hydride as a hydrogen-storage material," *Applied Physics A: Materials Science & Processing*, vol. 72, pp. 213-219, 2001.

[16]     G. Sandrock, K. Gross, and G. Thomas, "Effect of Ti-catalyst Content on the Reversible Hydrogen Storage Properties of the Sodum Alanates," *Journal of Alloys and Compounds*, vol. 339, pp. 299-308, 2002.

[17]     D. L. Anton, "Hydrogen Desorption Kinetics in Transition Metal Modified NaAlH₄," *Journal of Alloys and Compounds*, vol. 356-357, pp. 400-404, 2003.

[18]     D. Sun, T. Kiyobayashi, H. T. Takeshita, N. Kuriyama, and C. M. Jensen, "X-ray diffraction studies of titanium and zirconium doped NaAlH₄: elucidation of doping induced structural changes and their relationship to enhanced hydrogen storage properties," *Journal of Alloys and Compounds*, vol. 337, pp. L8-L11, 2002.

[19]     K. J. Gross, E. H. Majzoub, and S. W. Spangler, "The effects of titanium precursors on hydriding properties of alanates," *Journal of Alloys and Compounds*, vol. 356–357, pp. 423-428, 2003.

[20]     C. P. Baldé, H. A. Stil, A. M. J. vanderEerden, K. P. deJong, and J. H. Bitter, "Active Ti Species in TiCl₃-Doped NaAlH₄. Mechanism for Catalyst Deactivation," *Journal of Physical Chemistry C*, vol. 111, pp. 2797-2802, 2007.

[21]     J. Íñiguez, T. Yildirim, T. J. Udovic, M. Sulic, and C. M. Jensen, "Structure and hydrogen dynamics of pure and Ti-doped sodium alanate," *Physical Review B*, vol. 70, pp. 060101(R), 2004.

[22]     V. Ozolins, E. H. Majzoub, and T. J. Udovic, "Electronic Structure and Rietveld Refinement Parameters of Ti-doped Sodium Alanates," *Journal of Alloys and Compounds*, vol. 375, pp. 1-10, 2004.

[23] E. K. Lee, Y. W. Cho, and J. K. Yoon, "Ab-initio calculations of titanium solubility in NaAlH$_4$ and Na3AlH$_6$," *Journal of Alloys and Compounds*, vol. 416, pp. 245-249, 2006.

[24] T. Kiyobayashi, S. S. Srinivasan, D. Sun, and C. M. Jensen, "Kinetic Study and Determination of the Enthalpies of Activation of the Dehydrogenation of Titanium- and Zirconium-Doped NaAlH4 and Na3AlH6," *Journal of Physical Chemistry A*, vol. 107, pp. 7671-7674, 2003.

[25] M. E. Arroyo y de Dompablo and G. Ceder, "First principles investigations of complex hydrides AMH$_4$ and A$_3$MH$_6$ (A=Li, Na, K, M=B, Al, Ga) as hydrogen storage systems," *Journal of Alloys and Compounds*, vol. 364, pp. 6-12, 2004.

[26] O. M. Løvvik and S. M. Opalka, "Density functional calculations of Ti-enhanced NaAlH$_4$," *Physical Review B*, vol. 71, pp. 054103, 2005.

[27] T. Vegge, "Equilibrium structure and Ti-catalyzed H$_2$ desorption in NaAlH$_4$ nanoparticles from density functional theory," *Physical Chemistry Chemical Physics*, vol. 8, pp. 4853–4861, 2006.

[28] M. Fichtner, P. Canton, O. Kircher, and A. Léon, "Nanocrystalline alanates— Phase transformations, and catalysts," *Journal of Alloys and Compounds*, vol. 404-406, pp. 732-737, 2005.

[29] C. M. Araújo, S. Li, R. Ahuja, and P. Jena, "Vacancy-mediated hydrogen desorption in NaAlH$_4$," *Physical Review B*, vol. 72, pp. 165101-6, 2005.

[30] K. J. Gross, "Catalyzed alanates for Hydrogen Storage," *Journal of Alloys and Compounds*, vol. 330-332, pp. 683-690, 2002.

[31] S. Chaudhuri, J. Graetz, A. Ignatov, J. J. Reilly, and J. T. Muckerman, "Understanding the Role of Ti in Reversible Hydrogen Storage as Sodium Alanate: A Combined Experimental and Density Functional Theoretical Approach," *Journal of American Chemical Society*, vol. 128, pp. 11404-11415, 2006.

[32] S. Chaudhuri and J. T. Muckerman, "First-Principles Study of Ti-Catalyzed Hydrogen Chemisorption on an Al Surface: A Critical First Step for Reversible Hydrogen Storage in NaAlH$_4$," *Journal of Physical Chemistry B*, vol. 109, pp. 6952-6957, 2005.

[33] J. Graetz, A. Y. Ignatov, T. A. Tyson, J. J. Reilly, and J. Johnson, "X-ray absorption study of Ti-activated sodium aluminum hydride," *Journal of Materials Research Society Conference Proceedings*, vol. 837, 2005.

[34]    H. W. Brinks, C. M. Jensen, S. S. Srinivasan, B. C. Hauback, D. Blanchard, and
        K. Murphy, "Synchrotron X-ray and neutron diffraction studies of $NaAlH_4$
        containing Ti additives," *Journal of Alloys and Compounds*, vol. 376, pp. 215-
        221, 2004.

[35]    H. W. Brinks, B. C. Hauback, S. S. Srinivasan, and C. M. Jensen, "Synchrotron
        X-ray Studies of $Al_{1-y}Ti_y$ Formation and Re-hydriding Inhibition in Ti-Enhanced
        $NaAlH_4$," *Journal of Physical Chemistry B*, vol. 109, pp. 15780-15785, 2005.

[36]    A. G. Haiduc, H. A. Stil, M. A. Schwarz, P. Paulus, and J. J. C. Geerlings, "On
        the fate of the Ti catalyst during hydrogen cycling of sodium alanate," *Journal of
        Alloys and Compounds*, vol. 393, pp. 252-263, 2005.

[37]    A. Léon, O. Kircher, J. Rothe, and M. Fichtner, "Chemical State and Local
        Structure around Titanium Atoms in $NaAlH_4$ Doped with $TiCl_3$ Using X-ray
        Absorption Spectroscopy," *Journal of Physical Chemistry B*, vol. 108, pp. 16372-
        16376, 2005.

[38]    T. A. Dobbins, R. Tittsworth, S. A. Speakman, and J. Schneibel, "Synchrotron X-
        ray Absorption Spectroscopy (XAS) for Understanding Dopant Effects in Ti-
        doped NaAlH4," presented at Advanced Materials for Energy Conversion III, A
        Symposium in Honor of Drs. Gary Sandrock, Louis Schlapbach, and Seijirau
        Suda – ed. D. Chandra, J.J. Petrovic, R. Bautista, A. Imam, 2006.

[39]    A. Marashdeh, R. A. Olsen, O. M. Løvvik, and G. Kroes, "$NaAlH_4$ Clusters with
        Two Titanium Atoms Added," *Journal of Physical Chemistry C*, vol. 111, pp.
        8206-8213, 2007.

[40]    Y. W. C. E. K.Lee, J. K. Yoon, "Ab-initio calculations of titanium solubility in
        $NaAlH_4$ and Na3AlH6," *Journal of Alloys and Compounds*, vol. 416, pp. 245-249,
        2006.

[41]    T. J. Frankcombe and O. M. Løvvik, "The crystal structure and surface energy of
        $NaAlH_4$: A comparison of DFT methodologies," *Journal of Physical Chemistry B*,
        vol. 110, pp. 622-630, 2006.

[42]    A. J. Du, S. C. Smith, and G. Q. Lu, "Role of charge in destabilizing AlH4 and
        BH4 complex anions for hydrogen storage applications: Ab initio density
        functional calculations," *Physical Review B*, vol. 74, pp. 1934051-4, 2006.

[43]    S. Li, P. Jena, and R. Ahuja, "Effect of Ti and metal vacancies on the electronic
        structure, stability, and dehydrogenation of $Na_3AlH_6$: Supercell band-structure
        formalism and gradient-corrected density-functional theory," *Physical Review B*,
        vol. 73, pp. 214107, 2006.

[44]    J. Liu and Q. Ge, "A First-Principles Analysis of Hydrogen Interaction in Ti-
        Doped $NaAlH_4$ Surfaces:Structure and Energetics," *Journal of Physical
        Chemistry B*, vol. 110, pp. 25863-25868, 2006.

[45] J. M. Bellosta von Colbe, W. Schmidt, M. Felderhoff, B. Bogdanovic´, and F. Schu¨th, "Hydrogen-Isotope Scrambling on Doped Sodium Alanate," *Angewandte Chemie International Edition*, vol. 45, pp. 3663 –3665, 2006.

[46] W. Lohstroh and M. Fichtner, "Rate limiting steps of the phase transformations in Ti-doped NaAlH4 investigated by isotope exchange," *Physical Review B*, vol. 75, pp. 184106, 2007.

[47] H. Gunaydin, K. N. Houk, and V. Ozolins, "Vacancy-mediated dehydrogenation of sodium alanate," *Proceedings of the National Academy of Sciences of the United States of America*, vol. 105, pp. 3673-3677, 2008.

[48] R. T. Walters and J. H. Scogin, "A reversible hydrogen storage mechanism for sodium alanate: the role of alanes and the catalytic effect of the dopant," *Journal of Alloys and Compounds*, vol. 379, pp. 135–142, 2004.

[49] E. H. Majzoub and K. J. Gross, "Titanium–halide catalyst-precursors in sodium aluminum hydrides," *Journal of Alloys and Compounds*, vol. 356-357, pp. 363-367, 2003.

[50] W. Luo and K. J. Gross, "A kinetics model of hydrogen absorption and desorption in Ti-doped NaAlH$_4$," *Journal of Alloys and Compounds*, vol. 385, pp. 224-231, 2004.

[51] T. A. Dobbins, E. L. Bruster, E. U. Oteri, and J. Ilavsky, "Ultrasmall-angle X-ray scattering (USAXS) studies of morphological trends in high energy milled NaAlH$_4$ powders," *Journal of Alloys and Compounds*, vol. 446-447, pp. 248-254, 2007.

[52] V. Bérubé, G. Radtke, M. Dresselhaus, and G. Chen, "Size effects on the hydrogen storage properties of nanostructured metal hydrides: A review," *International Journal of Energy Research*, vol. 31, pp. 637-663, 2007.

[53] J. Wang, A. D. Ebner, R. Zidan, and J. A. Ritter, "Synergistic effects of co-dopants on the dehydrogenation kinetics of sodium aluminum hydride," *Journal of Alloys and Compounds*, vol. 391, pp. 245-255, 2005.

[54] C. J. Cramer, *Essentials of Computational Chemistry: Theories and Models*: John Wiley & Sons, 2004.

[55] E. Lewars, *Introduction to the theory and applications of molecular and quantum mechanics*: Kluwer Academic publications, 2003.

[56] F. Jensen, *Introduction to Computational Chemistry*: Wiley&Sons, 2002.

[57] A. R. Leach, *Molecular Modeling: principles and applications*, Second ed. UK: Prentice Hall, 2001.

[58]  M. Holthausen and W.Koch, *A Chemist's Guide to Density Functional Theory*: Wiler-VCH, 2001.

[59]  F. Jensen, *Introduction to Computational Chemistry*. NewYork: Wiley, 1999.

[60]  J. M. Seminario, *Recent Developments and Applications of Modern Density Functional Theory*, vol. 4. Amsterdam: Elsevier Science Publishers, 1996.

[61]  J. B. Foresman and A.Frisch, *Exploring Chemistry with Electronic Structure Methods*, vol. 2. Pittsburgh, PA: Gaussian,Inc, 1996.

[62]  D. J. Griffiths, *Introduction to Quantum Mechanics*, Second ed. New Jersey: Prentice-Hall, 2004.

[63]  N. D. Spencer and J. H. Moore, *Encyclopedia of Chemical Physics and Physical Chemistry*: Taylor & Francis, 2001.

[64]  A.R.Leach, *Molecular Modeling: principles and applications*, Second ed. UK: Prentice Hall, 2001.

[65]  F.Jensen, *Introduction to Computational Chemistry*: Wiley&Sons, 2002.

[66]  E.Lewars, *Computational chemistry: Introduction to the Theory and Applications of Molecular and Quantum Mechanics*: Kluwer Acad. Publishers, 2003.

[67]  J. P. Perdew and Y. Wang, "Accurate and simple analytic representation of the electron-gas correlation energy," *Physical Review B*, vol. 45, pp. 13244, 1992.

[68]  S. J. Vosko, L. Wilk, and M. Nusair, "Accurate spin-dependent electron liquid correlation energies for local spin density calculations: A critical analysis," *Canadian Journal of Physics*, vol. 58, pp. 1200-1211, 1980.

[69]  J. C. Slater, "A simplification of the Hartree-Fock method," *Physical Review*, vol. 81, pp. 385-390, 1951.

[70]  *Density Functional Theory: A Tool for Chemistry*. Amsterdam: Elsevier, 1995.

[71]  T. Ziegler, "Approximate density functional theory as a practical tool in molecular energetics and dynamics," *Chemical Reviews*, vol. 91, pp. 651–667, 1991.

[72]  J. P. Perdew, K. Burke, and M. Ernzerhof, "Generalized Gradient Approximation Made Simple," *Physical Review Letters*, vol. 77, pp. 3865-3868, 1996.

[73]  B. Hammer, L. B. Hansen, and J. K. Norskov, "Improved adsorption energetics within density-functional theory using revised Perdew-Burke-Ernzerhof functionals," *Physical Review B*, vol. 59, pp. 7413-7421, 1999.

[74]  Z. Wu and R. E. Cohen, "More accurate generalized gradient approximation for solids," *Physical Review B*, vol. 73, pp. 2351161-6, 2006.

[75]  J. A. White and D. M. Bird, "White, J. A.; Bird, D. M. "Implementation of gradient-corrected exchange-correlation potentials in Car-Parrinello total-energy calculations," *Physical Review B*, vol. 50, pp. 4954-4957, 1994.

[76]  A. D. Becke, "Density-functional exchange-energy approximation with correct asymptotic behavior," *Physical Review A*, vol. 38, pp. 3098-3100, 1988.

[77]  C. Lee, W. Yang, and R. G. Parr, "Development of the Colle-Salvetti correlation-energy formula into a functional of the electron density," *Physical Review B*, vol. 37, pp. 785-789, 1988.

[78]  T. Tsuneda, T. Suzumura, and K. Hirao, "A new one-parameter progressive Colle-Salvetti-type correlation functional", J. Chem. Phys., 110, 10664 (1999)." *Journal of Chemical Physics*, vol. 110, pp. 10664-10678, 1999.

[79]  A. D. Boese and N. C. Handy, "A new parametrization of exchange–correlation generalized gradient approximation functionals," *Journal of Chemical Physics*, vol. 114, pp. 5497-5503, 2001.

[80]  D. A. McQuarrie, *Statistical Mechanics*. Sausalito: University Science Books, 2000.

[81]  G. Henkelman, B. P. Uberuaga, and H. Jonsson, "A climbing image nudged elastic band method for finding saddle points and minimum energy paths," *Journal of Chemical Physics*, vol. 113, pp. 9901-9904, 2000.

[82]  G. Henkelman and H. Jonsson, "A dimer method for finding saddle points on high dimensional potential surfaces using only first derivatives," *Journal of Chemical Physics*, vol. 111, pp. 7010-7022, 1999.

[83]  D. G. Truhlar, B. C. Garrett, and S. J. Klippenstein, "Current Status of Transition-State Theory," *Journal of Physical Chemistry*, vol. 100, pp. 12771-12800, 1996.

[84]  T. A. Halgren and W. N. Lipscomb, "The synchronous-transit method for determining reaction pathways and locating molecular transition states," *Chemical Physics Letters*, vol. 49, pp. 225-232, 1977.

[85]  M. P. Allen and D.J.Tildesley, *Computer Simulation of Liquids*. NewYork: Oxford University Press, 1987.

[86]  L.Verlet, "Computer experiments on Classical Fluids.I.Thermodynamic Properties of Lennard-JonesMolecules," *Physical Review*, vol. 159, pp. 98-103, 1967.

[87]  H. C. A. W.C.Swope, P.H.Berens, K.R.Wilson, "A Computer Simulation Method for the Calculation of Equilibrium Constants for the Formation of Physical Clusters of Molecules," *Journal of Chemical Physics*, vol. 76, pp. 637-649, 1982.

[88]  C.W.Gear, *Numerical Initial Value Problems in Ordinary Differential Equations.* Englewood Cliffs, NJ: Prentice Hall, 1971.

[89]  D.Beeman, "Some Multistep Methods for Use in Molecular Dynamics Calculations," *Journal of Computational Physics,* vol. 20, pp. 130-139, 1976.

[90]  T. Arias, M. C. Payne, and J. D. Joannopoulos, "Ab initio molecular dynamics: Analytically continued energy functionals and insights into iterative solutions," *Physical Review Letters,* vol. 69, pp. 1077-1080, 1992.

[91]  D. Alfe, "Ab initio molecular dynamics, a simple algorithm for charge extrapolation," *Computational Physics Communications,* vol. 118, pp. 31-33, 1999.

[92]  C. Kittel, *Introduction to Solid State Physics,* Fifth ed: Wiley, 1976.

[93]  N. W. Ashcroft and N. D. Mermin, *Solid State Physics*: Holt, Rinehart and Winston, 1976.

[94]  S. J. Clark, M. D. Segall, C. J. Pickard, P. J. Hasnip, M. J. Probert, K. Refson, and M. C. Payne, "First principles methods using CASTEP," *Zeitschrift fuer Kristallographie,* vol. 220, pp. 567-570, 2005.

[95]  M. C. Payne, M. P. Teter, D. C. Allan, T. A. Arias, and J. D. Joannopoulos, "Iterative minimisation techniques for ab initio total-energy calculations: molecular dynamics and conjugate gradients," *Reviews of Modern Physics,* vol. 64, pp. 1045-1097, 1992.

[96]  H. J. Monkhorst and J. D. Pack, "Special points for Brillouin-zone integrations," *Physical Review B,* vol. 13, pp. 5188-5192, 1976.

[97]  M.T.Yin and M.L.Cohen, "Ground-state properties of diamond," *Physical Review B,* vol. 24, pp. 6121-6124, 1981.

[98]  J. C. Philips and L. Kleinmen, "New Method for Calculating Wave Functions in Crystals and Molecules," *Physical Review,* vol. 116, pp. 287-294, 1959.

[99]  G. P. Srivastava and D. Weaire, "The theory of the cohesive energies of solids," *Advances in Physics,* vol. 26, pp. 463-517, 1987.

[100]  L. Kleinman and D. M. Bylander, "Efficacious form for model pseudopotentials," *Physical Review Letters,* vol. 48, pp. 1425-1428, 1982.

[101]  D. R. Hamman, M. Schlüter, and C. Chiang, "Norm-conserving pseudopotentials," *Physical Review Letters,* vol. 43, pp. 1494-1497, 1979.

[102]  J. S. Lin, A. Qteish, M. C. Payne, and V. Heine, "Optimized and transferable nonlocal separable ab initio pseudopotentials," *Physical Review B*, vol. 47, pp. 4174-4180, 1993.

[103]  V. Milman, B. Winkler, J. A. White, C. J. Pickard, M. C. Payne, E. V. Akhmatskaya, and R. H. Nobes, "Electronic structure, properties and phase stability of inorganic crystals: A pseudopotential plane-wave study," *International Journal of Quantum Chemistry*, vol. 77, pp. 895-910, 2000.

[104]  N. Troullier and J. L. Martins, "Efficient pseudopotentials for plane-wave calculations," *Physical Review B*, vol. 43, pp. 1993-2006, 1991.

[105]  D. Vanderbilt, "Soft self-consistent pseudopotentials in a generalized eigenvalue formalism," *Physical Review B*, vol. 41, pp. 7892-7895, 1990.

[106]  S. G. Louie, S. Froyen, and M.L.Cohen, "Nonlinear ionic pseudopotentials in spin-density-functional calculations," *Physical Review B*, vol. 26, pp. 1738-1742, 1982.

[107]  G. Kresse and J. Furthmuller, "Efficient iterative schemes for ab initio total-energy calculations using a plane-wave basis set," *Physical Review B*, vol. 54, pp. 11169-11186, 1996.

[108]  B. G. Pfrommer, M. Cote, S. G. Louie, and M.L.Cohen, "Relaxation of Crystals with the Quasi-Newton Method," *Journal of Computational Physics*, vol. 131, pp. 133-140, 1997.

[109]  D. Sanchez-Portal, E. Artacho, and J. M. Soler, "Projection of plane-wave calculations into atomic orbitals," *Solid State Communications*, vol. 95, pp. 685-692, 1995.

[110]  R. S. Mulliken, "Electronic Population Analysis on LCAO-MO Molecular Wave Functions. I," *Journal of Chemical Physics*, vol. 10, pp. 1833-1840, 1955.

[111]  M. D. Segall, C. J. Pickard, R. Shah, and M. C. Payne, "Population analysis in plane wave electronic structure calculations," *Molecular Physics*, vol. 89, pp. 571-577, 1996.

[112]  M. D. Segall, R. Shah, C. J. Pickard, and M. C. Payne, "Population analysis of plane-wave electronic structure calculations of bulk materials," *Physical Review B*, vol. 54, pp. 16317-16320, 1996.

[113]  C. R. Bradley and A.P.Cracknell, *The Mathematical Theory of Symmetry in Solids*. Oxford: Clarendon Press, 1972.

[114]  G. J. Ackland, "Embrittlement and the Bistable Crystal Structure of Zirconium Hydride," *Physical Review Letters*, vol. 80, pp. 2233-2236, 1998.

[115] S. Baroni, S. deGironcoli, A. dalCorso, and P. Giannozzi, "Phonons and related crystal properties from density-functional perturbation theory," *Reviews of Modern Physics*, vol. 73, pp. 515-562, 2001.

[116] K. Parlinski, Z. Q. Li, and Y. Kawazoe, "First-Principles Determination of the Soft Mode in Cubic ZrO2," *Physical Review Letters*, vol. 78, pp. 4063-4066, 1997.

[117] G. J. Ackland, M. C. Warren, and S. J. Clark, "Practical methods in ab initio lattice dynamics," *Journal of Physics: Condensed Matter*, vol. 9, pp. 7861-7872, 1997.

[118] X. Gonze, "First-principles responses of solids to atomic displacements and homogeneous electric fields: Implementation of a conjugate-gradient algorithm," *Physical Review B*, vol. 55, pp. 10337-10354, 1997.

[119] B. J. Delley, "An all-electron numerical method for solving the local density functional for polyatomic molecules," *Journal of Chemical Physics*, vol. 92, pp. 508-517, 1990.

[120] A. Bergner, M. Dolg, W. Kuechle, H. Stoll, and H. Preuss, "Ab initio energy-adjusted pseudopotentials for elements of groups 13-17," *Molecular Physics*, vol. 80, pp. 1431 - 1441, 1993.

[121] "Inorganic Crystal Structure Database," NIST/FIZ Karlsruhe.

[122] B. C. Hauback, H. W. Brinks, C. M. Jensen, K. Murphy, and A. J. Maeland, "Neutron diffraction structure determination of $NaAlD_4$," *Journal of Alloys and Compounds*, vol. 358, pp. 142-145, 2003.

[123] G. Kresse and D. Joubert, "From ultrasoft pseudopotentials to the projector augmented-wave method," *Physical Review B*, vol. 59, pp. 1758-1775, 1999.

[124] V. Milman, B. Winkler, J. A. White, C. J. Pickard, M. C. Payne, E. V. Akhmatskaya, and R. H. Nobes, "Electronic Structure, Properties, and Phase Stability of Inorganic Crystals: A Pseudopotential Plane-Wave Study," *International Journal of Quantum Chemistry*, vol. 77, pp. 895-910, 2000.

[125] S. Gomes, G. Renaudin, H. Hagemann, K. Yvon, M. P. Sulic, and C. M. Jensen, "Effects of milling, doping and cycling of NaAlH4 studied by vibrational spectroscopy and X-ray diffraction," *Journal of Alloys and Compounds*, vol. 390, pp. 305-313, 2005.

[126] B. Bonnetot, G. Chahine, P. Claudy, M. Diot, and J. M. Letoffe, "Sodium tetrahydroaluminate $NaAlH_4$ and hexahydroaluminate $Na_3AlH_6$ Molar heat capacity and thermodynamic properties from 10 to 300K," *Journal of Chemical Thermodynamics*, vol. 12, pp. 249-254, 1980.

[127] X. Ke and I. Tanaka, "Decomposition reactions for NaAlH4, Na3AlH6, and NaH: First-principles study," *Physical Review B*, vol. 71, pp. 024117, 2005.

[128] O. Tougait and H. Noel, "Stoichiometry of $UAl_4$," *Intermetallics*, vol. 12, pp. 219-223, 2004.

[129] C. G. Shull, E. O. Wollan, G. A. Morton, and W. L. Davidson, "Neutron Diffraction Studies of NaH and NaD," *Physical Review*, vol. 73, pp. 842-847, 1948.

[130] A. Anderson, "Predicitng formation enthalpies of metal hydrides," Risø National Laboratory, Roskilde, Denmark Risø-R-1484(EN), 2004.

[131] I. V. Ionova and E. A. Carter, "Direct inversion in the iterative subspace-induced acceleration of the ridge method for finding transition states," *Journal of Chemical Physics*, vol. 103, pp. 5437–5441, 1995.

[132] I. V. Ionova and E. A. Carter, "Ridge method for finding saddle points on potential energy surfaces," *Journal of Chemical Physics*, vol. 98, pp. 6377–6386, 1993.

[133] R. E. Gillilan and K. R. Wilson, "Shadowing, rare events, and rubber bands. A variational Verlet algorithm for molecular dynamics," *Journal of Chemical Physics*, vol. 97, pp. 1757–1772, 1992.

[134] D. R. Trinkle, R. G. Hennig, S. G. Srinivasan, D. M. Hatch, M. D. Jones, H. T. Stokes, R. C. Albers, and J. W. Wilkins, "A New Mechanism for the Alpha to Omega Martensitic Transformation in Pure Titanium," *Physical Review Letters*, vol. 91, pp. 025701, 2003.

[135] K. J. Caspersen and E. A. Carter, "Finding transition states for crystalline solid–solid phase transformations," *Proceedings of National Academy of Sciences*, vol. 102, pp. 6738–6743, 2005.

[136] Accelrys, "Materials Studio®," 4.0 ed. San Diego: Accelrys Software, Inc., 2006.

[137] N. Govind, M. Petersen, G. Fitzgerald, D. King-Smith, and J. Andzelm, "A generalized synchronous transit method for transition state location," *Computational Materials Science*, vol. 28, pp. 250-258, 2003.

[138] G. K. P. Dathara and D. S. Mainardi, "Modeling Effects of Titanium Dopants on Hydrogen Adsorption/Desorption Kinetics by Sodium Alanates," presented at AIChE 2007 Annual Meeting, Salt Lake City, UT, 2007.

[139] P. Norby and A. N. Christensen, "Preparation and structure of $Al_3Ti$," *Acta Chemica Scandinavica, Series A*, vol. 40, pp. 157-159, 1986.

[140] P. E. Irving and C. A. Beevers, "Some metallographic and lattice parameter observations on titanium hydride," *Metallurgical Transactions*, vol. 2, pp. 613-615, 1971.

[141] A. G. Haiduc, H. A. Stil, M. A. Schwarz, P. Paulus, and J. J. C. Geerlings, "On the fate of the Ti catalyst during hydrogen cycling of sodium alanate," *Journal of Alloys and Compounds*, vol. 393, pp. 252-263, 2005.

[142] G. K. P. Dathara and D. S. Mainardi, "Structure and Dynamics of Ti-Al-H Compounds in Ti-Doped NaAlH$_4$," *Molecular Simulation*, vol. 34, pp. 201-210, 2008.

[143] C. Weidenthaler, A. Pommerin, M. Felderhoff, B. Bogdanović, and F. Schüth, "On the state of the titanium and zirconium in Ti- or Zr-doped NaAlH$_4$ hydrogen storage material," *Physical Chemistry Chemical Physics*, vol. 5, pp. 5149-5153, 2003.

[144] M. Fichtner, O. Fuhr, O. Kircher, and J. Rothe, "Small Ti clusters for catalysis of hydrogen exchange in NaAlH$_4$," *Nanotechnology*, vol. 14, pp. 778–785, 2003.

[145] H. W. Brinks, B. C. Hauback, S. S. Srinivasan, and C. M. Jensen, "Synchrotron X-ray Studies of Al$_{1-y}$Ti$_y$ Formation and Re-hydriding Inhibition in Ti-Enhanced NaAlH$_4$," *Journal of Physical Chemistry B*, vol. 109, pp. 15780-15785, 2005.

[146] T. Dobbins, M. Abrecht, Y. Uprety, and K. Moore, "An x-ray photoemission electron microscopy (XPEEM) study of the formation of Ti-Al phases in 4 mol % TiCl$_3$–catalyzed NaAlH$_4$ during high energy ball milling," *Nanotechnology*, 2009.

[147] T. Hong, T. J. Watson-Yang, A. J. Freeman, T. Oguchi, and J.-H. Xu, "Crystal structure, phase stability and electronic structure of Ti-Al intermetallics:TiAl$_3$," *Physical Review B*, vol. 41, pp. 12462-12467, 1990.

[148] M. D. Segall, P. J. D. Lindan, M. J. Probert, C. J. Pickard, P. J. Hasnip, S. J. Clark, and M. C. Payne, "First-principles simulation: ideas, illustrations and the CASTEP code," *Journal of Physics: Condensed Matter*, vol. 14, pp. 2717-2743, 2002.

[149] G. W. Crabtree and M. S. Dresselhaus, "The Hydrogen Fuel Alternative," *MRS Bulletin*, vol. 33, 2008.

[150] M. E. Bowden, G. J. Gainsford, and W. T. Robinson, "Room temperature structure of ammonia borane," *Australian Journal of Chemistry*, vol. 60, pp. 149-153, 2007.

[151] W. T. Klooster, T. F. Koetzle, P. M. Siegbahn, T. B. Richardson, and R. H. Crabtree, "Study of the N-H---H-B Dihydrogen Bond Including the Crystal Structure of BH$_3$NH$_3$ by Neutron Diffraction," *Journal of the American Chemical Society*, vol. 121, pp. 6337-6343, 1999.

[152]   C. R. Miranda and G. Ceder, "Ab initio investigation of ammonia-borane complexes for hydrogen storage," *Journal of Chemical Physics*, vol. 126, pp. 1847031-11, 2007.

[153]   E. W. Hughes, "The crystal structure of Ammonia Borane $H_3NBH_3$," *Journal of the American Chemical Society*, vol. 78, pp. 502-503, 1956.

[154]   F. Cheng, H. Ma, Y. Li, and J. Chen, "$Ni_{1-x}Pt_x$ (x =0-0.12) Hollow Spheres as Catalysts for Hydrogen Generation from Ammonia Borane," *Inorganic Chemistry*, vol. 46, pp. 788-794, 2007.